Studies of
Large Scale Atmospheric Energetics

Department of Meteorology
The University of Wisconsin
Madison, Wisconsin 53706

Contributions by
G.J. Dittberner
D.G. Hahn
L.H. Horn
R.A. Rudy
F.S. Sechrist

L.H. Horn and D.R. Johnson, Joint Principal Investigators

FINAL REPORT

The Research in this document has been supported
by the National Environmental Satellite Center of the
Environmental Science Services Administration under Grant WBG 52

June 1969

Studies of
Large Scale Atmospheric Energetics

Department of Meteorology
The University of Wisconsin
Madison, Wisconsin 53706

Contributions by
G.J. Dittberner
D.G. Hahn
L.H. Horn
R.A. Rudy
F.S. Sechrist

L.H. Horn and D.R. Johnson, Joint Principal Investigators

FINAL REPORT

The Research in this document has been supported
by the National Environmental Satellite Center of the
Environmental Science Services Administration under Grant WBG 52

June 1969

TABLE OF CONTENTS

400-126

INTRODUCTION

The research presented in this report includes the final studies completed with the support of ESSA grant WBG-52. Other studies supported by this grant were included in the annual reports of 1966 and 1967. In addition, the monograph by Professor John A. Dutton of Pennsylvania State University and Donald R. Johnson, "The Theory of Available Potential Energy and a Variational Approach to Atmospheric Energetics," published in Volume 12 of Advances in Geophysics, was in part supported by this grant.

Nearly all the studies completed under grant WBG-52 were also partially supported by the Wisconsin Alumni Research Foundation and National Science Foundation through the University of Wisconsin Research Committee in the form of a grant for computational funds and use of computer facilities.

Additional research initiated under grant WBG-52 is continuing through the support of ESSA grant E-8-69(G). This work will be presented in the next annual report.

Lyle H. Horn
Donald R. Johnson
—Joint Principal Investigators

Madison, Wisconsin
June, 1969

THE GENERATION OF AVAILABLE POTENTIAL ENERGY IN A MID-LATITUDE CYCLONE

by

Douglas G. Hahn
Lyle H. Horn

ABSTRACT:

The generation expression in the energy equations of Smith (1967) is modified so that it represents the available potential energy generated at the synoptic scale. The generation based on a regional reference state and Smith's (1967) heating estimates is studied both temporally and spacially in case studies of two March 1962 mid-latitude cyclones.

The generation expression has been divided into two terms. One is the product of the mean heating and the mean efficiency factor on a pressure surface (it represents the tendency for large-scale hydrostatic destabilization); the other is the covariance of the deviations of the efficiency factor and the heating. During the beginning stages of a cyclone's development, the vertical gradients of the heating and the regional efficiency factor are large, and the process of hydrostatic destabilization generates substantial amounts of available potential energy. In later stages of a cyclone's development, horizontal gradients of e_R and Q increase, and the covariance generation term becomes quite large. In the final stages of a cyclone's history, heating occurs in the cold air and at higher levels, and the regional generation becomes negative. The signs and magnitudes of the regional generation tend to be similar to those of the time rate of change of kinetic energy, i. e. there appears to be a tendency for regional diabatic heating to contribute both to a cyclone's growth and to its demise.

1. Introduction

The mechanisms which produce and maintain the kinetic energy of mid-latitude cyclones have long been a concern of the meteorologist. These mechanisms have been classified as one of two basic types. One involves the redistribution of pre-existing kinetic energy, i.e., the kinetic energy of some mean zonal flow is transferred to that of a cyclonic disturbance. Kuo (1949) and Fjortoft (1950) have made significant contributions to an understanding of this process, usually called barotropic instability. The other basic type, baroclinic instability, involves a conversion of potential energy to kinetic energy. The theoretical development explaining this conversion mechanism has been extensively discussed in papers by Charney (1947) and Eady (1949).

Other investigators in an attempt to better understand the processes which produce and maintain kinetic energy have focused their attention on the energetics of the general circulation of the atmosphere. Lorenz (1955), followed by Van Mieghem (1956) and Dutton and Johnson (1967), have developed equations which describe the portion of the total potential energy (internal energy plus gravitational potential energy) which is available for conversion to kinetic energy through baroclinic processes. Their equations include an expression which shows that diabatic processes play an important role in generating available potential energy. On the global scale, Dutton and Johnson (1967) have shown that there is a net positive generation of available potential energy due to heating at relatively high pressure in low latitudes and cooling at relatively low pressure in high latitudes. However, at the synoptic scale there is some question as to whether the diabatic processes associated with the eddies create or destroy available potential energy. Some investigators, such as Corcoran and Horn (1963) and Suomi and Shen (1962), using Lorenz's approximate equation have obtained numerical results indicating that infrared cooling creates eddy available potential energy. Using the same equation, others, most of whom have calculated the eddy generation as a residual term, have concluded that the sum of all diabatic processes destroys eddy available potential energy. See Oort (1964). On the other hand, Dutton and Johnson (1967), also calculating the generation of eddy available potential energy as a residual but using different equations, obtained results indicating that the net diabatic heating creates eddy available potential energy. To better understand the role diabatic processes play in the generation of available potential energy at the synoptic scale, case studies of the generation associated with two March, 1962, cyclones are conducted in this paper.

The energy equations developed by Dutton and Johnson (1967) contain a generation term involving the product of diabatic heating and an efficiency factor, which is determined by the distribution of potential

temperature and pressure. Their generation term, very similar to the one obtained by Lorenz (1955b), has provided new insight into the problem of calculating the generation of available potential energy. However, like previous theoretical studies they postulate integration over the entire atmosphere. Recently Smith (1967) developed a set of energy equations necessary for the calculation of an energy budget for a limited region and used these equations to obtain the energy budget for North America for March, 1962. His equations include a generation term which is essentially the same as Dutton and Johnson's. In this paper, Smith's generation term is used in studying the generation during the development of a cyclone. While Smith's computational study covered all of North America for March, 1962, this study involves the limited areas and times chosen from his data which coincide with individual cyclones. Specifically, this paper will attempt to (1) develop a method of calculating a three-dimensional field of efficiency factors which displays the regions about an extratropical cyclone in which diabatic processes are most efficient in generating eddy available potential energy, (2) study the changing patterns of the field of efficiency factors as the cyclone matures, and (3) study the changes in magnitude of the generation term during the life of the cyclone.

It is important to note that for this study we are concerned only with the creation of available potential energy due to the diabatic heating and cooling associated with a cyclone. There are, of course, other processes (horizontal and vertical transport of available potential energy through the boundaries, and the conversion of kinetic energy to available potential energy) which can serve to change the amount of available potential energy within the region of the cyclone. However, no attempt is made to explain all of the changes in behavior of the storm. We are concerned only with the contribution of the generation to the supply of eddy available potential energy in the region of the cyclone.[1]

2. Discussion of Basic Equations

In this section, the basic equations are discussed in some detail. As derived by Smith (1967), the rate of change of the contribution to the global supply of potential energy, $\partial A/\partial t$, from a limited region is (see table of symbols (page 32):

[1] Lorenz (1955) defined the generation of eddy available potential energy as the east-west covariance of temperature and heating on a pressure surface. Because of the limited north-south extent of the area studied for individual cyclones, the generation discussed here will be considered as essentially eddy generation.

$$\partial A/\partial t = g^{-1} \int_R \int_{p_0}^{p} [p^K - (\bar{p})^K][p]^{-K} Q \, dp dR + g^{-1} \int_R \int_{p_0}^{p} \omega\alpha \, dp dR$$

$$- g^{-1} \int_R \int_{p_0}^{p} \nabla_p \cdot \{c_p [p^K - (\bar{p})^K][p]^{-K} T \vec{V}\} dp dR \qquad (1)$$

$$- g^{-1} \int_R \int_{p_0}^{p} \partial/\partial p \{c_p [p^K - (\bar{p})^K][p]^{-K} T \omega\} dp dR .$$

The first term on the right represents the generation, the second the conversion, the third and fourth the change of the contribution to the global supply of available potential energy in the box due to fluxes through the horizontal and vertical boundaries of the region.

The generation term of (1) can be written as

$$G_{RT} = g^{-1} \int_R \int_{p_0}^{p} e_T Q \, dp dR \qquad (2)$$

where Q is heating per unit mass, R is the surface area of the limited region, g is gravity, p is pressure, p_0 is surface pressure, and e_T is the global efficiency factor,

$$e_T = [p^K - (\bar{p})^K][p]^{-K} . \qquad (3)$$

Here, $\bar{p}$ is the pressure a mass element would assume if the entire atmosphere were to undergo an adiabatic redistribution to a horizontal statically stable state of minimum total potential energy.

The efficiency factor, e_T, specifies the regions where diabatic heating (or cooling) will be the most efficient in generating (or destroying) available potential energy. It will be positive where $p > \bar{p}$ and negative where $p < \bar{p}$. The magnitude of the efficiency factor will be the greatest along isentropic surfaces which intersect the most pressure surfaces, i.e. along the θ surfaces which intersect the surface of the earth in warm, tropical regions and extend into the upper troposphere in polar regions. The largest positive generation occurs in regions where the signs of e_T and Q are the same and their magnitudes are large. The largest negative generation occurs where e_T and Q are large but of opposite signs.

In obtaining the value of the efficiency factor for a given point, it is necessary to compute a reference pressure, $\bar{p}$, which involves calculating the global mean pressure of the potential temperature surface passing

through that point. As a function of potential temperature, θ, $\bar{p}$ can be written, according to Dutton and Johnson (1967), as

$$\bar{p}(\theta) = S^{-1} \int_S \int_{\theta_t}^{\theta} \partial p/\partial\theta \, d\theta dS \qquad (4)$$

where S is the area of the surface of the earth, and θ_t is the potential temperature at the top of the atmosphere. In his computations, Smith (1967) used global mean annual values of $\bar{p}$ which were calculated by Dutton and Johnson. Consequently, Smith's (1967) calculations show how the heating (or cooling) over North America contributes to the global generation of available potential energy.

For this study, the computation of the efficiency factor using a global reference state would present a problem, because here we are interested in the regional, rather than the global, generation of available potential energy. Figure 1 illustrates this problem well. Assume that the box extending from 32° N to 51° N represents the area occupied by a mid-latitude winter cyclone. Defining an efficiency factor on a global scale results in negative values of e_T throughout most of the region, thus, for example, latent heating in the warm sector of the cyclone destroys available potential energy on the global scale although actually increasing the slope of the θ surfaces regionally. However, if a regional efficiency factor, e_R, were defined for the mass within this box, both latent heating in the warm sector and infrared cooling in the cool sector would tend to increase the slope of the θ surfaces, and thus generate available potential energy locally. Consequently, we wish to develop a procedure which will permit a study of the effects of heating in a local area. The method of doing this is given in the next section.

3. Procedure

To gain a better understanding of the role that diabatic processes play at the eddy scale, the efficiency factor in this study was defined for a region of the atmosphere containing the cyclone. A box was chosen which enclosed the cyclone system. Using the surface pressure analysis, this was objectively done by extending the edge of the box out to the center or ridge of the surrounding high pressure systems. If the cyclone was adjacent to another cyclonic disturbance, the 850 mb contour map was used, and the edge of the box was placed along the line of greatest horizontal wind shear between the two circulations. The bottom and top of the box were the earth's surface and the 250 mb surface, respectively. The 250 mb surface was chosen as the top to insure adequate wind data for the necessary calculations. The box was moved along as the cyclone

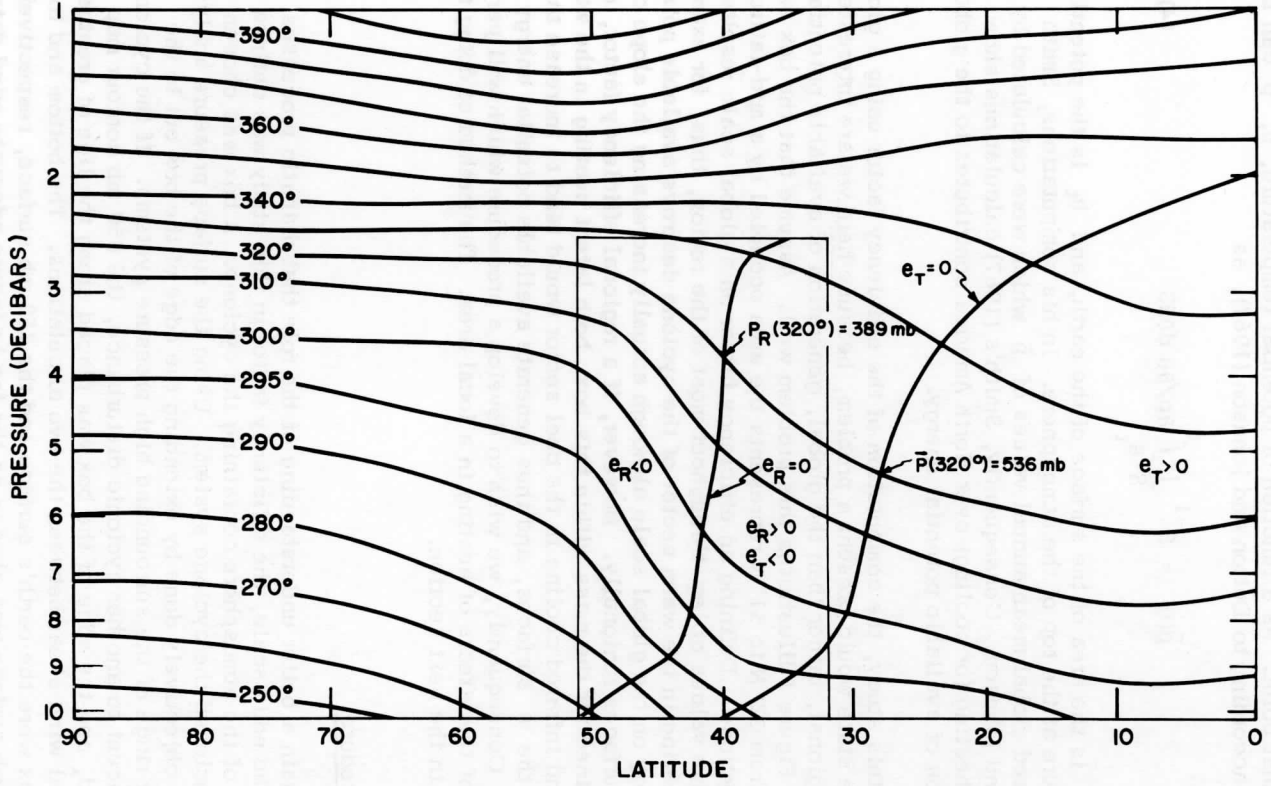

Figure 1. A typical winter North Pole-Equator potential temperature cross section showing a box enclosing a mid-latitude cyclone. The lines $e_R = 0$ and $e_T = 0$ divide the regions of positive and negative regional efficiency factors and global efficiency factors, respectively.

progressed and its size was adjusted (according to the above criteria) to fit changes in the storm's dimensions.

Equation (2), which gives the contribution of a limited region to the global generation of available potential energy, was used to obtain the generation within the boxes. However, to measure the significance of the generation locally, Equation (2) was partitioned into two parts:

$$G_{RT} = g^{-1} \int_R \int_{p_0}^{p} e_R Q \, dp dR + g^{-1} \int_R \int_{p_0}^{p} [e_T - e_R] Q \, dp dR \qquad (5)$$

where

$$e_R = (p^K - p_R^K)(p)^{-K} \qquad (6)$$

and

$$p_R(\theta) = R^{-1} \int_R \int_{\theta_t}^{\theta} \partial p / \partial \theta \, d\theta dR \qquad (7)$$

The term p_R is the pressure a parcel would assume if the entire mass within the box were adiabatically redistributed to a flat, horizontal state of minimum total potential energy. At a given point, p_R was determined by computing the regional mean pressure of the θ surface which passed through that point. This was done by computing $p_R(\theta)$ for given θ surfaces (215°K, 220°K, ..., 365°K), and linear interpolation was used to determine intermediate $p_R(\theta)$'s. If the θ surface was found to lie below the surface of the earth, the convention used by Lorenz (1955) was applied, setting p equal to the surface pressure. Analogously, if the θ surface extended above the 250 mb surface, the pressure, p, was set equal to 250 mb. It is important to note that the mathematical description of the reference state is only arbitrary, and there may be other ways of defining such a reference state for the region. In this case, even though the reference state is easy to describe mathematically, its probability of being physically realized is most unlikely. If such an adiabatic adjustment were to occur within the box to produce increased kinetic energy and this flat, horizontal reference state, first order discontinuities in the pressure and temperature fields would be created along the lateral boundaries of the region unless compensating adjustments occurred in the adjacent areas. However, this reference state does provide a simple, effective method of measuring the generation of eddy available potential energy. With the reference state so defined, the first of the two generation components in (5) represents the available potential energy generated inside the box based on the efficiency factor derived from the enclosed mass field. Such a generation is an important process contributing to the change in baroclinicity within the region. With this definition of a local reference atmosphere diabatic heating in the warm regions within the box,

where $e_R > 0$, creates eddy available potential energy, while decreasing the global supply of available potential energy, since $p_R < \bar{p}$ in most winter cases (see Figure 1).

Of lesser importance for this study is the second term of (5) which represents the difference $G_{RT} - G_{RR}$, where G_{RT} is the generation of available potential energy inside the box with respect to the global reference state, and G_{RR} is the generation of available energy inside the box with respect to the regional reference state. The difference of these two generation terms can be written

$$G_{RT} - G_{RR} = \int_R \int_{p_0}^{p} [p_R^K - (\bar{p})^K][p]^{-K} Q \, dp dR \qquad (8)$$

In the special case where the two reference atmospheres are identical, the term is, of course, zero. However in the winter period studied here it is non-zero.

The other parameter needed for the generation computations is the heating per unit mass, Q, which was calculated by Smith (1967) for each North American radiosonde station at each of 17 pressure levels (from the surface to 250 mb). The calculation was made by evaluating the first law of thermodynamics

$$Q = c_p \partial T/\partial t + c_p \vec{V} \cdot \nabla_p T + (c_p \partial T/\partial p - \alpha)\omega \qquad (9)$$

where $\partial T/\partial p$ was estimated by finite differencing and where ω was estimated at each level by the kinematic method, assuming that at $z = 0$, $\omega = dp/dt = 0$. The cyclones studied here were selected from those which passed over North America during March, 1962—the time and region corresponding to that of Smith's (1967) study, thus allowing Smith's heating calculations to be used. The two storms chosen for this study traveled across the United States, from Arizona toward Maine, during the periods 2-5 March, 1962 and 10-13 March, 1962.

To obtain the local generation at times 00 GMT and 12 GMT of each of these days, the terms $e_R Q$ and $(e_T - e_R)Q$ were first integrated with respect to pressure, and then integrated over the surface area of the box. The area integration was carried out using a triangular grid system, similar to the one used by Smith (1967) for his energy budget calculations. The results of these calculations are discussed in the next chapter.

4. Results

The procedures described above were used to compute the generation of available potential energy for the actual cyclones shown in Appendix A. The cyclones here investigated are by no means model lows, therefore the results obtained by studying them should not necessarily be considered typical. However, the results can provide meaningful insight for the modeling of the diabatic terms associated with secondary circulations.

Since the computation of the generation involves the integration of the product of the efficiency factor and heating, the discussion of the results has been divided into three parts: (A) the field of regional efficiency factors, (B) the heating field, and (C) the generation.

A. The Field of Regional Efficiency Factors

Some of the most interesting information resulted from investigating the field of efficiency factors within the region of the cyclones. In particular, the time variation of this field during the life of the cyclones is noteworthy. To illustrate the field of efficiency factors at a given time and its evolution in time, a series of cross sections for the 10-13 March cyclone were constructed. The stations used for the cross sections were chosen so that they were (1) in a reasonably straight line, (2) the line passed through the center of the cyclone, and (3) the line was perpendicular to the $e_R = 0$ isoline on the 600 mb surface.

First, let us consider the cross section for 00 GMT March 10, 1962, Figure 2, a period early in the cyclone's development. Examination of the profile of e_R above a typical station in the cold air reveals that the largest positive regional efficiency factors are found near the surface. From the surface upward there is a regular decrease of the efficiency factor, changing from positive to negative between 800 and 600 mb, until the 250 mb region is reached where $|e_R|$ begins to decrease. There are two reasons for the smaller $|e_R|$'s near the top of the box: (1) the 250 mb level is the region of the tropopause where the potential temperature surfaces are more nearly horizontal than in the lower regions of the atmosphere, and (2) an artificial tropopause is produced at 250 mb due to the method of computing $p_R(\theta)$, i.e. for θ surfaces above 250 mb, the pressure of that θ surface was set equal to 250 mb.

For those stations (in the cold air on 10 March), where $e_R > 0$ in the lower troposphere and $e_R < 0$ in the middle and upper troposphere, it is quite obvious that hydrostatic destabilization due to heating at the surface and cooling aloft generates available potential energy for the local region. However, at typical stations in the warm air, there exists

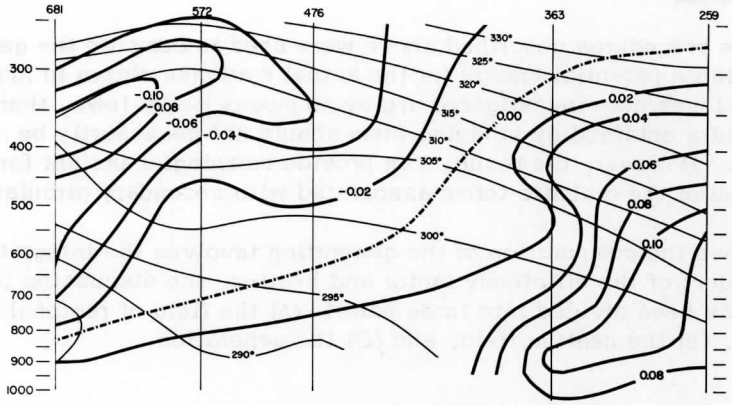

Figure 2. Cross section of potential temperature (°K) and the regional efficiency factor, e_R, from Boise, Idaho (681) to Ft. Worth, Texas (259) for 00 GMT on 10 March 1962.

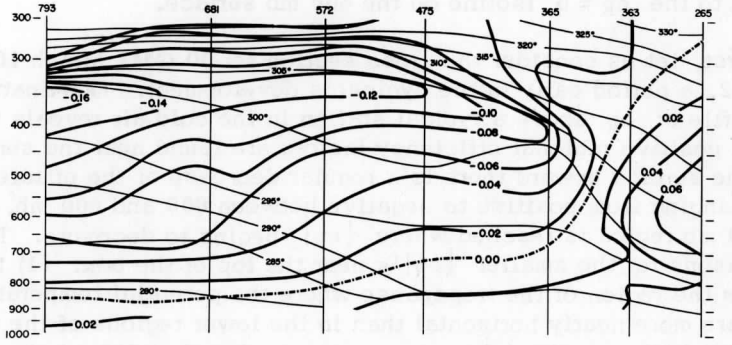

Figure 3. Cross section of potential temperature (°K) and the regional efficiency factor, e_R, from Seattle, Washington (793) to Midland, Texas (265) for 12 GMT on 10 March 1962.

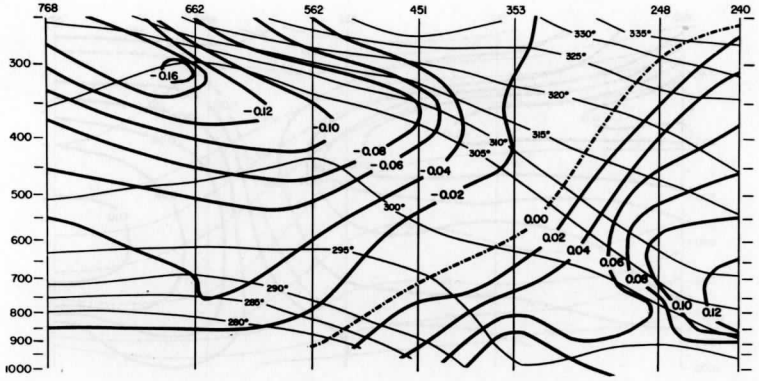

Figure 4. Cross section of potential temperature (°K) and the regional efficiency factor, e_R, from Glasgow, Montana (768) to Lake Charles, Louisiana (240) for 00 GMT on 11 March 1962.

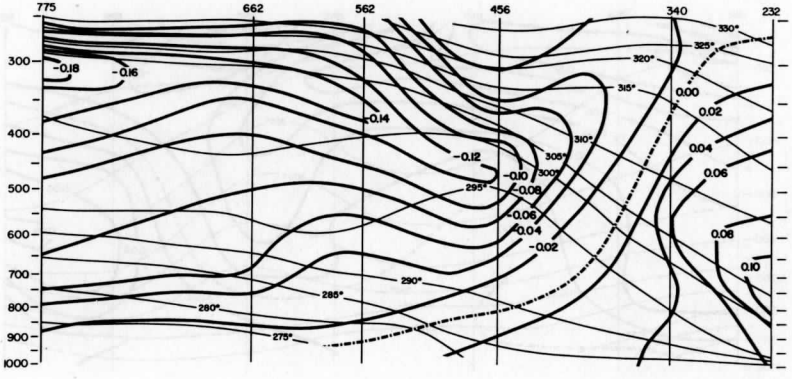

Figure 5. Cross section of potential temperature (°K) and the regional efficiency factor, e_R, from Great Falls, Montana (775) to Burrwood, Louisiana (232) for 12 GMT on 11 March 1962.

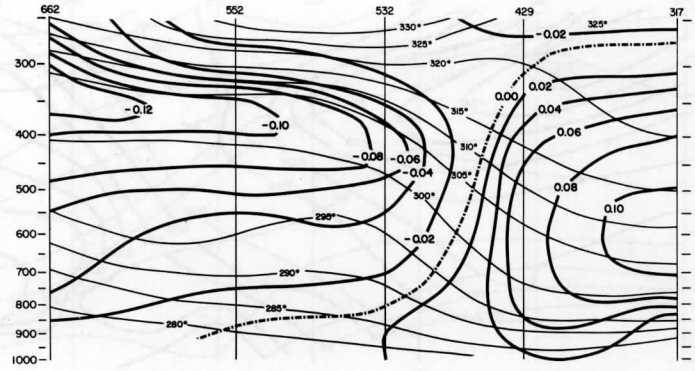

Figure 6. Cross section of potential temperature (°K) and the regional efficiency factor, e_R, from Rapid City, South Dakota (662) to Greensboro, North Carolina (317) for 00 GMT on 12 March 1962.

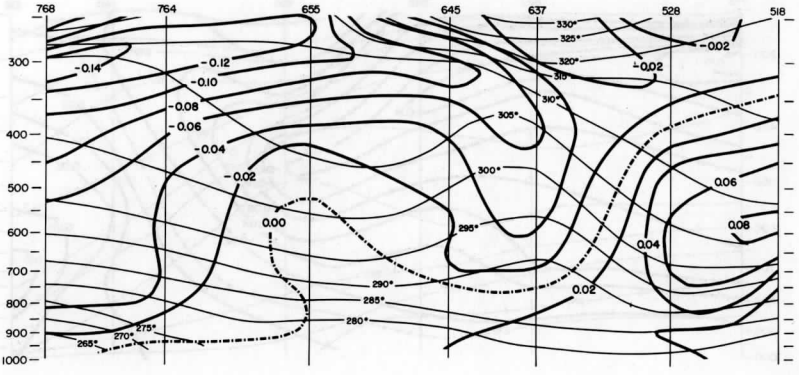

Figure 7. Cross section of potential temperature (°K) and the regional efficiency factor, e_R, from Glasgow, Montana (768) to Albany, New York (518) for 12 GMT on 12 March 1962.

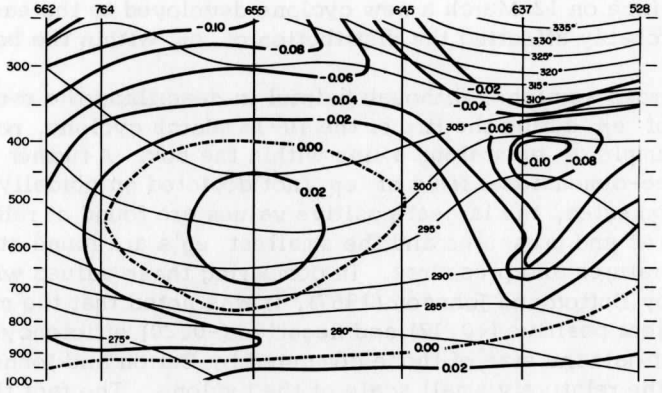

Figure 8. Cross section of potential temperature (°K) and the regional efficiency factor, e_R, from Rapid City, South Dakota (662) to Buffalo, New York (528) for 00 GMT on 13 March 1962.

a deep layer of about 500 mb in which e_R remains quite large before tapering off to small negative values at higher levels. This profile of e_R sets up a favorable situation for large generation due to release of latent heat between 900 and 500 mb in the warm air, where $e_R > 0$, and infrared cooling at the top of the clouds in the upper troposphere where e_R takes on the small negative values. The implications of this distribution of efficiency factors is more fully discussed later in this chapter.

The importance of the changing field of efficiency factors for the 10-13 March cyclone is illustrated by the succeeding cross sections, Figure 3 through Figure 8. As depicted in Figure 2, the $e_R = 0$ isoline was quite horizontal, making the vertical heating gradient (hydrostatic destabilization) important in the generation of available potential energy. As the cyclone became more developed the $e_R = 0$ isoline became more vertical, increasing the relative importance of horizontal gradients of Q in generating available potential energy; note, for example, Figure 6. In the final stages of the cyclone, Figures 7 and 8, the distribution of pressure and potential temperature became such that the field of efficiency factors became rather disorganized, with a center of positive efficiency factors at 500-600 mb west of the storm and negative regional efficiency factors east of the storm. This somewhat disorganized field of regional efficiency factors lessens the importance of any organized field of heating and cooling in generating available potential energy, and in fact indicates that continued heating east of the wave serves to destroy available potential

energy. It should be noted that this final distribution of e_R may not be typical, since on 12 March a new cyclone developed to the east of the region, probably affecting the distribution of e_R within the box.

The cross sections, although helpful in describing the evolution of the field of e_R during the life of the 10-13 March cyclone, reveal only a small sample of e_R's along a line within the box. A further inspection of the three-dimensional field of e_R (not depicted graphically) revealed that, as expected, the largest positive values are found at relatively high temperatures and pressures and the smallest e_R's are found at relatively low temperatures and pressures. In comparing these values with those obtained by Dutton and Johnson (1967), it was noted that the magnitudes of the largest positive (+0.12) and negative (-0.20) efficiency factors were about half the size of those computed by Dutton and Johnson. This is due to the relatively small scale of the cyclone. The fact that $|e_R|$ is larger for the negative regional efficiency factors is due to the pressure effect, i.e. the denominator of e_R (p^K) for negative efficiency factors at low pressures is about half as large as that for positive e_R's at high pressures. This has certain implications concerning the contribution to the generation by each of the various diabatic components. For example, even though $|Q|$ for the latent heating in a region of relatively heavy precipitation in the warm air is usually much larger than $|Q|$ for infrared cooling in the cold air, the contribution to the generation of available potential energy, due to infrared cooling in the cold air is quite significant because of the large area involved.

It is also noteworthy to point out that according to the field of e_R calculated for the 10-13 March cyclone, most of the contribution to the generation of eddy available potential energy for a developing cyclone can be expected to come from the lateral boundary regions of the box. In these regions of large $|e_R|$, the appropriate distribution of Q (e.g. in the warm air latent heating at 800-500 mb and in the cold air infrared cooling through most of the profile except sensible heating near the surface) can lead to appreciable generation. In the central region about a growing cyclone this would not be expected since e_R is relatively small, especially at about 700-500 mb.

To further analyze the change of e_R with time, mean vertical profiles of e_R were constructed for 00 and 12 GMT of both cyclones by computing the area weighted mean e_R of all of the stations within the box for each standard 50 mb level. To reduce the number of diagrams and to facilitate discussion, the mean vertical profiles for individual synoptic times were combined, averaging the 00 and 12 GMT profiles for each day, except for the final profile in which three synoptic times were combined. If the reader wishes to view the mean e_R profiles, as well as those of

Q and G_R,[1] for the individual synoptic times, he will find them in the appendix. The results of these calculations show that the profile of $\bar{e}_R$ is relatively constant with respect to time, and that $\bar{e}_R$ decreases almost linearly with respect to pressure; see Figures 9 and 10. The exceptions, although not particularly prominent, involve a tendency for the profile of e_R for the second storm to become slightly less steep with pressure in the storm's later stage, Figure 10. This can be considered as an indication of a flattening of the isentropic surfaces. The other exception is the middle time period (March 3) for the first storm where the efficiency factor noticeably increased in the lower levels and actually remained nearly constant with pressure in the first 150 mb. This reflects an increasing slope of the θ surfaces during the first half of the first cyclone's history. Despite these slight exceptions the mean profiles of e_R for each entire cyclone are almost identical, Figure 11, indicating that the method chosen here for determining the boundaries of the region does not lead to sizable differences in the mean efficiency factors of the limited cyclone regions, regardless of the varying dimensions and shapes of the boxes enclosing the cyclones.

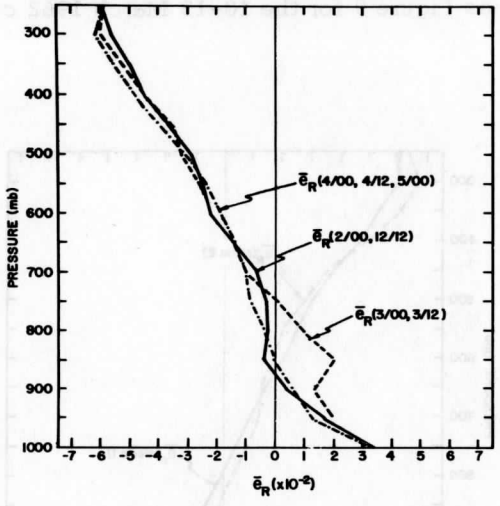

Figure 9. Averaged, as indicated, area weighted mean profiles of the regional efficiency factor, e_R, for the 2-5 March 1962 cyclone.

[1] Here and in the rest of the paper, the symbol G_{RR}, representing the generation of available potential energy inside the box using e_R, has been shortened to G_R.

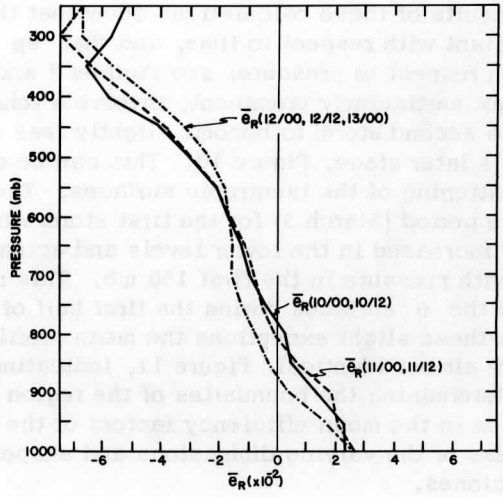

Figure 10. Same as Figure 9 for the 10-13 March 1962 cyclone.

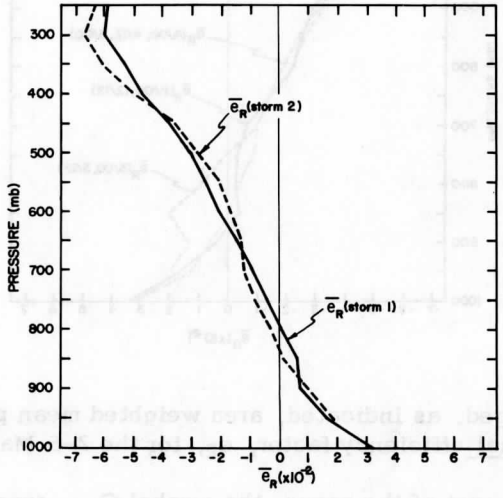

Figure 11. Mean profiles of e_R for the 2-5 March 1962 cyclone (storm 1) and the 10-13 March 1962 cyclone (storm 2).

B. The Heating Field

In addition to the field of regional efficiency factors, this study is also concerned with the calculation of the heating field. The heating term was evaluated at the 17 levels for each station using the first law of thermodynamics. These calculations, which were made by Smith (1967), essentially involved computing the difference between kinematic and adiabatic vertical velocities for each of the above grid points. Since the calculation of the kinematic vertical velocity, using horizontal wind data, is subject to large, cumulative errors at high elevations, there is some doubt as to the accuracy of these estimates near the top of the box.

To gain some insight of the heating field, mean vertical profiles of Q were prepared for each box of the 2-5 March cyclone and the 10-13 March cyclone; see Appendix B. They reveal large, unrealistic mean heating values in the upper levels (e.g. over 15°/day at 300 mb at 00 GMT on 10 March). Because of the unreliability of these estimates at high levels, discussions of the heating, and thus the generation, will be limited to levels below 500 mb. In the lower levels the profiles of the mean heating appear quite reasonable, depicting the dominance of sensible heating near the surface, and infrared cooling aloft.

The mean heating profiles for all the boxes of each storm, Figure 12, show cooling between 900 and 600 mb suggesting the dominance of infrared cooling over latent heating in this region. At first the dominance of infrared cooling may seem questionable; however, an inspection of the rainfall amounts within each box reveals that the areal mean precipitation, and thus the net latent heating, was quite limited. For example, for the 10-13 storm, an estimate of a mean precipitation rate for all the stations within the enclosed boxes of about 0.05 inches of rain per 12 hours would, if anything, be too high. Assuming that all the latent heat was distributed over a 400 mb layer, an upper limit of the mean heating due to latent heat release is about +1.6° per day which can be offset by a mean infrared cooling rate of -2.0° per day. The above values are means for entire storms. A check of the heating in regions of larger precipitation rates revealed that the individual profiles for these stations did indeed show warming. But since there were a limited number of stations within the box of this type, the contribution from such stations was limited, allowing the infrared cooling to dominate in the middle troposphere.

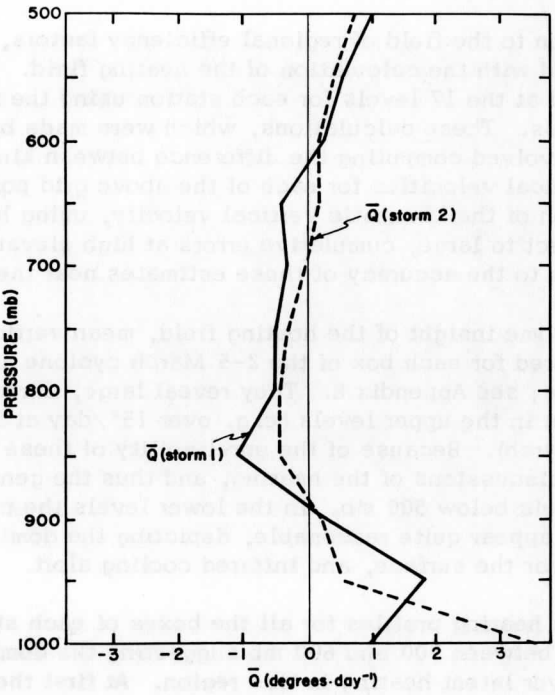

Figure 12. Mean profiles of Q for the 2-5 March 1962 cyclone (storm 1) and the 10-13 March 1962 cyclone (storm 2).

C. The Generation

The computation of the generation of available potential energy involves the integration of e_R and Q over the entire mass within the box. Because of the unreliable heating estimates at high altitudes, the discussion of the generation is confined to the region below 500 mb. For the analysis of the regional generation in the layer below 500 mb, mean profiles of Q and G_R for each cyclone were constructed by averaging (as was done for computing the mean regional efficiency factor as a function of pressure) the area weighted mean of Q and G_R for each time period, see Appendix B. In all of these vertical analyses, it is important to note that the mean of each of the terms was determined independently, and therefore $\bar{G}_R \neq \bar{e}_R\bar{Q}$, but rather $\bar{G}_R = \bar{e}_R\bar{Q} + \overline{e'_RQ'}$, where $(\bar{\ })$ denotes the area weighted mean on a pressure surface and $(\ )'$ denotes the deviations from that mean. The terms $\bar{e}_R\bar{Q}$ and $\overline{e'_RQ'}$ will be discussed later.

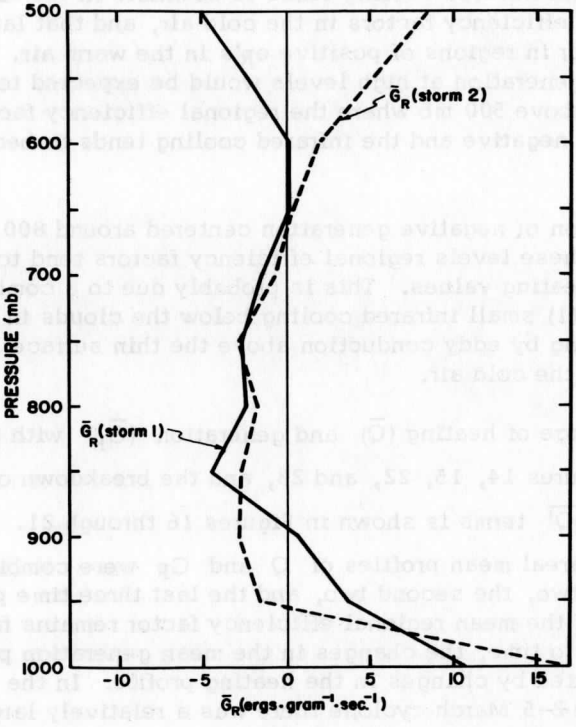

Figure 13. Mean profiles of G_R for the 2-5 March 1962 cyclone (storm 1) and the 10-13 March 1962 cyclone (storm 2).

As for the mean profiles of $\bar{G}_R$ for each of the cyclones, it can be seen in Figure 13 that there is a slight tendency for them to be parabolic, with maximum values of $\bar{G}_R$ near the surface and near 500 mb, with a region between about 700 mb and 900 mb of negative generation contributions. The positive generation contributions at the surface indicate that there is heating in regions of positive regional efficiency factors. The fact that G_R is positive in lower levels points out a difficulty that can arise when the Lorenz approximation equation is used to compute the generation term. With the generation computed by evaluating the covariance of T and Q, the cold air moving over the warm land would result in very negative generation computations due to sensible heating of the cold air by the ground. But when one employs the exact equation for calculating the eddy generation, the inclusion of the pressure effect makes the e_R's small but positive over most of the surface within the box, so that surface heating produces positive generation contributions.

The region of positive generation above 650-700 mb is probably due to the fact that infrared cooling tends to dominate in the regions of negative regional efficiency factors in the cold air, and that latent heating tends to occur in regions of positive e_R's in the warm air. This tendency for positive generation at high levels would be expected to be even more pronounced above 500 mb where the regional efficiency factors tend to become more negative and the infrared cooling tends to become more dominant.

The region of negative generation centered around 800 mb reveals the fact that at these levels regional efficiency factors tend to be opposite in sign to the heating values. This is probably due to a combination of two processes: (1) small infrared cooling below the clouds in the warm air and (2) heating by eddy conduction above the thin surface layer of positive e_R's in the cold air.

The change of heating ($\bar{Q}$) and generation ($\bar{G}_R$) with time are portrayed in Figures 14, 15, 22, and 23, and the breakdown of $\bar{G}_R$ into the $\bar{e}_R\bar{Q}$ and $\overline{e'_R Q'}$ terms is shown in Figures 16 through 21. As in the case of $\bar{e}_R$, the areal mean profiles of Q and G_R were combined by averaging the first two, the second two, and the last three time periods. Since the profile of the mean regional efficiency factor remains fairly constant with respect to time, the changes in the mean generation profile are mainly reflected by changes in the heating profile. In the beginning stages of the 2-5 March cyclone there was a relatively large vertical heating gradient (see Figure 14), with considerable heating at the surface and cooling aloft. With the e_R's decreasing almost linearly with pressure, such mean heating profiles tend to produce large positive generation contributions due to hydrostatic destabilization, i.e. $\int \bar{e}_R\bar{Q}\, dp$ is large. The initial vertical heating gradients of the 10-13 March cyclone (Figure 15) were considerably smaller than those for the 2-5 March cyclone because the second cyclone had matured somewhat over the eastern Pacific before the study of it was begun. As a result some upper level heating had already set in on 10 March. However, in each case as the cyclone matured, the heating became more positive in the upper levels (where $e_R < 0$) and, in the case of the first cyclone, less positive in the lower levels (where $e_R > 0$). These changes in the heating profile finally resulted in a near zero mean vertical heating gradient. As a result, the generation contribution due to hydrostatic destabilization became negative in the final stages of the cyclone, Figures 16 through 21.

In addition to vertical heating gradients, horizontal heating gradients were also very important, especially during the stages of the cyclone when the $e_R = 0$ isoline is almost vertical. The importance of the

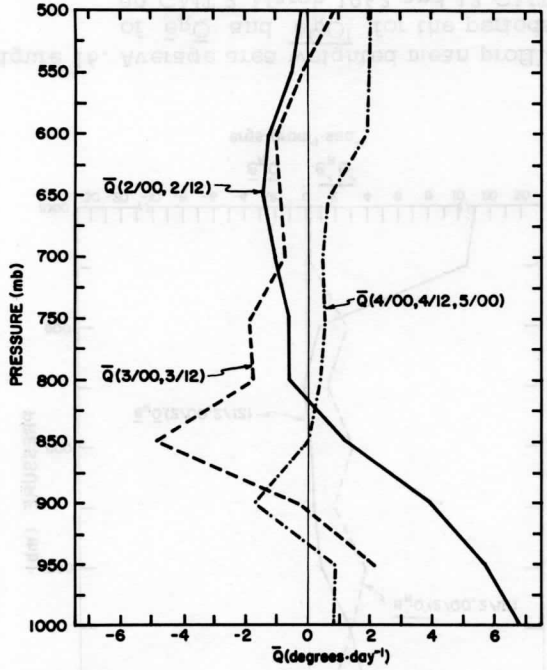

Figure 14. Averaged, as indicated, area weighted mean profiles of heating per unit mass, Q, for the 2-5 March 1962 cyclone.

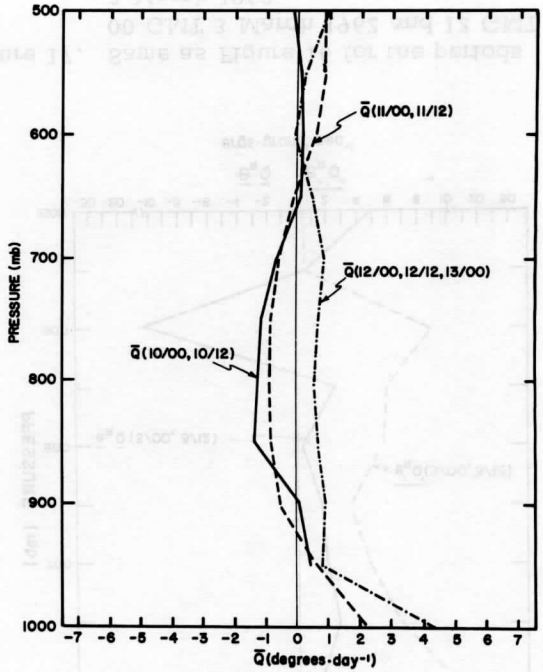

Figure 15. Same as Figure 14 for the 10-13 March 1962 cyclone.

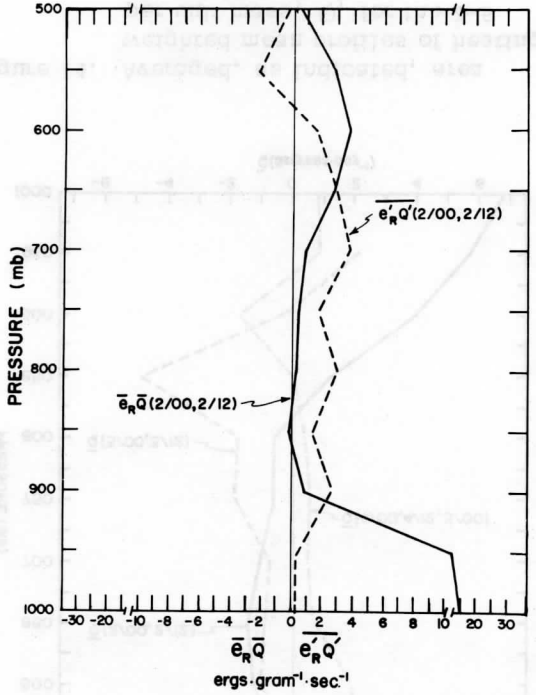

Figure 16. Average area weighted mean profiles of $\bar{e}_R \bar{Q}$ and $\overline{e'_R Q'}$ for the periods 00 GMT 2 March 1962 and 12 GMT 2 March 1962.

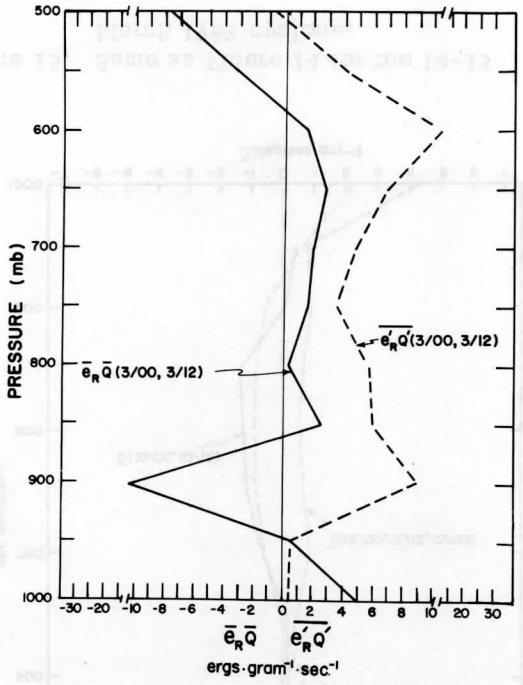

Figure 17. Same as Figure 16 for the periods 00 GMT 3 March 1962 and 12 GMT 3 March 1962.

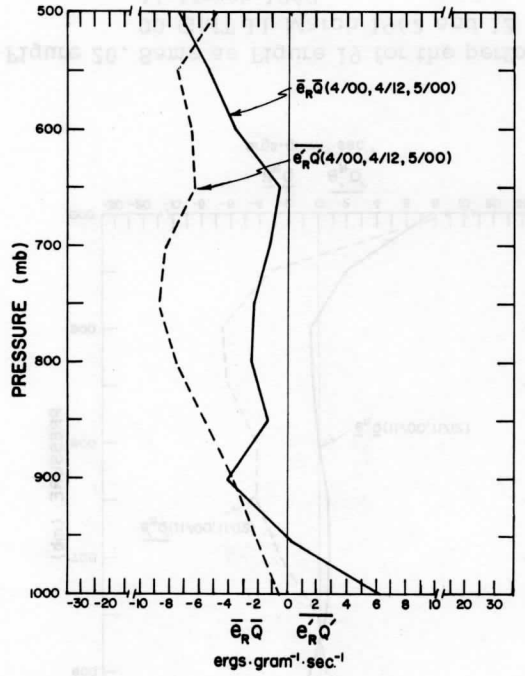

Figure 18. Same as Figure 16 for the periods 00 GMT 4 March 1962, 12 GMT 4 March 1962, and 00 GMT 5 March 1962.

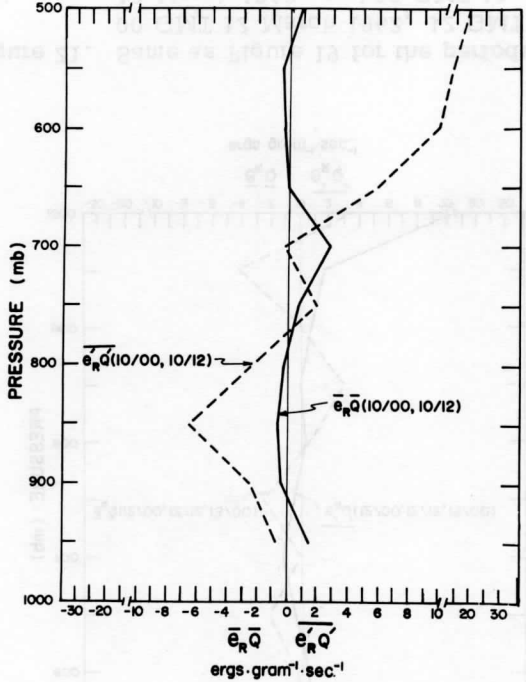

Figure 19. Average area weighted mean profiles of $\bar{e}_R\bar{Q}$ and $\overline{e'_R Q'}$ for the periods 00 GMT 10 March 1962 and 12 GMT 10 March 1962.

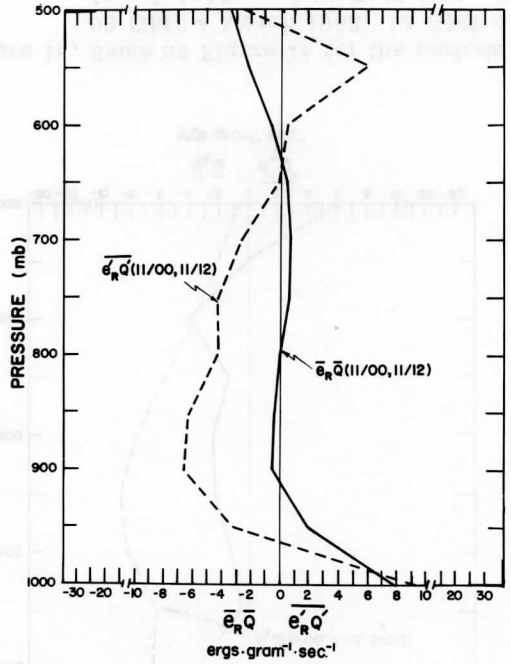

Figure 20. Same as Figure 19 for the periods 00 GMT 11 March 1962 and 12 GMT 11 March 1962.

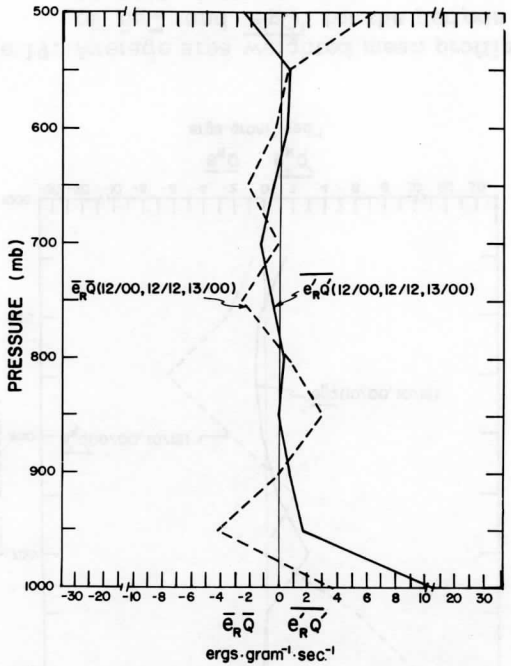

Figure 21. Same as Figure 19 for the periods 00 GMT 12 March 1962, 12 GMT 12 March 1962, and 00 GMT 13 March 1962.

horizontal gradient of heating for large generation contributions is illustrated by the large values of the covariance term $(\overline{e'_R Q'})$, dashed lines, in Figures 16 through 21. Early in the history of the 2-5 March cyclone, the value of the covariance term grows larger, indicating that there is a tendency for increased heating in the warm air at high pressure where $e'_R > 0$, and increased cooling in the cold air at low pressure where $e'_R < 0$. Because the second cyclone had matured somewhat before the study of it was begun, the largest values of $\overline{e'_R Q'}$ were calculated for the first time period. During the final, more occluded, stages of both cyclones when latent heat is being released in the cold air where $e'_R < 0$, the covariance term becomes negative. Therefore the horizontal heating gradients, as well as the vertical heating gradients, tend to contribute both to a cyclone's development and to its dissipation, Figure 22 and Figure 23.

To further analyze the generation term, the region was divided into two layers—surface to 750 mb (layer 1) and 750 to 500 mb (layer 2), and the generation term was then evaluated for each of these layers. One noticeable result is that the generation in layer 1 is only about half as large as that of layer 2. This is primarily due to the fact that layer 1 is much thinner than layer 2, because, for a low, particularly in mountain regions, the surface pressures are often as low as 800-850 mb.

The change of the generation of available potential energy, for the surface to 500 mb level, generally was followed by similar changes in central pressure of the cyclones, Figures 24 and 25. This might have been expected since available potential energy (defined by pressure deviations from a mean pressure on a potential temperature surface) is related directly to the baroclinicity found within the region studied. Perhaps even more significant is the fact that the generation estimates (except for the time periods centered on 11/00) are of the same sign as the corresponding changes in kinetic energy of the region. The magnitudes of the mean eddy generation and the change in kinetic energy being nearly equal (columns 4 and 5 of Table 1) indicates that the baroclinic conversion processes were probably significant, especially during the early stages of a cyclone's development.

The final aspect of this study concerns how the local generation contributes to the global supply of available potential energy. As a result of analyzing the approximations of the residual term in Equation 5, Figures 26 and 27 show that the local heating and cooling about these cyclones also made significant contributions to the global generation. For both cyclones there were initial periods of positive generation of global potential energy, followed by a single period of large negative global generation, coming at about the time that the cyclones showed signs of dissipating. These results again show that the diabatic term associated with the eddies studied here is of importance to the global energy budget.

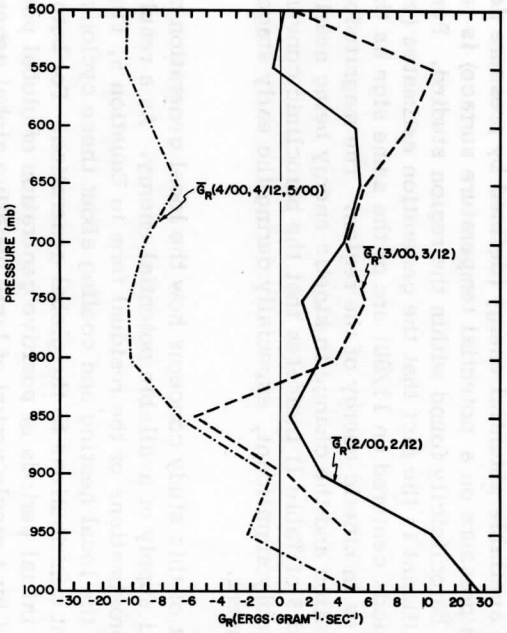

Figure 22. Averaged, as indicated, area weighted mean profiles of the regional generation, G_R, for the 2-5 March 1962 cyclone.

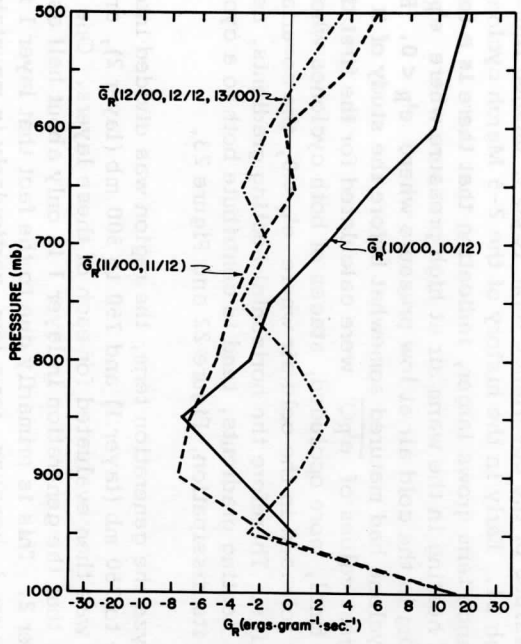

Figure 23. Same as Figure 22 for the 10-13 March 1962 cyclone.

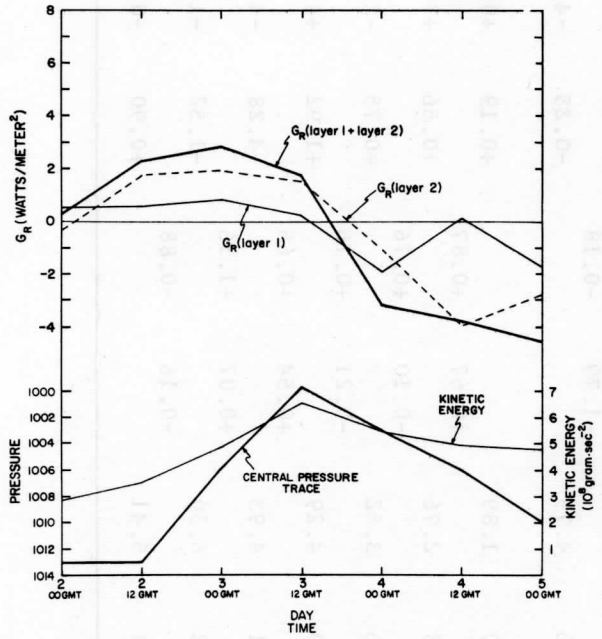

Figure 24. Time variation of the regional generation, G_R, the kinetic energy inside the box, and the central pressure of the 2-5 March 1962 cyclone.

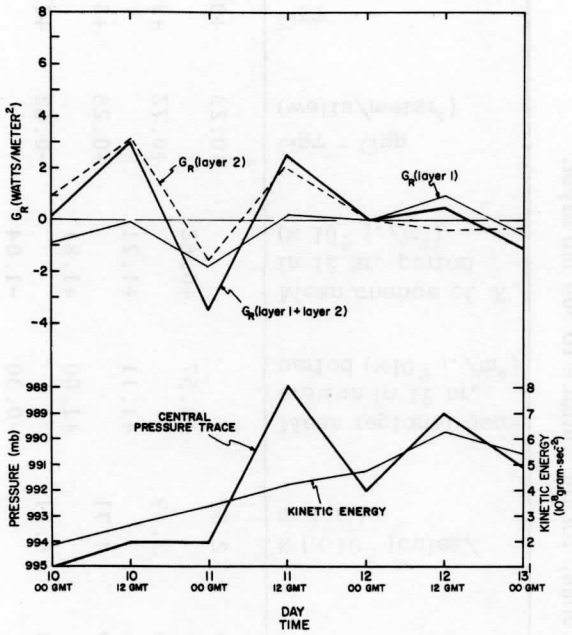

Figure 25. Time variation of the regional generation, G_R, the kinetic energy inside the box, and the central pressure of the 10-13 March 1962 cyclone.

Table 1. The calculated values of the various generation and kinetic energy terms, for the surface to 500 mb layer.

Day/time	G_R (watts/meter^2)	K ($\times 10^5$ joules/meter^2)	Mean regional generation in 12 hr. period ($\times 10^5$ j./m^2)	Mean change of K in 12 hr. period ($\times 10^5$ j./m^2)	$G_{RT} - G_{RR}$ (watts/meter^2)	G_{RT} (watts/meter^2)
2/00	+0.30	2.87			+0.23	+0.53
			+0.57	+0.62		
2/12	+2.34	3.49			+0.72	+3.06
			+1.11	+1.21		
3/00	+2.80	4.71			+0.25	+3.05
			+1.00	+1.81		
3/12	+1.83	6.51			-0.62	+1.20
			-0.30	-1.04		
4/00	-3.21	5.48			-2.32	-5.52
			-1.50	-0.51		
4/12	-3.73	4.97			+0.82	-2.91
			-1.79	-0.18		
5/00	-4.56	4.79			-0.25	-4.81
10/00	+0.10	1.89			+0.19	+0.29
			+0.67	+0.87		
10/12	+2.98	2.76			+0.56	+3.64
			-0.10	+0.76		
11/00	-3.46	3.52			+0.75	-2.71
			-0.21	+0.76		
11/12	+2.50	4.29			+1.92	+4.42
			+0.54	+0.65		
12/00	-0.01	4.93			-4.28	-4.29
			+0.07	+1.36		
12/12	+0.32	6.30			-1.52	-1.20
			-0.16	-0.88		
13/00	-1.08	5.41			+0.90	-0.18

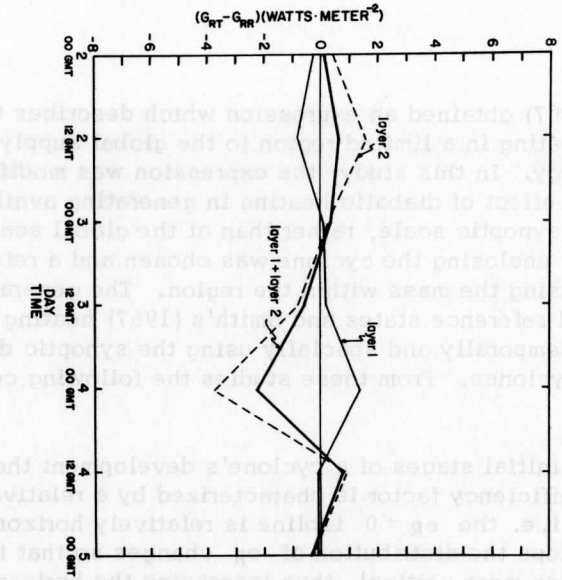

Figure 26. Time variation of the residual generation term, $G_{RT} - G_{RR}$, for the 2-5 March 1962 cyclone.

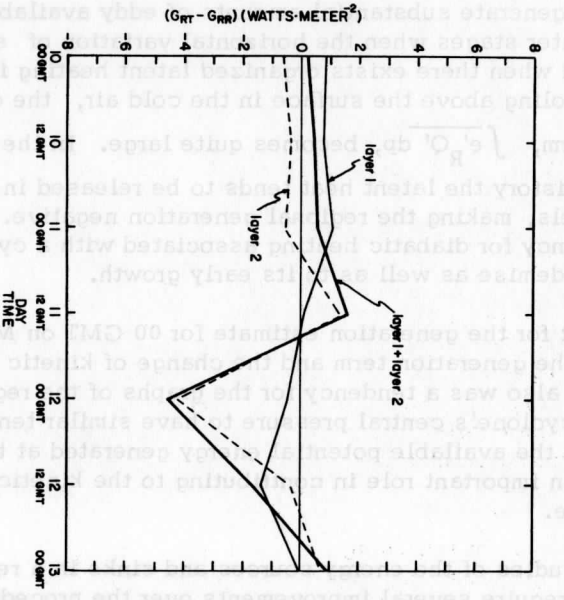

Figure 27. Same as Figure 26 for the 10-13 March 1962 cyclone.

V. Summary

Smith (1967) obtained an expression which describes the contribution of diabatic heating in a limited region to the global supply of available potential energy. In this study, the expression was modified so that it described the effect of diabatic heating in generating available potential energy at the synoptic scale, rather than at the global scale. To do this a local region enclosing the cyclone was chosen and a reference state was defined using the mass within the region. The generation based on these regional reference states and Smith's (1967) heating estimates was studied both temporally and spacially using the synoptic data for two March 1962 cyclones. From these studies the following conclusions have been reached:

1) In the initial stages of a cyclone's development the distribution of the regional efficiency factor is characterized by a relatively large vertical gradient, i.e. the $e_R = 0$ isoline is relatively horizontal. As the cyclone develops the distribution of e_R changes so that the $e_R = 0$ isoline becomes more vertical, thus increasing the horizontal variation of e_R. Finally, in the mature stages of the cyclone's history, the field of e_R became somewhat disorganized.

2) With the vertical gradients of e_R and Q being quite large during the beginning stages of a cyclone, the process of hydrostatic destabilization tends to generate substantial amounts of eddy available potential energy. In later stages when the horizontal variation of e_R increases somewhat and when there exists organized latent heating in the warm sector and cooling above the surface in the cold air, the covariance generation term, $\int \overline{e'_R Q'}\, dp$, becomes quite large. In the final stages of a cyclone's history the latent heat tends to be released in the cold air and at higher levels, making the regional generation negative. Thus there appears a tendency for diabatic heating associated with a cyclone to contribute to its demise as well as to its early growth.

3) Except for the generation estimate for 00 GMT on March 11, 1962, the signs of the generation term and the change of kinetic energy were the same. There also was a tendency for the graphs of the regional generation and the cyclone's central pressure to have similar tendencies. This suggests that the available potential energy generated at the synoptic scale plays an important role in contributing to the kinetic energy supply of the cyclone.

Future studies of the energy sources and sinks in a region about a cyclone will require several improvements over the procedures used here. One of the most important is the need for the improvement of the heating

estimates, especially above 500 mb. Perhaps this will be best accomplished by determining the generation of each of the heating components directly. Additional case studies of the generation term should involve comparing the generation estimates for deep, intense storms with those for storms that do not develop significantly. Another possible improvement might be obtained by allowing the dimensions and shape of the box to vary according to upper level contour patterns. Finally, there is an obvious need to compute the other terms of the energy equations using the regional reference state, and to compare such approximations with those of the eddy generation.

ACKNOWLEDGMENTS

The authors wish to express their appreciation to Dr. Phillip J. Smith for the heating calculations, to Dr. Donald R. Johnson and Dr. Benjamin R. Bullock for their enlightening discussion and comments, and to Stephen A. Newcombe for drafting the figures.

BIBLIOGRAPHY

Charney, J. G. (1947): The dynamics of long waves in a baroclinic westerly current. Journal of Meteorology, Vol. 4, No. 5, 135-162.

Corcoran, J. L., and L. H. Horn (1955): The role of synoptic scale variations of infrared radiation in the generation of available potential energy. Journal of Geophysical Research, Vol. 70, No. 18, 4521-4528.

Dutton, J. A., and D. R. Johnson (1967): The theory of available potential energy and a variational approach to atmospheric energetics. Advances in Geophysics, Vol. 12, Academic Press, New York, 333-436.

Eady, E. T. (1949): Long waves and cyclone waves. Tellus, Vol. 1, No. 3, 33-52.

Fjortoft, R. (1950): Application of integral theorems in deriving criteria of stability for laminar flows and for the baroclinic circular vortex. Geofys. Publikasjoner, Vol. 17, No. 5, 1-52.

Kuo, H. (1949): Dynamic instability of two-dimensional nondivergent flow in a barotropic atmosphere. Journal of Meteorology, Vol. 6, No. 2, 105-122.

Lorenz, E. N. (1955): Available potential energy and the maintenance of the general circulation. Tellus, Vol. 7, No. 2, 157-167.

Lorenz, E. N. (1955): Generation of available potential energy and the intensity of the general circulation. Large Scale Synoptic Processes, University of California (Los Angeles), Department of Meteorology, Final Report, J. Bjerknes, Project Director.

Oort, A. H. (1964): On estimates of the atmospheric energy cycle. Monthly Weather Review, Vol. 92, No. 11, 483-493.

Smith, P. J. (1967): Energy equations and their application to a limited region of the atmosphere. Ph. D. Thesis, University of Wisconsin.

Suomi, V. E. and W. C. Shen (1963): Horizontal variation of infrared cooling and the generation of eddy available potential energy. Journal of Atmospheric Sciences, Vol. 20, No. 1, 62-65.

TABLE OF SYMBOLS

Q	heating per unit mass
p	pressure
p_0	surface pressure
g	acceleration due to gravity
α	specific volume
c_p	specific heat of dry air at constant pressure
R_d	gas constant for dry air
K	R_d/c_p
T	absolute temperature
θ	potential temperature
θ_t	potential temperature at the top of the atmosphere
t	time

$\vec{V}$ horizontal wind vector

ω dp/dt

∇_p horizontal del operator on a constant pressure surface

R surface area of the region inside the box

S surface area of the earth

$\bar{p}(\theta)$ global mean pressure of the potential temperature surface

$p_R(\theta)$ regional mean pressure of the potential temperature surface

e_T efficiency factor using $\bar{p}(\theta)$

e_R efficiency factor using $p_R(\theta)$

A available potential energy

G_{RT} generation of available potential energy inside the box using e_T

G_{RR} generation of available potential energy inside the box using e_R

G_R same as G_{RR}

$\bar{(\ )}$ area weighted mean on a pressure surface

$(\cdot)'$ deviations from the area weighted mean on a pressure surface

$\bar{(\ )}$ (aa/jj, bb/kk) time average of area weighted mean on a pressure surface for time jj GMT on day aa and time kk GMT on day bb

APPENDIX A

Surface synoptic maps at 00Z and 12Z corresponding to the times for which generation calculations were made. Also included are the approximate lateral boundaries of the box which were chosen according to criteria defined in this paper. Solid boundary lines indicate areas where the specified criteria were used. Dashed lines indicate boundaries which did not meet the specified criteria for one of many, usually obvious, reasons.

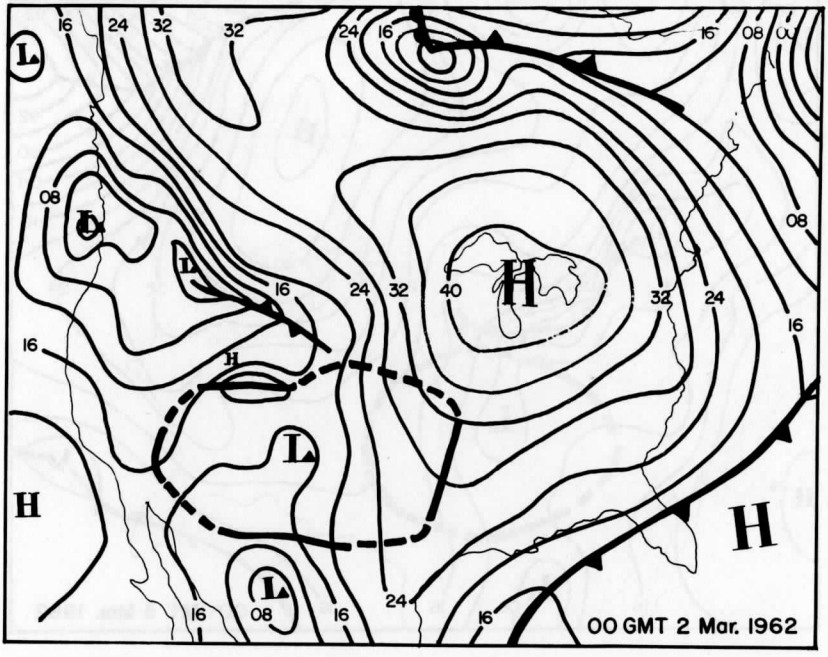
00 GMT 2 Mar. 1962

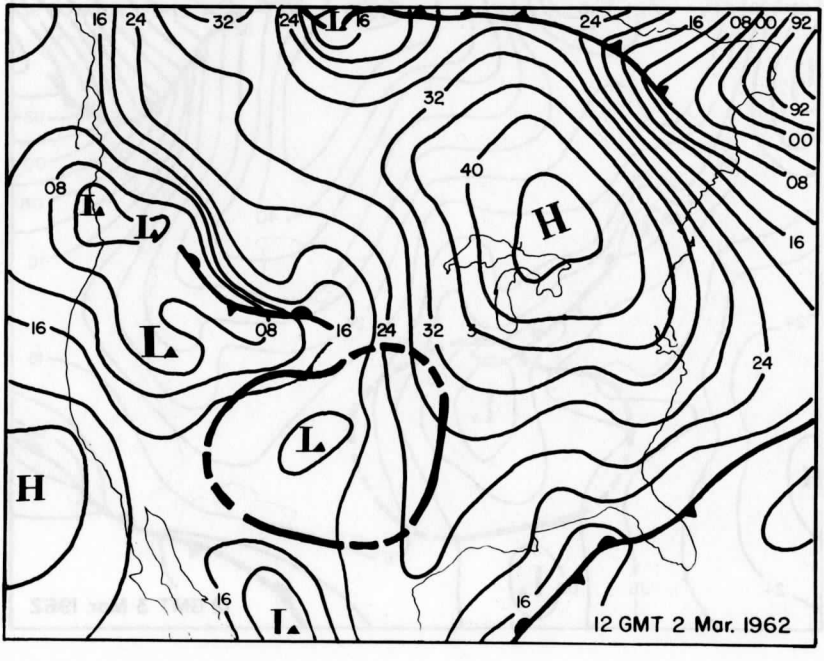
12 GMT 2 Mar. 1962

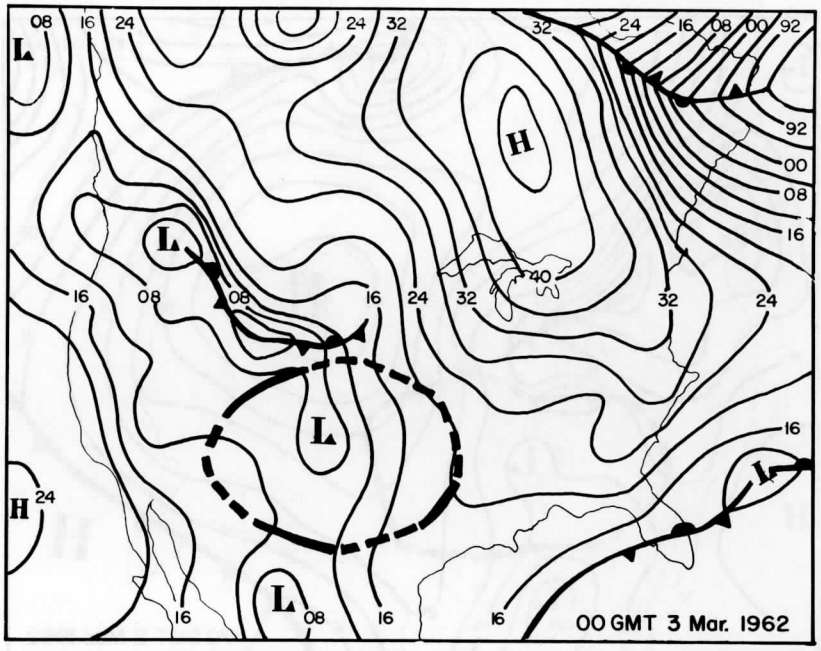
00 GMT 3 Mar. 1962

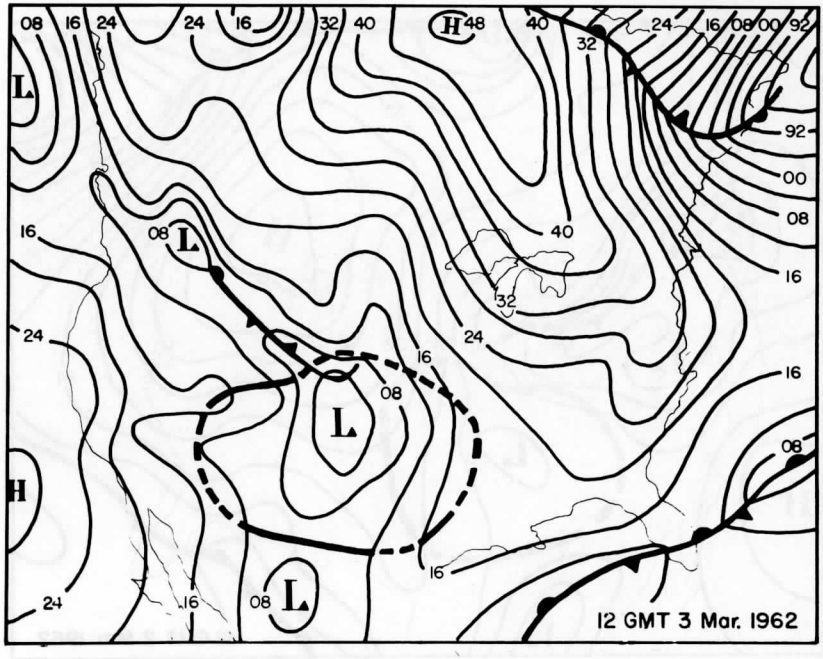
12 GMT 3 Mar. 1962

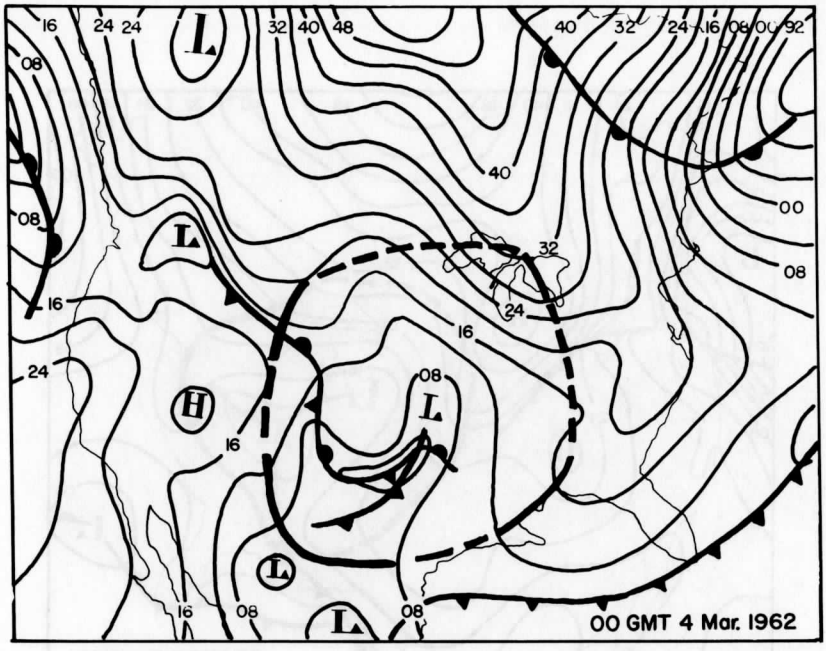
00 GMT 4 Mar. 1962

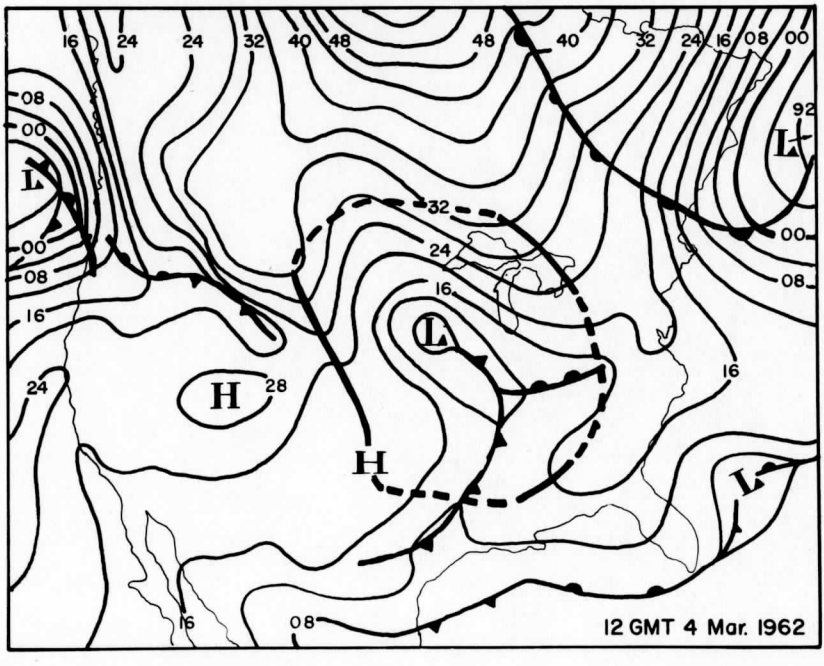
12 GMT 4 Mar. 1962

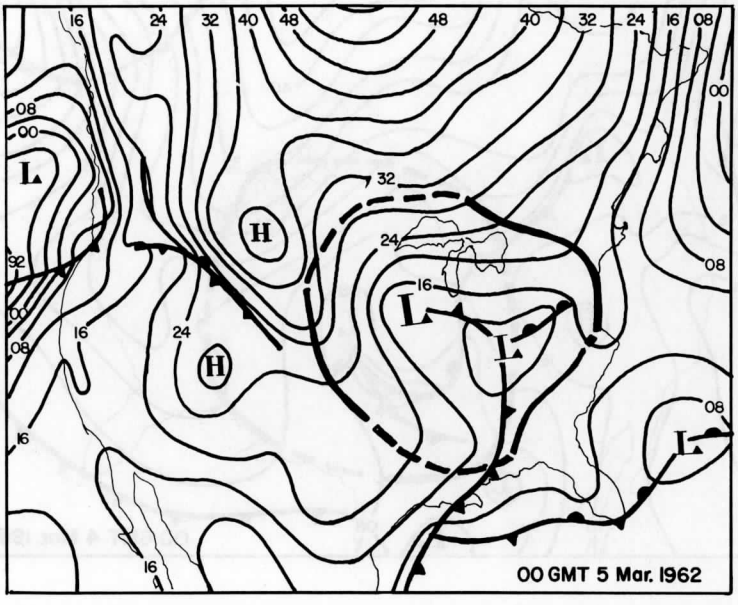
16
24
32
40
48
48
40
32
24
16
08
00
08
00
L
H
32
24
16
L
L
08
32
00
08
16
24
H
16
08
L
16
00 GMT 5 Mar. 1962

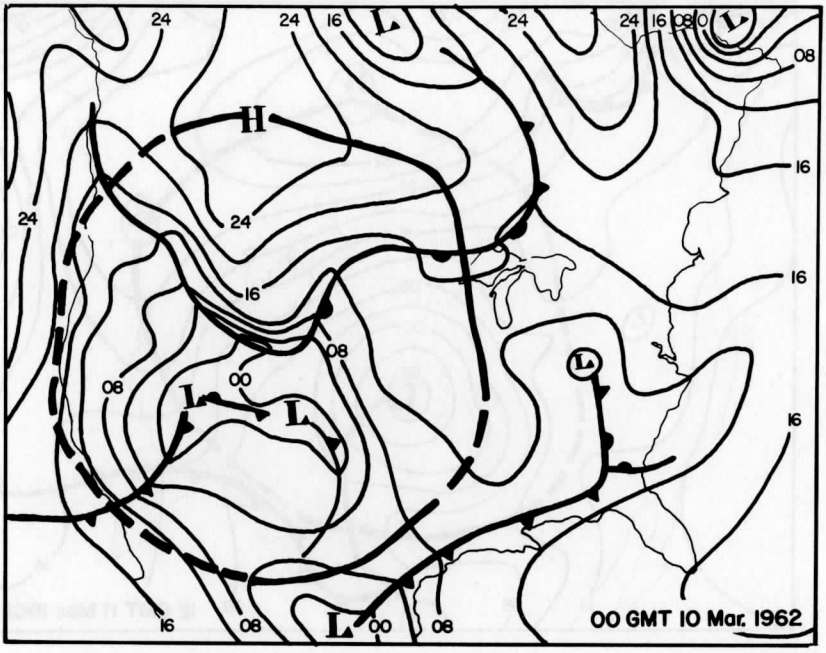
24
24
16
L
24
24
16
08
00
L
08
H
16
24
24
16
16
08
08
00
L
L
L
16
16
08
00
08
L
16
00 GMT 10 Mar. 1962

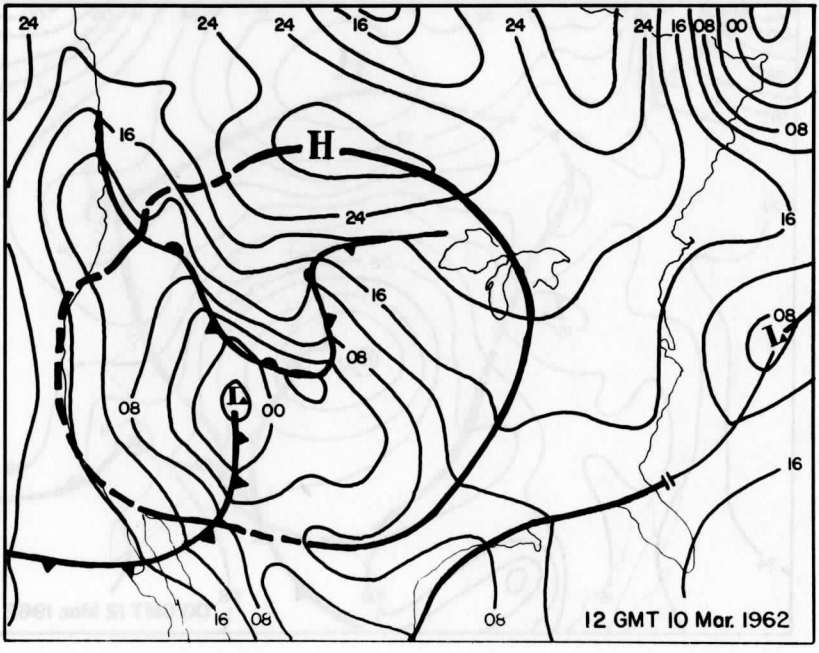
24
24
24
16
24
24
16
08
00
08
16
H
24
16
16
08
08
L
00
08
L
16
16
08
08
12 GMT 10 Mar. 1962

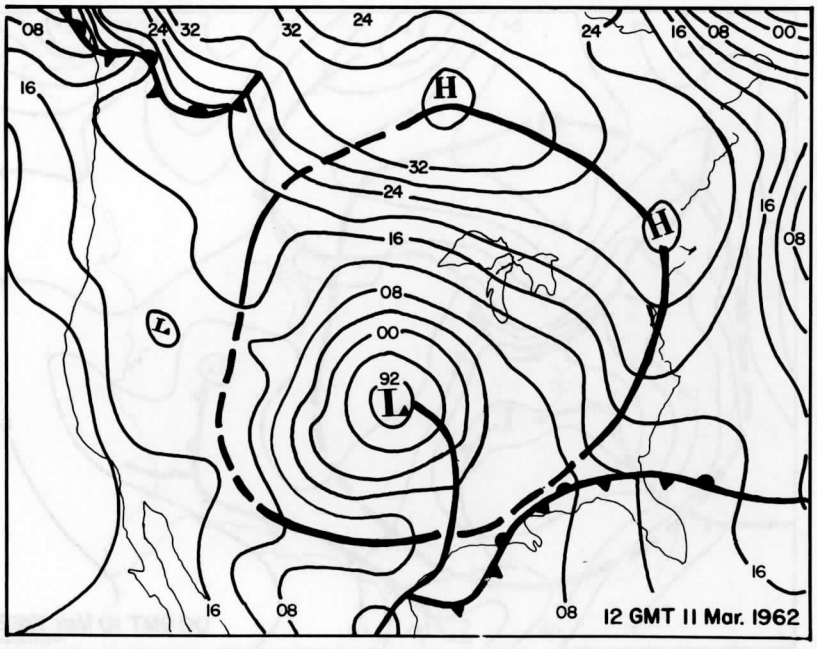
H
H
L
L
92
12 GMT 11 Mar. 1962

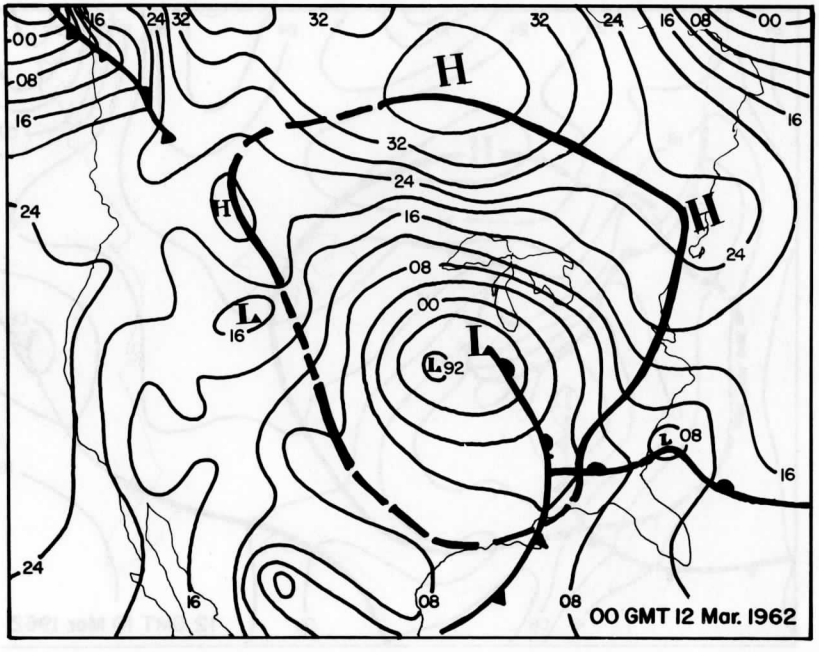
H
H
H
L
L
L
92
00 GMT 12 Mar. 1962

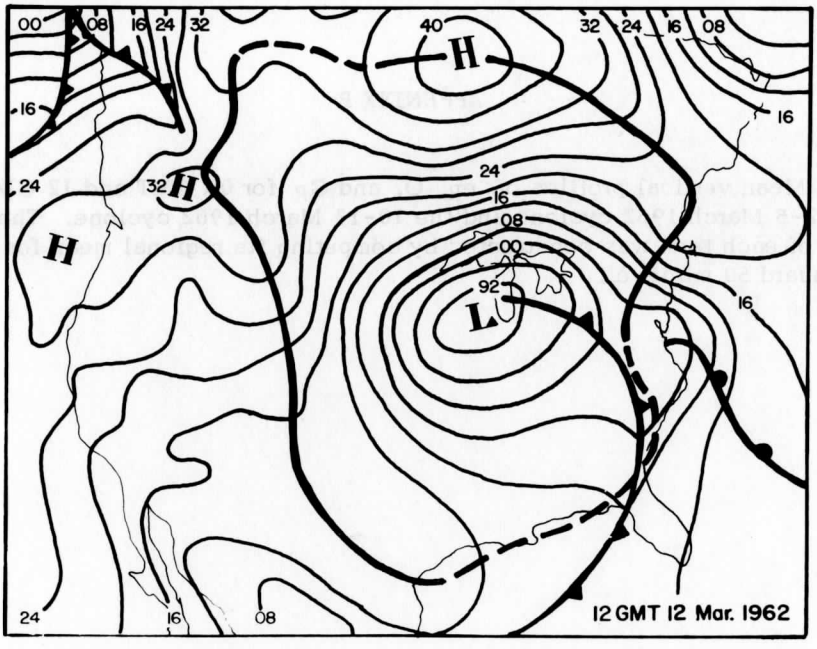
00
08
16
24
32
40
H
32
24
16
08
16
24
32
H
H
24
16
08
00
92
L
16
24
16
08
12 GMT 12 Mar. 1962

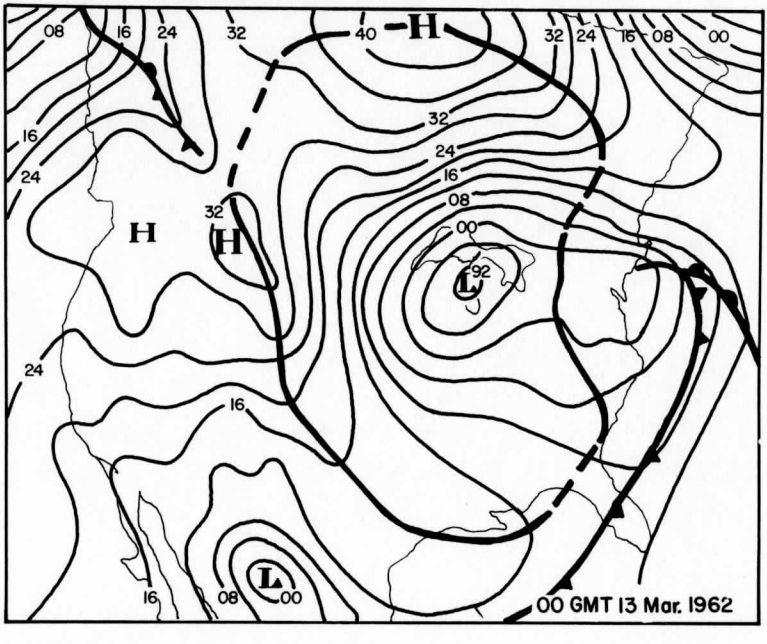
08
16
24
32
40
H
32
24
16
08
00
32
16
24
24
16
08
32
00
H
H
92
L
24
16
16
08
L
00
00 GMT 13 Mar. 1962

APPENDIX B

Mean vertical profiles of e_R, Q, and G_R for 00 GMT and 12 GMT of the 2-5 March 1962 cyclone and the 10-13 March 1962 cyclone. The profile of each term was constructed by computing its regional mean for each standard 50 mb level.

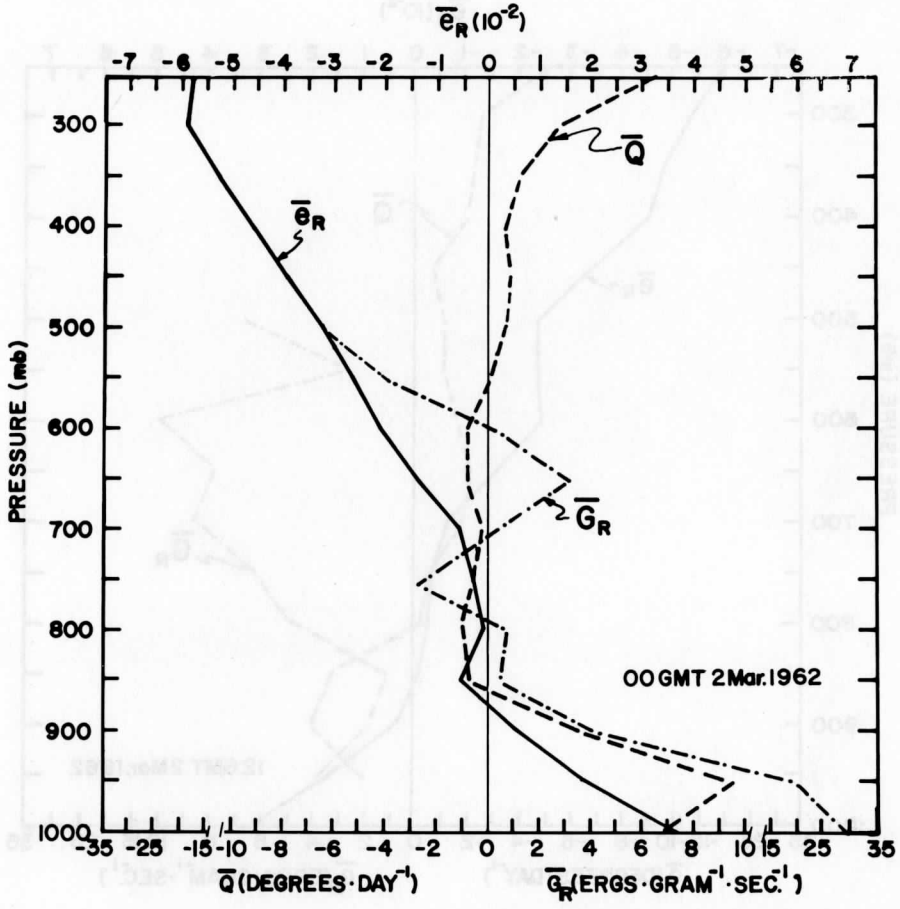
$\overline{e}_R (10^{-2})$
-7 -6 -5 -4 -3 -2 -1 0 1 2 3 4 5 6 7
300
400
500
600
700
800
900
1000
PRESSURE (mb)
$\overline{Q}$
$\overline{e}_R$
$\overline{G}_R$
00 GMT 2 Mar. 1962
-35 -25 -15 -10 -8 -6 -4 -2 0 2 4 6 8 10 15 25 35
$\overline{Q}$ (DEGREES · DAY^{-1})
$\overline{G}_R$ (ERGS · GRAM^{-1} · SEC.$^{-1}$)

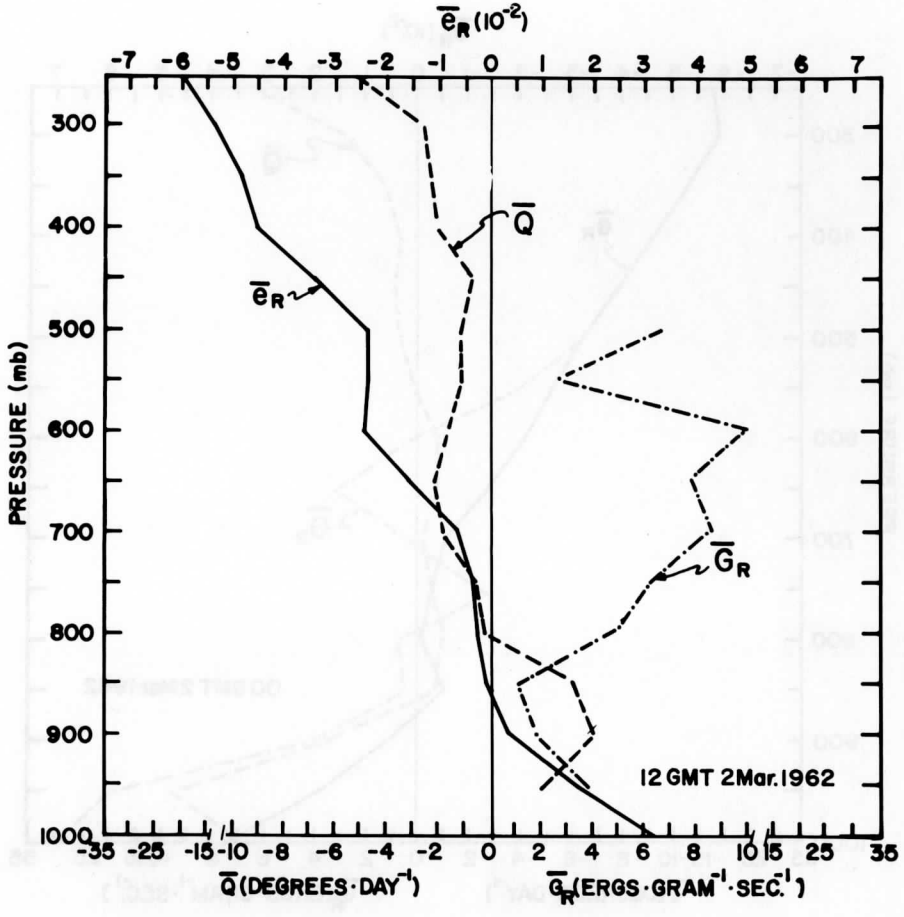
$\overline{e}_R(10^{-2})$
-7 -6 -5 -4 -3 -2 -1 0 1 2 3 4 5 6 7
300
400
500
600
700
800
900
1000
PRESSURE (mb)
$\overline{Q}$
$\overline{e}_R$
$\overline{G}_R$
12 GMT 2Mar.1962
-35 -25 -15 -10 -8 -6 -4 -2 0 2 4 6 8 10 15 25 35
$\overline{Q}$(DEGREES·DAY^{-1})
$\overline{G}_R$(ERGS·GRAM^{-1}·SEC.$^{-1}$)

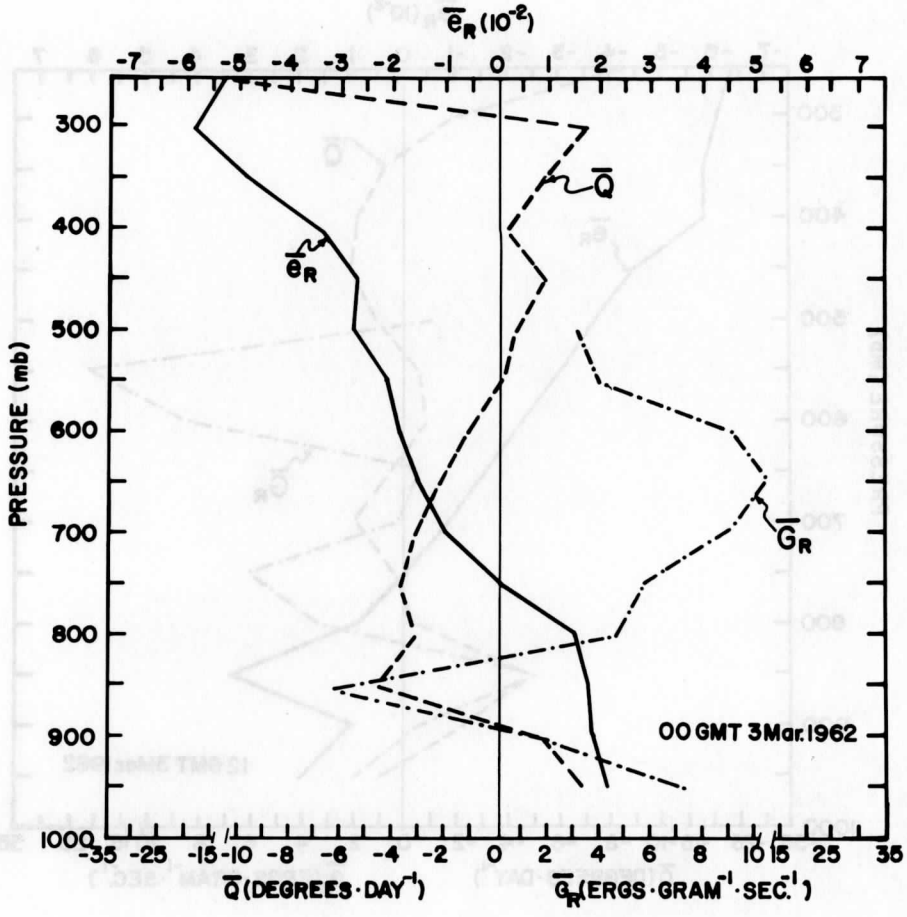
$\overline{e}_R$ (10^{-2})
-7 -6 -5 -4 -3 -2 -1 0 1 2 3 4 5 6 7
300
400
500
600
700
800
900
1000
PRESSURE (mb)
$\overline{Q}$
$\overline{e}_R$
$\overline{G}_R$
00 GMT 3 Mar. 1962
-35 -25 -15 -10 -8 -6 -4 -2 0 2 4 6 8 10 15 25 35
$\overline{Q}$ (DEGREES · DAY^{-1})
$\overline{G}_R$ (ERGS · GRAM^{-1} · SEC.$^{-1}$)

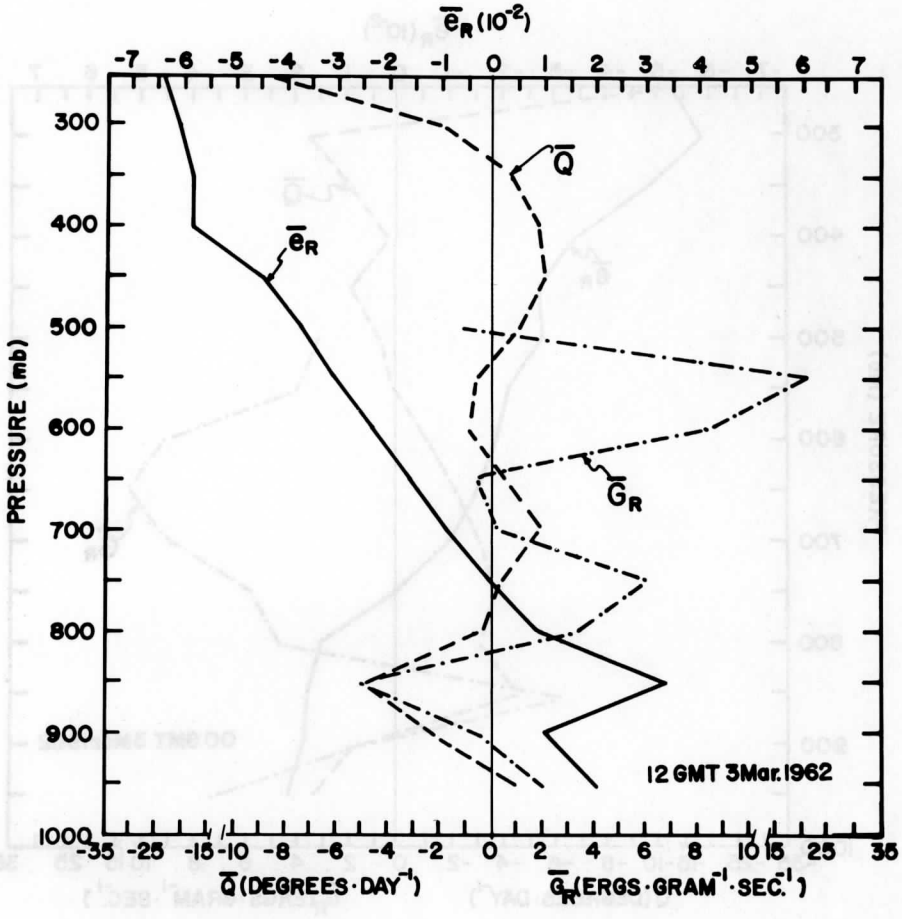
$\bar{e}_R(10^{-2})$
-7 -6 -5 -4 -3 -2 -1 0 1 2 3 4 5 6 7
300
400
500
600
700
800
900
1000
PRESSURE (mb)
$\bar{Q}$
$\bar{e}_R$
$\bar{G}_R$
12 GMT 3Mar.1962
-35 -25 -15 -10 -8 -6 -4 -2 0 2 4 6 8 10 15 25 35
$\bar{Q}$(DEGREES·DAY^{-1})
$\bar{G}_R$(ERGS·GRAM^{-1}·SEC.$^{-1}$)

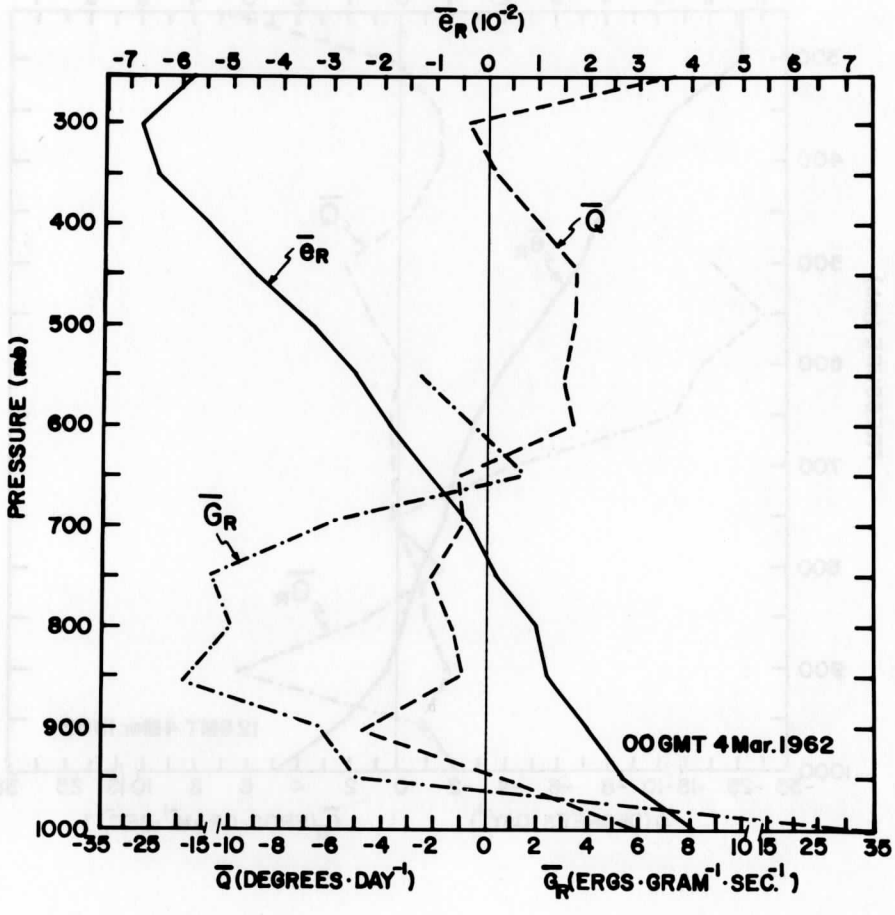
$\bar{\theta}_R(10^{-2})$
-7 -6 -5 -4 -3 -2 -1 0 1 2 3 4 5 6 7
300
400
500
600
700
800
900
1000
PRESSURE (mb)
$\bar{\theta}_R$
$\bar{Q}$
$\bar{G}_R$
00 GMT 4 Mar. 1962
-35 -25 -15 -10 -8 -6 -4 -2 0 2 4 6 8 10 15 25 35
$\bar{Q}$(DEGREES·DAY^{-1})
$\bar{G}_R$(ERGS·GRAM^{-1}·SEC.$^{-1}$)

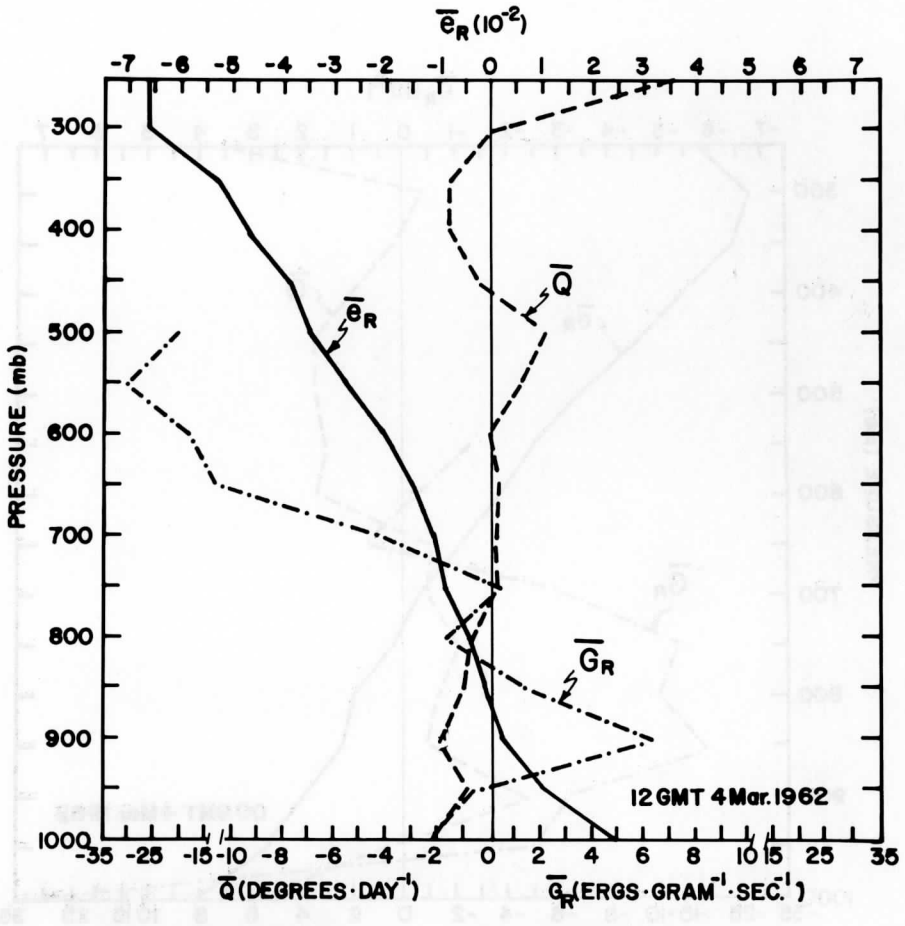
$\overline{e}_R(10^{-2})$
-7 -6 -5 -4 -3 -2 -1 0 1 2 3 4 5 6 7
300
400
500
600
700
800
900
1000
PRESSURE (mb)
$\overline{e}_R$
$\overline{Q}$
$\overline{G}_R$
12 GMT 4 Mar. 1962
-35 -25 -15 -10 -8 -6 -4 -2 0 2 4 6 8 10 15 25 35
$\overline{Q}$(DEGREES·DAY^{-1})
$\overline{G}_R$(ERGS·GRAM^{-1}·SEC.$^{-1}$)

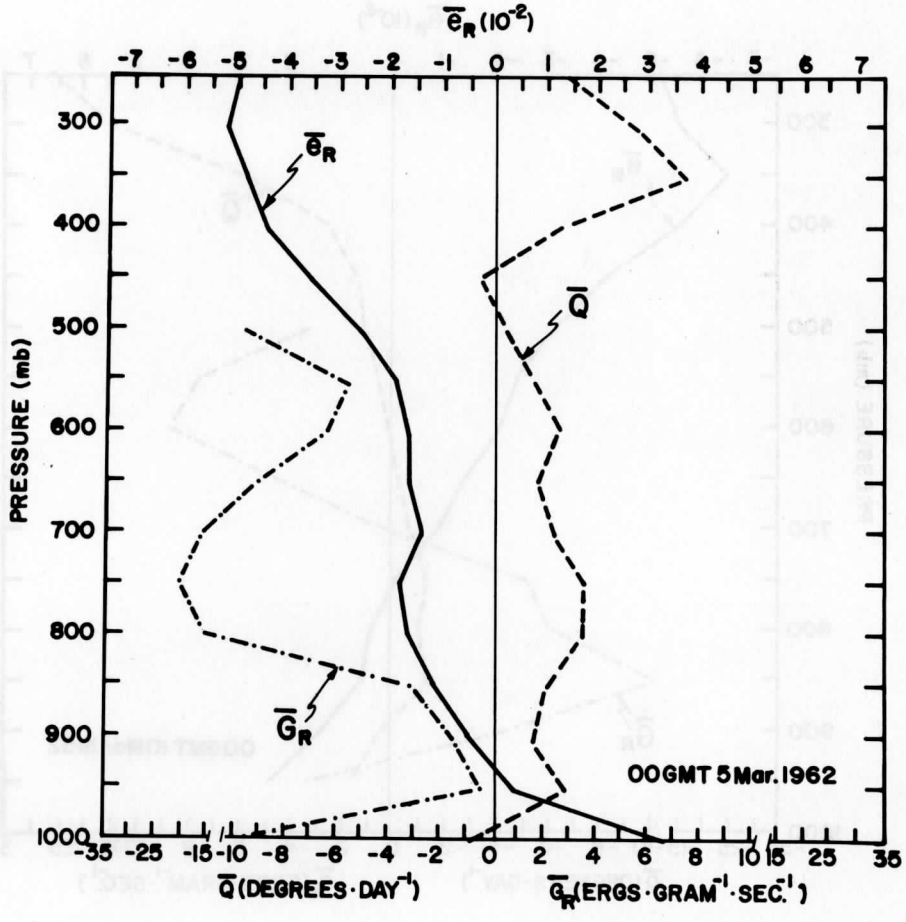
$\bar{e}_R(10^{-2})$
-7 -6 -5 -4 -3 -2 -1 0 1 2 3 4 5 6 7
300
400
500
600
700
800
900
1000
PRESSURE (mb)
$\bar{e}_R$
$\bar{Q}$
$\bar{G}_R$
00GMT 5Mar.1962
-35 -25 -15 -10 -8 -6 -4 -2 0 2 4 6 8 10 15 25 35
$\bar{Q}$(DEGREES·DAY^{-1})
$\bar{G}_R$(ERGS·GRAM^{-1}·SEC.$^{-1}$)

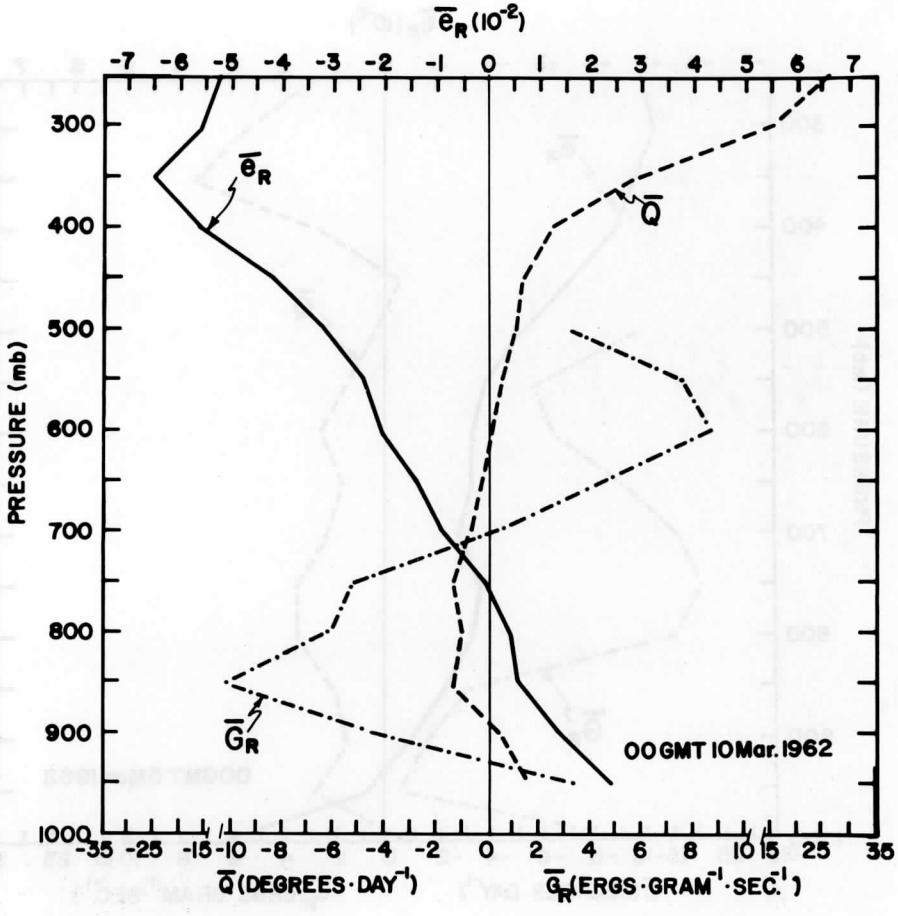
$\bar{e}_R(10^{-2})$
-7 -6 -5 -4 -3 -2 -1 0 1 2 3 4 5 6 7
300
400
500
600
700
800
900
1000
PRESSURE (mb)
$\bar{e}_R$
$\bar{Q}$
$\bar{G}_R$
00 GMT 10 Mar. 1962
-35 -25 -15 -10 -8 -6 -4 -2 0 2 4 6 8 10 15 25 35
$\bar{Q}$ (DEGREES · DAY^{-1})
$\bar{G}_R$ (ERGS · GRAM^{-1} · SEC.$^{-1}$)

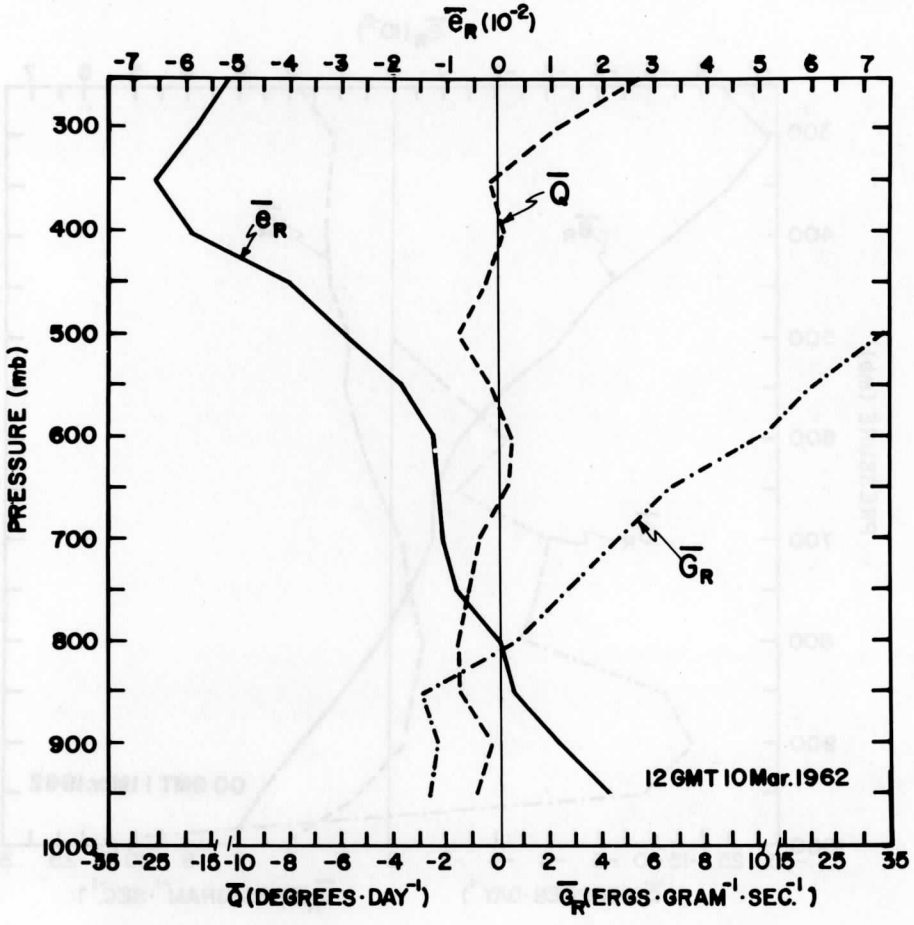
$\overline{e}_R(10^{-2})$
-7 -6 -5 -4 -3 -2 -1 0 1 2 3 4 5 6 7
300
400
500
600
700
800
900
1000
PRESSURE (mb)
$\overline{e}_R$
$\overline{Q}$
$\overline{G}_R$
12 GMT 10 Mar. 1962
-35 -25 -15 -10 -8 -6 -4 -2 0 2 4 6 8 10 15 25 35
$\overline{Q}$ (DEGREES · DAY^{-1})
$\overline{G}_R$ (ERGS · GRAM^{-1} · SEC.$^{-1}$)

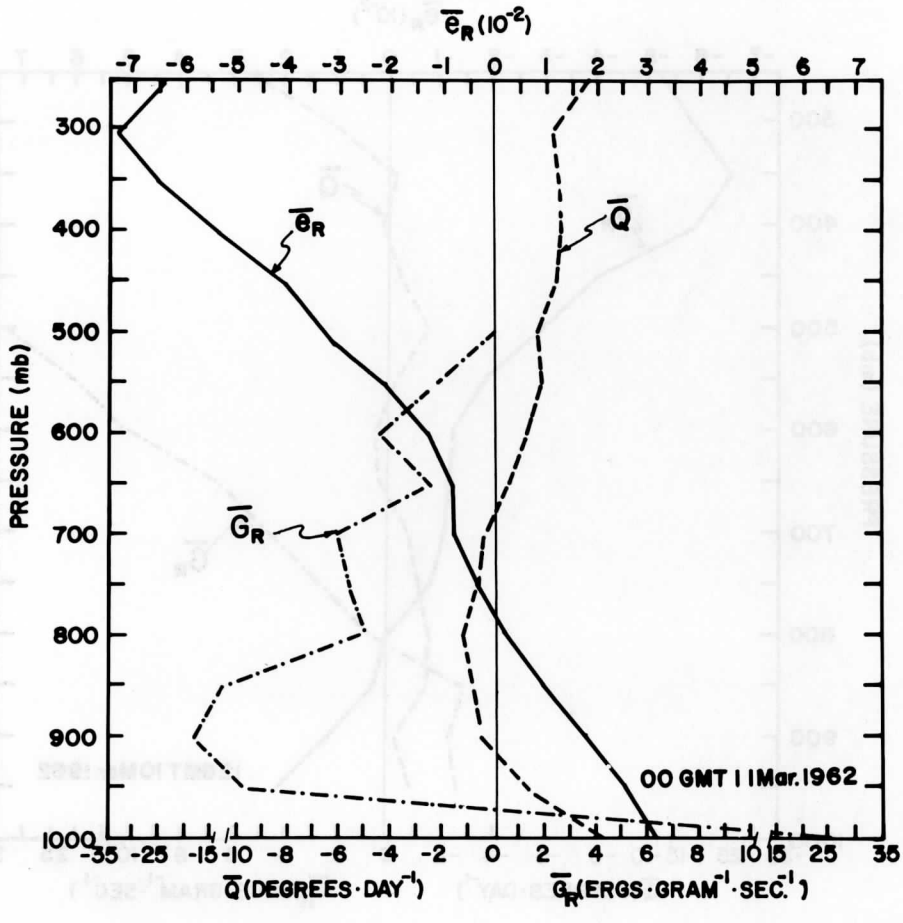
$\overline{e}_R(10^{-2})$
-7 -6 -5 -4 -3 -2 -1 0 1 2 3 4 5 6 7
300
400
500
600
700
800
900
1000
PRESSURE (mb)
$\overline{\theta}_R$
$\overline{Q}$
$\overline{G}_R$
00 GMT 11 Mar. 1962
-35 -25 -15 -10 -8 -6 -4 -2 0 2 4 6 8 10 15 25 35
$\overline{Q}$(DEGREES·DAY^{-1})
$\overline{G}_R$(ERGS·GRAM^{-1}·SEC.$^{-1}$)

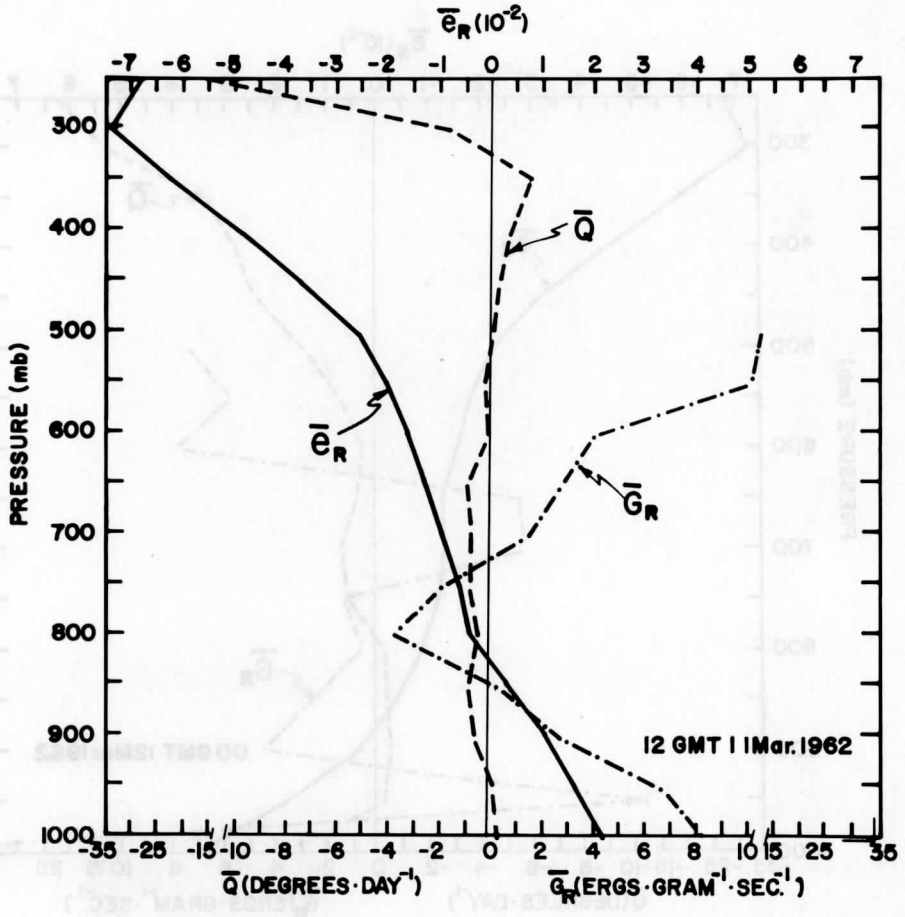
$\bar{e}_R(10^{-2})$
-7 -6 -5 -4 -3 -2 -1 0 1 2 3 4 5 6 7
300
400
500
600
700
800
900
1000
PRESSURE (mb)
$\bar{Q}$
$\bar{e}_R$
$\bar{G}_R$
12 GMT 11 Mar. 1962
-35 -25 -15 -10 -8 -6 -4 -2 0 2 4 6 8 10 15 25 35
$\bar{Q}$(DEGREES·DAY^{-1})
$\bar{G}_R$(ERGS·GRAM^{-1}·SEC.$^{-1}$)

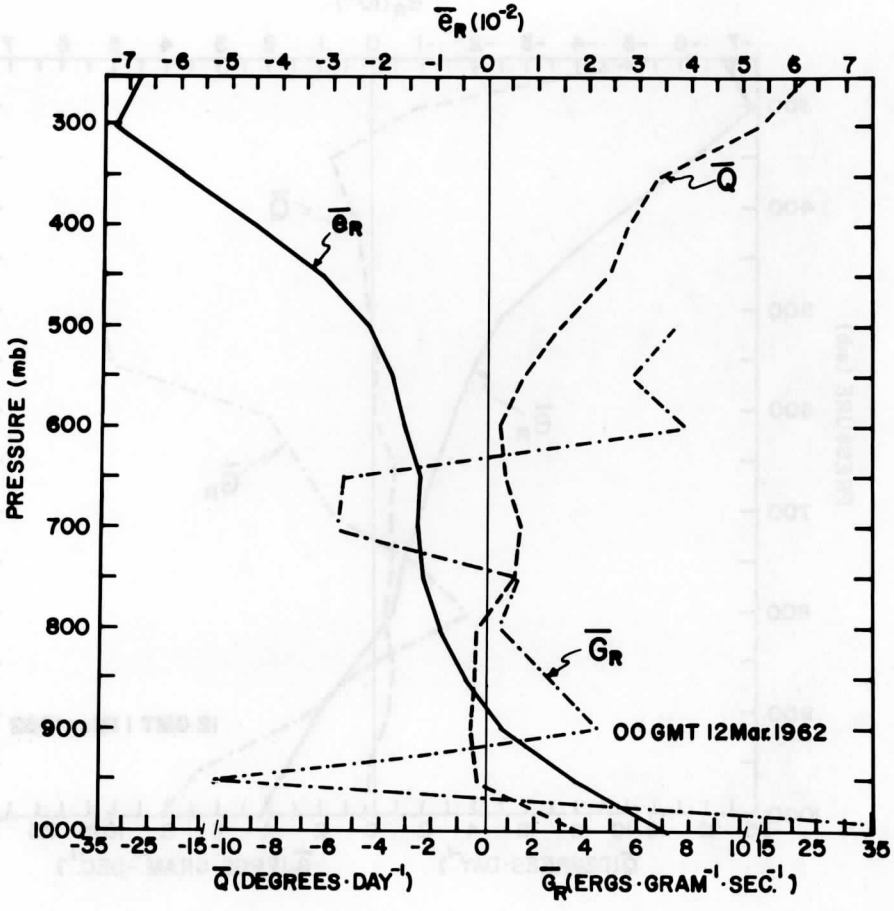
$\overline{e}_R (10^{-2})$
-7 -6 -5 -4 -3 -2 -1 0 1 2 3 4 5 6 7
300
400
500
600
700
800
900
1000
PRESSURE (mb)
$\overline{e}_R$
$\overline{Q}$
$\overline{G}_R$
00 GMT 12 Mar. 1962
-35 -25 -15 -10 -8 -6 -4 -2 0 2 4 6 8 10 15 25 35
$\overline{Q}$ (DEGREES · DAY^{-1})
$\overline{G}_R$ (ERGS · GRAM^{-1} · SEC^{-1})

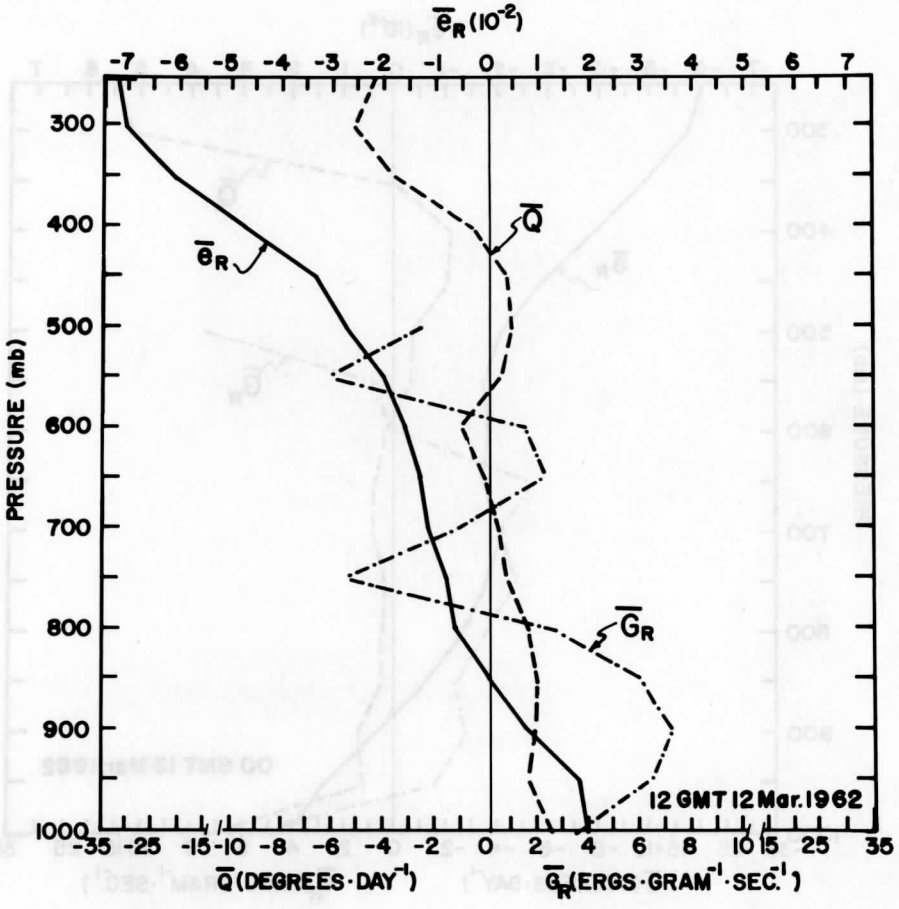
$\overline{e}_R(10^{-2})$
-7 -6 -5 -4 -3 -2 -1 0 1 2 3 4 5 6 7
300
400
500
600
700
800
900
1000
PRESSURE (mb)
$\overline{e}_R$
$\overline{Q}$
$\overline{G}_R$
12 GMT 12 Mar. 1962
-35 -25 -15 -10 -8 -6 -4 -2 0 2 4 6 8 10 15 25 35
$\overline{Q}$(DEGREES·DAY^{-1})
$\overline{G}_R$(ERGS·GRAM^{-1}·SEC^{-1})

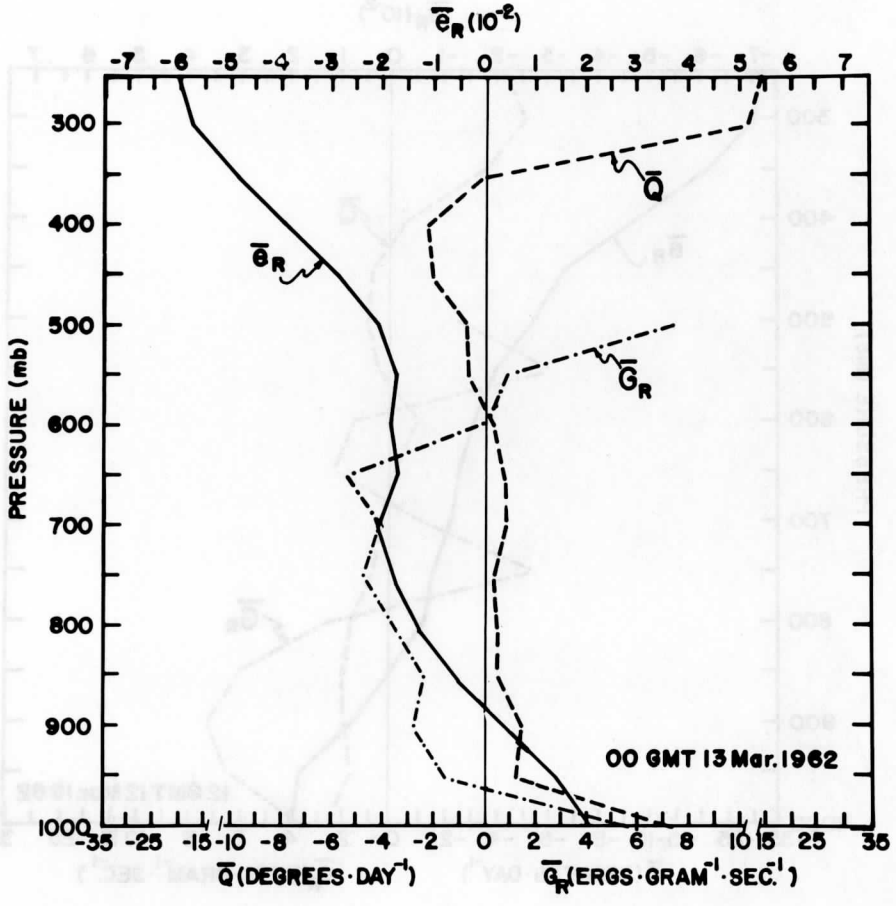
$\bar{e}_R(10^{-2})$
-7 -6 -5 -4 -3 -2 -1 0 1 2 3 4 5 6 7
300
400
500
600
700
800
900
1000
PRESSURE (mb)
$\bar{e}_R$
$\bar{Q}$
$\bar{G}_R$
00 GMT 13 Mar. 1962
-35 -25 -15 -10 -8 -6 -4 -2 0 2 4 6 8 10 15 25 35
$\bar{Q}$(DEGREES·DAY^{-1})
$\bar{G}_R$(ERGS·GRAM^{-1}·SEC.$^{-1}$)

A STUDY OF THE INDIAN MONSOON USING SATELLITE MEASURED ALBEDO AND LONG WAVE RADIATION

by

Gerald J. Dittberner
Frank Sechrist

ABSTRACT:

Thirty months of continuous low resolution satellite data, emitted long wave radiation and albedo are used to study the Indian monsoon. These data, combined with rainfall data for the Indian subcontinent, are employed to develop an intensity index which provides the first quantitative measure of monsoon intensity. Three monsoons are studied: the 1963 monsoon, the strong 1964 monsoon and the very weak 1965 monsoon. Intensity differences show up most dramatically on the intensity index maps. The time history of the 1964 and 1965 monsoons are examined showing how the intense cloudiness of the 1964 monsoon lingered on for a number of months apparently reducing surface heating significantly preceding the weak 1965 monsoon. Typical values of the intensity index, long wave radiation and albedo are compiled for each season of the year preceding the 1964 and 1965 monsoons. Finally, the monsoon is described in terms of radiation depicting certain recurring, quasi-steady state, seasonal features.

1. Introduction

The term "monsoon," according to Webster, is "a periodic wind, especially in the Indian Ocean and southern Asia; also, the rainy season of the southwest monsoon in India." The word is derived from the obsolete Arabic "Mausim," the Dutch "Monssoen," and the Portuguese "Mancao" meaning "a time, a season."

Predicting the monsoon onset is still one of the most challenging problems in meteorology. Rainfall during the southwest monsoon season (June to September) is extremely important to the agriculture of India and the economy of the country (Pant (1964) and Shamshad (1966)). In fact, 90 percent of the population of India is agricultural (Raman (1963)).

To date there have been many studies of the monsoon, some of which are described in chapter 2. Most of these investigations were restricted to the use of data collected from land stations, with very little being available from the vast ocean areas. New data has recently become available. Vonder Haar (1968) in his study of the earth's radiation budget, accumulated more than 30 months of continuous, satellite measured albedo and radiated long wave data over almost the entire globe.

These data encompass the period from the summer of 1963 to the autumn of 1965. Thus, for the first time, continuous radiation data over land and sea are available which cover the growth and development of two monsoons. Ironically, the monsoon of 1964 was very strong and the monsoon of 1965 was very weak and practically nonexistent.

The main task, then, is to examine these two monsoons over a longer span of time and space than has ever been attempted before. Further, characteristic radiation patterns of the monsoon will be suggested. In the process, there appear indications that the long wave radiation data can be combined with the albedo yielding a quantitative measure of monsoon intensity.

2. Historical Background

Differential heating as the cause of the monsoon was set forth as early as 1686 by Halley in the Memoirs of the Philosophical Society of Great Britain. This theory is still unchallenged.

Simpson (1921) states that the primary cause of the monsoon is the high temperature and corresponding low pressure over the land. Air is then transported under the influence of this pressure system and the rotation of the earth from the southern hemisphere northwest across the equator and then northeast in the northern hemisphere. The moisture accumulated in the long journey over the oceans is then distributed over India due to orographic effects in and around India. Thus, he says, the rainfall associated with the monsoon is determined by topography, and says nothing about other causes.

Wagner (1931) held that the monsoon represents a stationary system of cyclonic disturbances reaching up to the average height of the Himalayas between two air masses, one continental belonging to the west winds of the middle latitudes and the other maritime. He considers that the continental air is warmer than the monsoon air at the surface and colder above and that a considerable part of the monsoon precipitation in and south of the Gangetic plain is due to cyclonic convergence.

The Army Air Force in their study of India, Burma and Southern China (Climate and Weather of Southeastern Asia, 1942) carries this effect further observing that these Eastern cyclones move toward the low over northern India during the monsoon season and then move southward in late September. They conclude that the pulse and extent of the monsoon are related to these depressions.

Yin (1949), in his renowned paper on the 1946 monsoon, discovered that the burst of the monsoon occurs as a mean low latitude trough that is displaced rapidly from one semi-permanent position near 90 E to another relatively semi-permanent position near 80 E. He finds that the motion of this trough is caused mainly by the displacement of the low level westerly jet from south of the Himalayas to their northern boundary. This displacement correlates in time with a general rearrangement of the northern hemispheric long wave pattern that results in a replacement of a mean ridge by a mean trough over central Siberia. A polar trough then extends all the way from Siberia to the tropics.

Chakravortty and Basu (1956) investigated the influences of disturbances from the west on the weather over northeastern India during the monsoon season. They state that the contribution of such disturbances when they pass through the eastern Himalayas is to increase rainfall over the submountain regions of northeast India to a significant and often important degree. They maintain that the passage of such disturbances accentuates the monsoon trough near the foot of the Himalayas. They also state that the monsoon current becomes stronger due to the convergence of the Arabian Sea and Bay of Bengal branches of the monsoon.

Pant (1964) extended the work of Yin (1949) by incorporating the changes in large scale circulation as related to the gradual onset of monsoon rain over different parts of India. He maintains that the monsoon trough forms near 90 E at 700 mb and then shifts westward to 80 - 85 E and becomes more intense. The orientation of the primary axis of the monsoon trough, which was north-south at the beginning of June, becomes east-west by the end of June, the monsoon low having formed with its axis along about 22 N. This is the time, he says, when the monsoon establishes itself over the whole country. At the same time, the Pacific High shifts northward toward Japan. He concludes that the onset of the monsoon thus occurs gradually and calls for new methods to forecast the formation and movement of the monsoon trough. It is worth noting here that the availability of satellite photographs and radiation data now provide a substantial data base for developing such forecast methods.

Colon (1964) studied the Arabian Sea area and interactions between the southwest monsoon current and the sea surface. He states that over large portions of the Arabian Sea there is a rapid warming of the surface

water during late winter and early spring. The maximum temperatures are observed around May, at the time of the establishment of the southwest monsoon circulation. Then there is a cooling trend to a minimum in August and September. The water cooling appears to be a direct result of the establishment of the southwest monsoon regime. Large rates of heat flux by evaporation (670 langleys per day or 1.2 cm per day) were observed in the west central portions of the Arabian Sea. He shows that the evaporation makes a major contribution to the water cooling in that area.

Rao (1966) used long wave radiation (8 - 12 microns) from TIROS IV to study the 1962 monsoon. He observes that the centers of low outgoing long wave radiation associated with the cloudiness of the intertropical convergence zone (ITC) moved northward from April to June, the most abrupt shift occurring in the middle of May. With the advance of cloudiness, the monsoon sets in over the Indian subcontinent. Changes in the radiation values showed changes in the cloud fields. He also noted that when more satellite data become available it will be possible to study the variation in the monsoon circulation, the retreat and the development of the monsoon by observing the changes in the radiation intensities.

The large number of investigations point out that the monsoon is still not completely understood. First generation satellites (the TIROS series) have provided the first good indication of what is happening over the vast ocean areas surrounding the Indian subcontinent. As satellite data increases in quality and quantity, our understanding of the monsoon will likewise increase, thus yielding more effective methods of forecasting the onset, intensity and duration.

3. Data Availability

Radiation data used here are essentially those of Vonder Haar (1968). Most of the data were collected by low resolution sensors whose design was based on principles first described by Suomi (1958). Data for June, 1963 to September, 1963 were collected by hemispheric sensors mounted on TIROS IV. These are described in detail by Sprakman (1964) and House (1965). The data were transformed to radiation budget parameters (long wave radiation, albedo, and net radiation) using the techniques developed by House (1965) and Suomi et al. (1967).

Data for June, 1963 to May, 1964 were collected from medium resolution sensors mounted on TIROS VII. A complete description of this system is given by NASA Staff Members (1964). Season averages of albedo and long wave radiation were computed in a manner similar to that of Bandeen et al. (1965).

Data for June, 1964 to November, 1965 were collected by disc sensors mounted on experimental satellites. The description and data reduction techniques are similar to those for the hemispheric sensors, above.

The data is given in terms of an average value for each 10 × 10 degree latitude-longitude block since the low resolution sensors require this limit on spatial resolution. Long wave radiation is given in langleys per minute and albedo is given in percent (representing 0.3 - 3.0 microns, see Vonder Haar (1968)).

The change of sensors in June, 1964 would lead one to suspect comparisons in any time series. However, there were about three months of overlapping data. These were compared by Vonder Haar and found to correlate almost exactly.

The rainfall data were compiled from the Indian Journal of Meteorology and Geophysics (for example: Staff Members (1964)). The data are given in terms of percent of mean seasonal rainfall for the 30 meteorological divisions of India.

It should be noted that because of the agricultural aspect of the monsoon, rainfall data in percent are used rather than actual millimeters of rainfall. That is, the most important consideration to the economy of India is whether the monsoon rains were above normal or below normal.

4. Procedure of the Investigation

Long wave radiation and albedo at the top of the atmosphere are generally indicative of cloud top heights and cloud amounts, respectively. Fritz and Winston (1962), Wark, Yamamoto, and Lienesch (1962), and Rao and Winston (1963) have shown methods of converting long wave radiation values to cloud top heights. Although there are difficulties when dealing with high thin cirrus or scattered clouds, it is assumed that values of 0.34 langleys per minute or below correspond, generally, to broken or overcast clouds and that regions of lowest outgoing radiation correspond to the thickest clouds or clouds of large vertical depth (Rao (1966)).

High values of albedo are indicative of large cloud amounts. The average albedo of the earth is about 30%. Vonder Haar (1968) calculated a value of 29% ($\pm$ 1). The average cloud cover of the earth is 0.4 to 0.5. Thus about half the earth is clear to scattered and half is broken to overcast. The oceans, which cover most of the earth, under clear conditions have an albedo of about 10% (Conover, 1965) and taking into account some scattered clouds and land, the average albedo for the "clear" half of the earth will be about 15%. This means that the average albedo for

the "cloudy" half is about 45%. To include broken situations, a value of 28% or above is chosen to represent regions with broken to overcast conditions.

The study of Rao (1966) shows how long wave radiation can be used to study the monsoon. Similar studies could be conducted using albedo. Each type of data is adequate for examining the southwest monsoon (and other meteorological phenomena). But using both types in conjunction with one another should provide much more insight.

In this light, an attempt is made to combine three parameters (long wave radiation, albedo, and rainfall) into an index representing the intensity of the monsoon.

It is generally accepted that more precipitation is expected from clouds with large vertical extents than from low clouds and that more precipitation is expected from areas with high cloud amounts than from areas with low cloud amounts. By identifying regions with low long wave radiation (high cloud tops) and high albedo (large cloud amounts) areas of maximum cloud activity can be located.

Figure 1 shows this region qualitatively. That portion with low long wave radiation and high albedo is labeled high, thick, broken or overcast. The region with high long wave and high albedo represent bright, warm targets such as fog or low cloud decks. The region with high long wave radiation and low albedo represent warm, generally nonreflecting targets such as cloudless oceans. The region with low long wave radiation and low albedo represent cold, generally nonreflecting targets or a combination of high, thin cirrus with some radiation emanating from lower layers or the earth's surface coming through.

A point located region I is expected to represent greater activity than a point in any of the other regions.

4.1 Long wave, Albedo and Rainfall Relationships

The Indian southwest monsoons for 1964 and 1965 provide an excellent opportunity to investigate the relationships between radiation data and rainfall because of the striking differences in intensity. In fact, there was enough difference in the two to cause the annual total agricultural production level to suffer a sharp drop in 1965 as shown in Figure 2 (based on data from Food and Agriculture Organization of the United Nations, 1968).

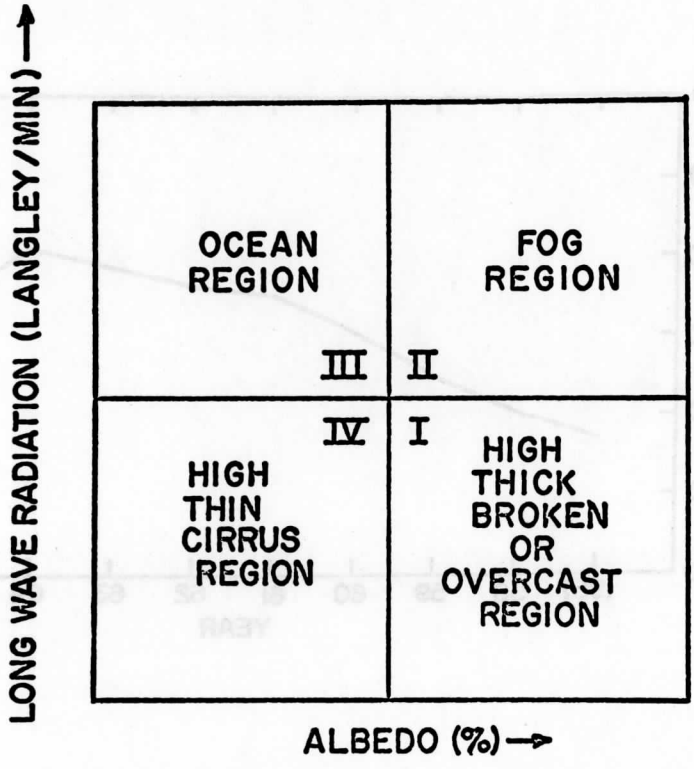

Fig. 1: Qualitative diagram of long wave radiation vs. albedo showing regions explained in the text.

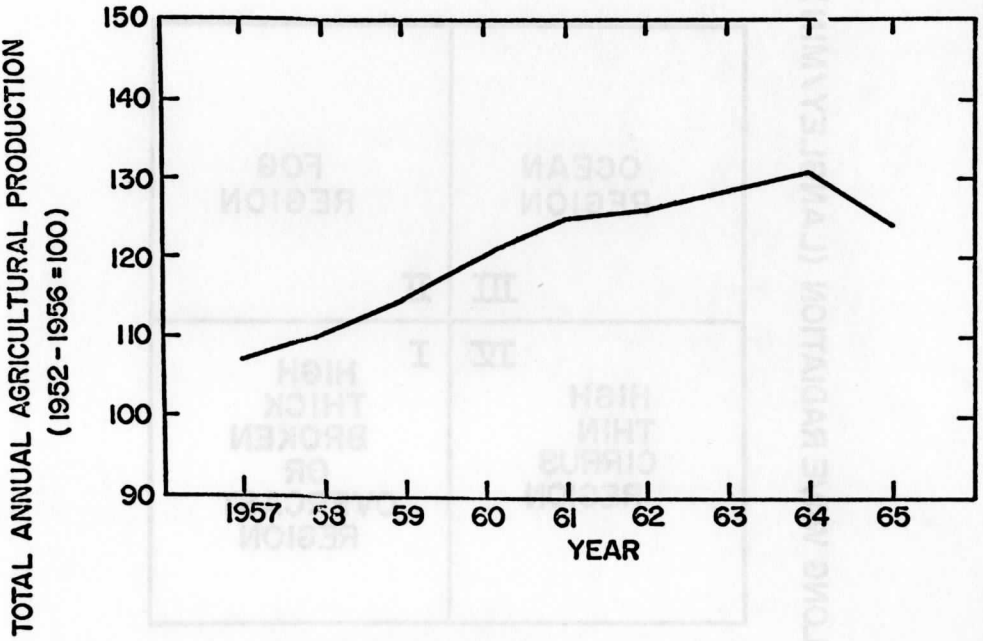

Fig. 2. Total annual agricultural production of India for 1957 through 1965.

An average of precipitation percents for the three 10 x 10 degree blocks, which approximate the Indian subcontinent, were computed taking into account the different areal coverage of each meteorological division. Points corresponding to region I of Figure 1 appear to show the best correlation. A diagram of these vs. the appropriate long wave radiation value (in time and space) is shown in Figure 3. A similar diagram with albedo is shown in Figure 4. These points are quite scattered, as expected, since actual rainfall is not a function of long wave radiation and/or albedo alone but is affected by topography, local convection, etc. There does, however, seem to be some relationship.

The distribution of points in Figures 3 and 4 is different. The distribution for albedo vs. rainfall is wider than that for long wave radiation vs. rainfall; this implies that actual rainfall is more dependent on cloud top height and thickness than on cloud amounts, as expected.

For the purpose of using these results as the first approximation to an intensity index, the distribution is considered to be the same on the two diagrams, and linear. The results of this investigation will show that this first approximation does, in fact, produce meaningful results, thereby calling for further investigations to determine an optimum index.

4.2 Intensity Index Nomogram

With the results of the previous section, a nomogram is constructed in the fashion of Figure 1. The nomogram is constructed by taking points at unit distances for each value of rainfall from the relationships in Figures 3 and 4 and plotting these on a diagram of long wave radiation vs. albedo, as shown in Figure 5. The rainfall value of each point is taken as the index number that is shown in Figure 5.

The nomogram can be interpreted in several ways. For example: Given values for the long wave radiation and albedo for a certain region, the nomogram can be entered and the intensity index read off directly. The index represents a measure of meteorological activity with respect to clouds and an indication of intensity. Higher index values mean higher activity or higher intensity.

Lines of constant intensity index can be interpreted as follows: If the two radiation values are given, and the corresponding index determined, a certain cloud density is defined. Now, if there is another value of long wave radiation which is slightly lower, with the same albedo, more cloud activity is expected since this lower value represents higher cloud tops. In the same way, given an albedo which is slightly larger, with the same long wave radiation, more cloud activity is expected since

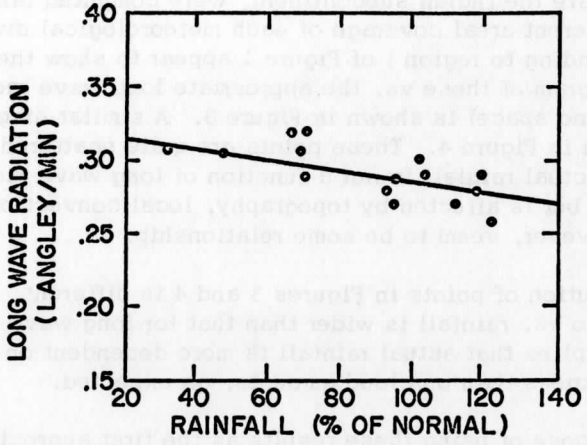

Fig. 3: Long wave radiation vs. rainfall

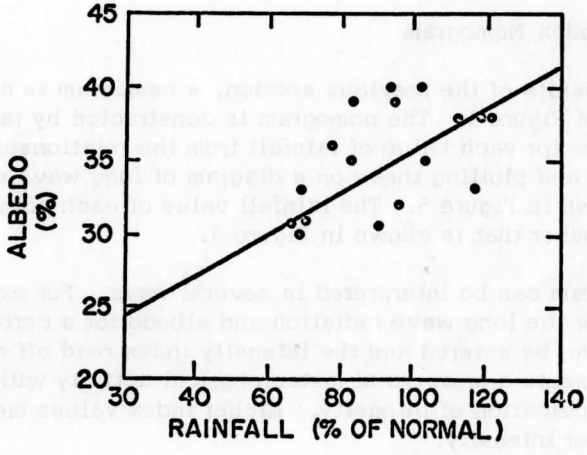

Fig. 4: Albedo vs. rainfall

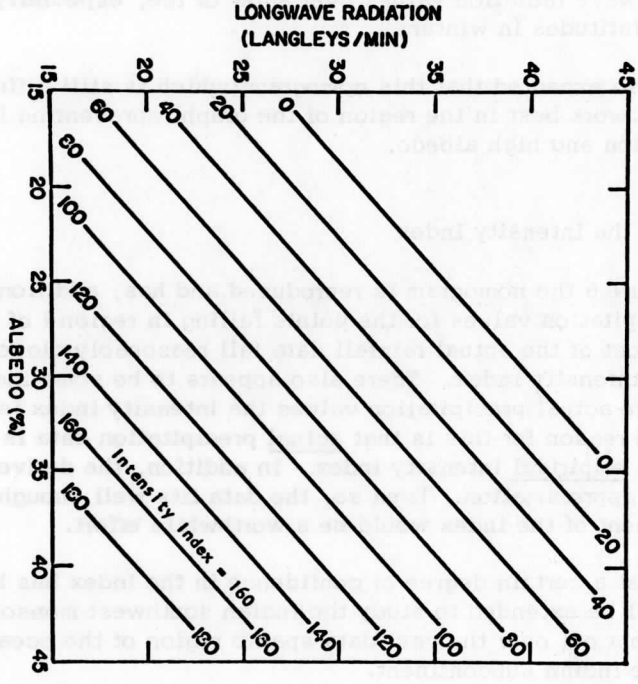

Fig. 5: Intensity index nomogram

this larger value represents a larger cloud amount.

It must be noted that great care is to be used when trying to apply this index over land surfaces. Misleading index values can occur, for example, because of high albedos from clear deserts (such as the Sahara), or low long wave radiation values over snow or ice, especially in high and middle latitudes in winter.

It is also expected that this nomogram (which is still a first approximation) will work best in the region of the graph representing low long wave radiation and high albedo.

4.3 Test of the Intensity Index

On Figure 6 the nomogram is reproduced and has, additionally, the actual precipitation values for the points falling in region I of Figure 1. Note that most of the actual rainfall data fall reasonably close to the corresponding intensity index. There also appears to be some indication that for large actual precipitation values the intensity index is too low. Perhaps one reason for this is that actual precipitation data is being compared to the empirical intensity index. In addition, the derived index is only a first approximation. Even so, the data fits well enough to suggest that refinement of the index would be a worthwhile effort.

Now that a certain degree of confidence in the index has been reached, its use shall be extended to study the Indian southwest monsoon not only over land, but out over the vast data sparse region of the oceans surrounding the Indian subcontinent.

5. The Indian Monsoon Using the Intensity Index

In this chapter the Indian monsoon is studied using long wave radiation, albedo and the intensity index. It is shown that either long wave radiation or albedo can be used to study the monsoon but can also produce misleading results. It is also shown that the intensity index combines the best features of both types of data producing meaningful, quantitative results.

Seasonal maps of long wave radiation, albedo and the intensity index are presented in Figures 7, 8 and 9. The season depicted encompasses June, July and August (JJA) and defines the monsoon season as used in this paper.

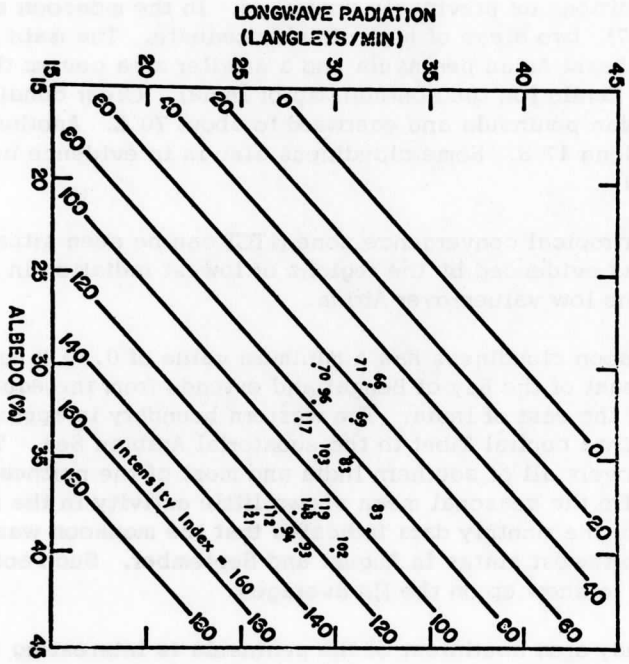

Fig. 6: Nomogram with actual rainfall

Figure 7 depicts the monsoon seasons of 1963, 1964 and 1965 in terms of long wave radiation. Shaded areas denote regions with values of 0.34 langleys per minute or less, and generally represent broken to overcast conditions as previously described. In the monsoon season of 1963 (Figure 7), two areas of high clouds dominate. The main area is over the southeast Asian peninsula and a smaller area covers the ocean southwest of Kerala (on the southern tip of India). Clear conditions exist over the Arabian peninsula and eastward to about 70 E. Another clear area is oriented along 17 S. Some cloudiness also is in evidence over Africa at about 10 N.

The Intertropical convergence zone (ITC) can be seen situated along 10 to 15 N, as evidenced by the regions of lowest radiation in the monsoon pattern and the low values over Africa.

The monsoon cloudiness has a minimum value of 0.30 langleys per minute northeast of the Bay of Bengal and extends from the equator to at least 40 N to the east of India. The western boundary is approximately along a line from central Tibet to the equatorial Arabian Sea. The seasonal cloudiness covers all of southern India and most of the northeast portion. Note that while the seasonal mean shows little activity in the northwest, an analysis of the monthly data indicates that the monsoon was most active in the northwest states in August and September. Such activity is not expected to show up on the JJA averages.

The cloudy area southwest of the peninsula is interesting since it approximates the location of high net sea-air heat flux mentioned by Colon (1964).

The intense monsoon season of 1964, as shown in Figure 7, depicts extensive cloudiness covering the entire portion of the map north of the equator. The African radiation minimum is farhter north than in 1963 and is centered over Aden. Cloudiness covers the Arabian peninsula which was clear the previous year. South of the equator, the clear area is more evident but is still in the same location.

In addition to covering a larger area, the monsoon cloudiness is more intense. In fact, the minimum radiation is only 0.25 langleys per minute compared to 0.30 in 1963. The radiation values over India are lower by about 0.07 langleys per minute.

The ITC is slightly north of its 1963 position over Africa and slightly south in the Bay of Bengal.

There is very little evidence of a cloudy region southwest of the peninsula on this map.

In 1965 the monsoon was very weak, especially in the northern states. But Figure 7 shows the region of cloudiness to be larger than in 1963. This apparent paradox will be considered later when the albedo is taken into account in determining intensity indices.

In 1965, then, the cloudiness appears to cover almost all of India, southeast Asia, the Arabian sea and the Bay of Bengal. The double minimum is still present although the main minimum is shifted farther west by about 10 degrees. The southern hemisphere clear area is in the same position but is extremely zonal compared to the previous two years.

The two radiation minimums have the same values as in 1963 although the pattern appears to be more widely separated. Note that the ITC is located south of its 1963 position over Africa by about 10 degrees.

Again, there is little evidence of a cloudy region southwest of the peninsula.

Considering the three seasons depicted in Figure 7, the general features of the monsoon (such as the center over the Bay of Bengal) appear each year. Using these three maps alone, one can observe that the 1964 monsoon was indeed the strongest. However, it is not clearly evident that the 1965 monsoon was the weakest! Before proceeding on this point, the albedo maps merit examination.

Figure 8 portrays these three monsoon seasons in terms of albedo. Shaded areas signify regions with values of 28% or more, and generally represent areas with broken or overcast conditions as previously described.

The monsoon cloudiness of the 1963 season (Figure 8) extends from Kerala eastward over the Bay of Bengal and southeast Asia and northward to at least 40 N. The highest albedo value of the monsoon is 37%. High albedo values also exist over the Arabian peninsula and north Africa. Note that the Arabian and Sahara deserts alone have albedo values near 30% (Conover, 1965). This fact, combined with the high long wave radiation values in Figure 7, indicate an area that is almost completely clear. The large values near 10 N over Africa, however, are due to cloudiness since this area is not a desert region.

Some evidence exists supporting the existence of the cloudy region southwest of the peninsula. The clear area south of the equator is well defined by low albedo values.

The strong monsoon of 1964, in Figure 8, again shows cloudiness covering the entire northeast quadrant of the map, and almost all of the eastern half. The highest albedo is now 43% compared to 37% in 1963

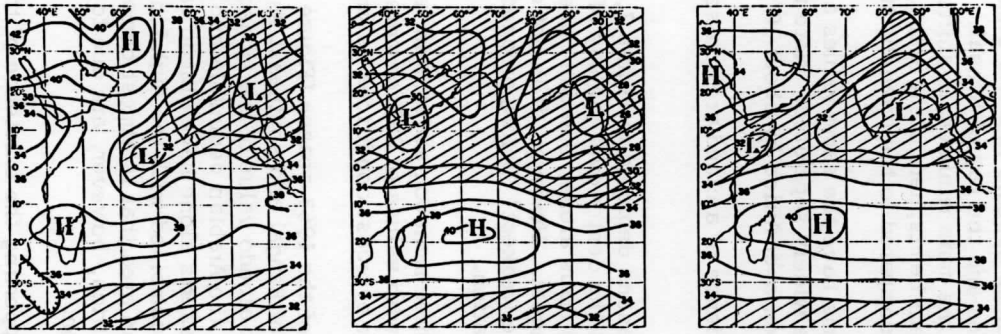

Fig. 7: Long wave radiation maps for 1963, 1964, 1965 monsoons

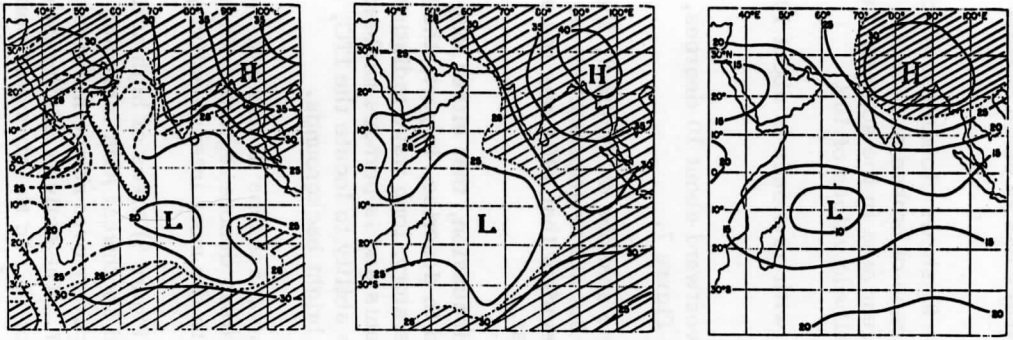

JJA 63 JJA 64 JJA 65

Fig. 8: Albedo maps for 1963, 1964, 1965 monsoons

and is in the same position. The cloudiness over the Somali Republic appears as a small region of high albedo values. Southwest of the peninsula, there does appear some evidence of a cloud region which was not apparent on the long wave radiation map (Figure 7).

The clear area in the southern hemisphere is again broader than in 1963.

The 1965 monsoon season (Figure 8) shows cloudiness north and east of central India. There is little evidence of broken or overcast skies on any other portion of this map. The clear area in the southern hemisphere is very pronounced, as is shown by albedo values of 10%.

Recall that the albedo of oceans with no clouds is about 10% (Conover, 1965).

The albedo maximum is shifted westward about 10 degrees, which corresponds to the westward shift on Figure 7.

Once again, considering the three seasons on Figure 8, the general features do appear on all three maps but not as impressively as before. Using these three maps alone, it is evident that 1964 was the strong monsoon year and 1965 was the weak year.

It is clear, from the preceding discussion, that either long wave radiation or albedo alone can be used to describe, in part, the Indian monsoon. But neither tells the whole story; long wave radiation is lacking in its ability to determine cloud amounts and is perhaps misleading by itself. Albedo maps are lacking in the ability to locate the ITC, for example, and is misleading in areas with bright backgrounds.

Figure 9 presents the three monsoon seasons in terms of the intensity index derived in chapter 3. Shaded areas denote regions with index values of 40 or more and represent zones with the most intense activity.

In the monsoon season of 1963 (Figure 9) areas of high activity cover southern India, the Bay of Bengal and southwest Asia including northeast India and Tibet. The zone of high activity over northern Africa shows up very well, with index values up to 47. The activity southwest of the peninsula is only moderate with an index of 28. In the strongest portion of the monsoon, centered over eastern Burma and western Laos, activity is very intense with a maximum index of 100. Here one sees a true picture of monsoon activity depicted in terms of a quantitative measure of identity.

The strong monsoon of 1964 portrays itself vividly on Figure 9. The most intense portion of the monsoon covers more than the northeast

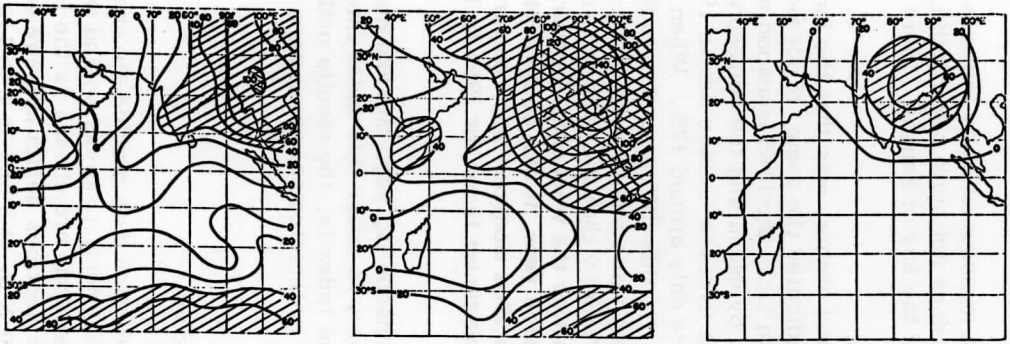

Fig. 9: Intensity index maps for 1963, 1964, 1965 monsoons

quadrant of the map and has index values up to 155 over Burma. High values exist throughout India, the Bay of Bengal and southeast Asia. The extension southwest of the peninsula is quite pronounced and active with index values up to 50. Note that the southern hemisphere clear area has index values of zero and larger in extent than that in 1963.

In 1965 (Figure 9) the maximum monsoon activity index is less than 70, and very restricted in size. It does not quite cover India, Tibet and Burma, and covers only a portion of the Bay of Bengal. There is no other activity on this map.

The apparent paradox, mentioned earlier, was that the long wave radiation map for 1965 (Figure 7) indicated the same, if not more,cloudiness than the map for 1963 when, in fact, the 1965 monsoon was much weaker. The reason comes to light by examining the corresponding albedo maps (Figure 8). The albedo values over the Arabian Sea in 1963 were around 24% while those in 1965 were only around 17%. When these are combined into index values (Figure 9), this difference is readily apparent. Thus another limitation on using long wave radiation by itself has been found. It is clearly obvious from Figure 9 that the 1964 monsoon was the most intense and the 1965 monsoon was the weakest. Further, by observing the maximum index values for each year, it can be determined quantitatively how much more intense the 1964 monsoon was compared to, for example, the 1963 monsoon. The maximum index for 1963 is 100, for 1964, 155, and for 1965, 70.

Before one can say that one monsoon is, say, one and one-half times as intense as another, it is necessary to refine this index into its most optimum form. Crude as the present index is, the results outline a method by which the intensities of various meteorological phenomena can be investigated.

5.1 The Time History of Two Monsoons

Thirty months of continuous radiation data provide an excellent opportunity to examine monsoon development, progression and withdrawal. Time-latitude and time-longitude sections are chosen as the best method of investigation. The time-latitude sections depict average values for each 10 degree latitude belt from 40 N to 40 S and 30 E to 110 E. Similarly, the time-longitude sections portray average values for each 10 degree longitude belt from 30 E to 110 E and from 40 N to 20 S.

Advection of cloudiness or intensity northward or southward can be detected on the time-latitude sections, and eastward or westward motion, on the time-longitude sections.

Figures 10 and 11 show long wave radiation in terms of time-latitude and time-longitude sections, respectively. Shaded areas correspond to those used on previous diagrams.

In Figure 10 during June, July and August of 1963 (JJA 63), the most active portion of the monsoon appears between the equator and 20 N. A nearly clear area moves southward from about 40 N over a period of three seasons and stabilizes near 15 N in winter followed by a slight northerly movement in spring (MAM 64). This is the period of maximum surface heating preceding the onset. The 1964 monsoon season starts abruptly in June as shown by the strong gradient between spring and summer. Note that the monsoon trough described by Yin (1949) and Pant (1964) does not appear on these diagrams. The motion of this trough occurs in a very short period of time (from the end of May to the first part of June), and compared to the time scale used here, is not expected to appear.

Cloudiness remains from 10 S to at least 40 N for almost three seasons, becoming concentrated on the equator in DJF 64/65. It then moves northward throughout MAM 65 to its most northerly extent (about 20 N) becoming the 1965 monsoon. In fact, northern India (north of 20 N) was extremely dry during the monsoon. Cloudiness disappears completely in SON 65.

Important differences in the two monsoons are now brought to light. In particular, the period of large surface heating so evident in MAM 64 was virtually nonexistent in MAM 65. The abrupt onset characterizing the 1964 monsoon occurs very gradually in 1965. Also, while the 1964 monsoon shows little influence due to cloudiness coming from the north or south, the 1965 monsoon appears to have been caused entirely by cloudiness moving northward from the equator.

The southern clear region is also interesting, moving from 10 S in the summer of 1963 to 20 S for the next three seasons and moving farther south following the 1964 monsoon. Its movement in the two years is completely different.

Figure 11 is now examined for eastward and westward movements. Very little cross-longitude motion occurs in the year preceding the 1964 monsoon. The clear zone, which moved north to south during this period, remained confined to the western region (30 E to 60 E). The abrupt monsoon onset in 1964 is also apparent on this diagram, but indicated rapid motion from the east. Cloudiness remains across almost the entire longitude range for the next three seasons. The most cloudy portion appears to move westward to about 70 E until MAM 65 when it moves eastward culminating in the 1965 monsoon.

Considering Figures 10 and 11 together, it is seen that the 1963 monsoon dissipates almost completely leaving the following three seasons relatively cloud free (on a seasonal basis). During this period, surface heating takes place reaching a maximum in MAM 64, and perhaps is the main cause of the 1964 monsoon. Cloudiness from the 1964 monsoon, however, does not dissipate significantly with high clouds moving southwest to about 0 N and 75 E by the end of autumn and remaining there until MAM 65. At this point it moves northwest into the southern portion of India becoming the 1965 monsoon.

In other words, monsoon cloudiness in 1964 appears abruptly following the clear spring season. This cloudiness split into two segments, one moving northeastward, the other moving southwestward into the south Arabian Sea. More importantly, the Arabian Sea segment appears to have maintained its intensity until the 1965 monsoon season when it gradually moved into southern India. This is apparently the major source of cloudiness for the 1965 monsoon.

Figures 12 and 13 show albedo in terms of time-latitude and time-longitude sections, respectively. Shaded areas correspond to those used on previous diagrams.

In Figure 12 the apparent regions of cloud cover north of 20 N are, to a large extent, due to desert regions and must be interpreted with great care. Again, the cloudless spring of 1964 is prominent as is the abrupt increase in cloud cover associated with the onset of the 1964 monsoon. The movement of high cloud cover to the south is also apparent. A slight increase in cloud amounts appears during the 1965 monsoon.

In Figure 13 the MAM 64 heating is apparent. The most prominent feature is associated with the post-monsoon cloud cover. It originates during the monsoon and progresses steadily westward until DJF 64/65. At this point the diagram shows a decrease in cloud cover, and that which remains moves eastward until the 1965 monsoon.

Considered together, Figures 12 and 13 show the area of large cloud amounts dissipating after the 1963 monsoon, and the clear heating season preceding the 1964 monsoon. Again, the region of large cloud amounts following the 1964 monsoon appears. It moves southwestward until DJF 64/65. Note that cloud cover then decreases as it moves northeastward culminating in the 1965 monsoon.

Figures 14 and 15 show the intensity index on time-latitude and time-longitude sections, respectively. Shaded areas are the same as those on previous diagrams.

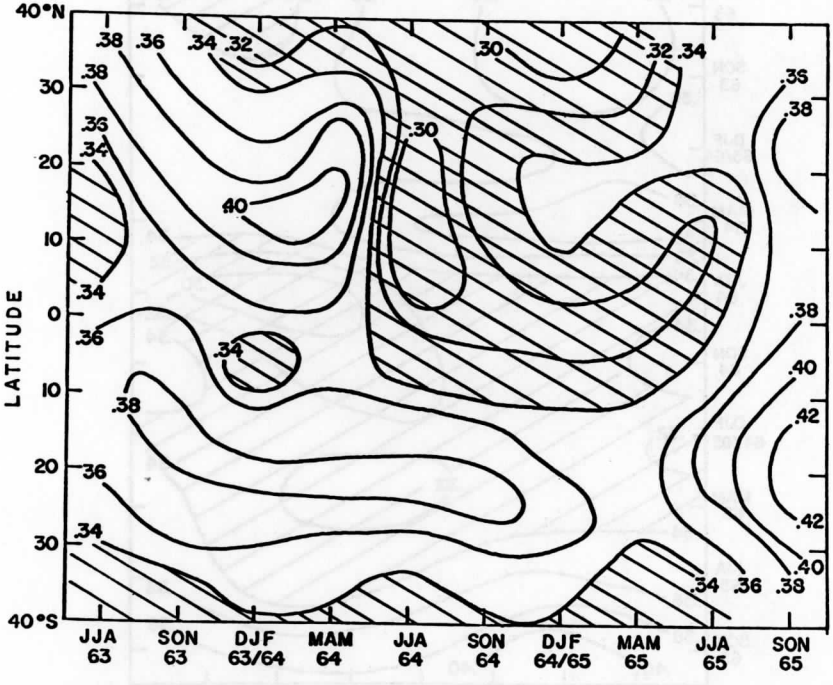

Fig. 10: Long wave radiation time-latitude section

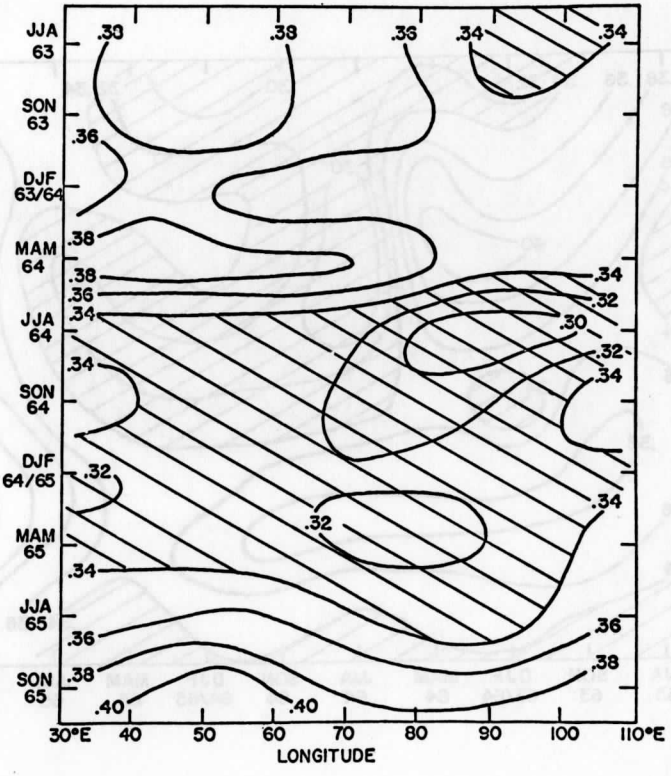

Fig. 11: Long wave radiation time-longitude section

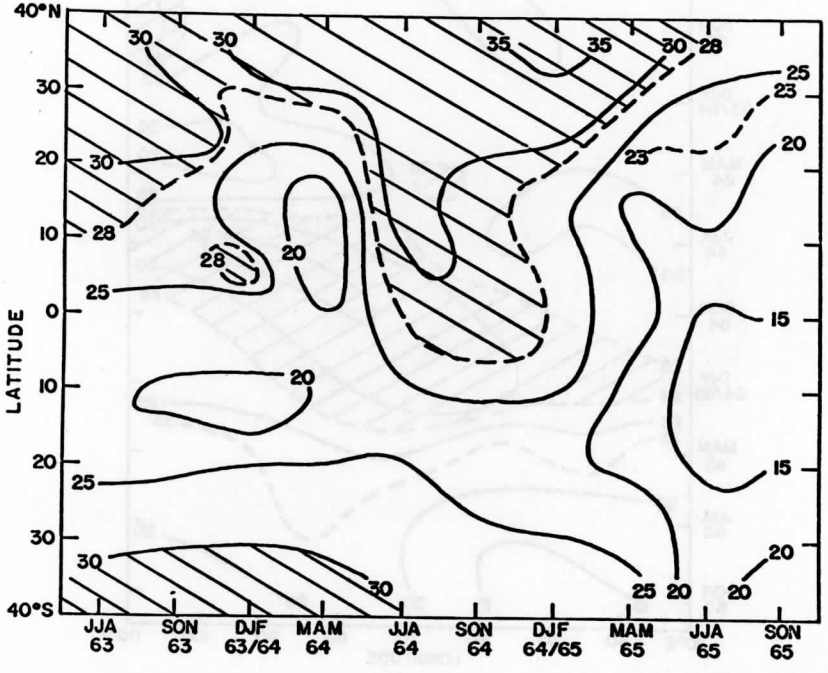

Fig. 12: Albedo time-latitude section

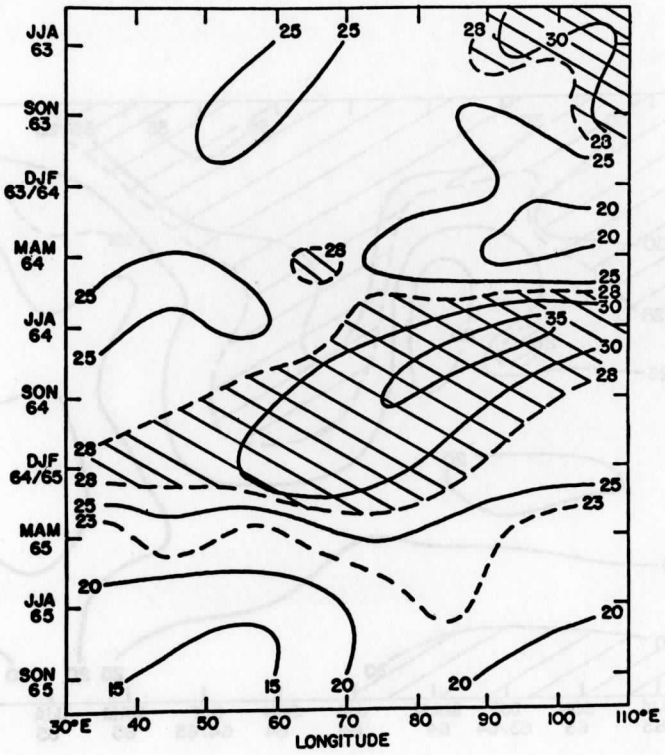

Fig. 13: Albedo time-longitude section

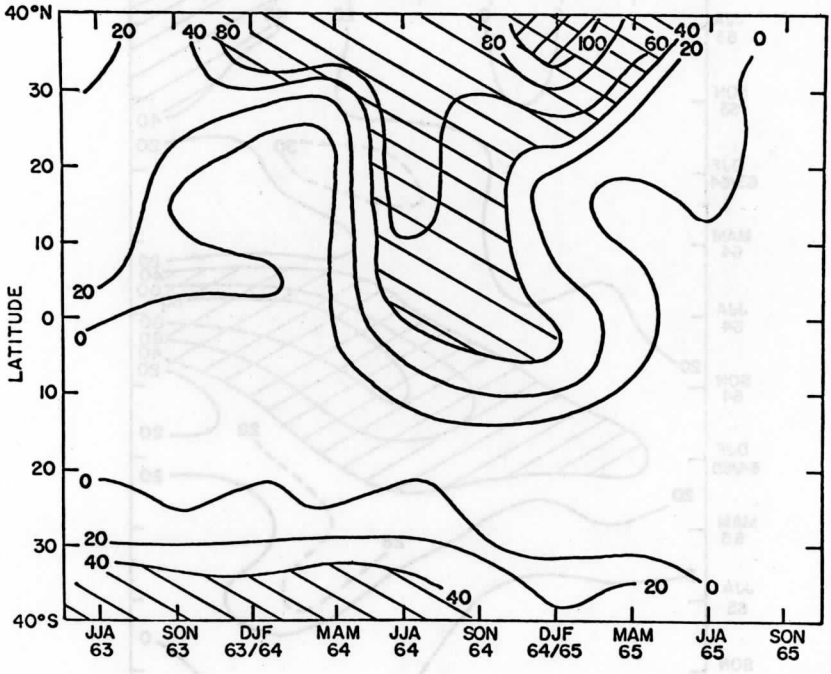

Fig. 14: Intensity index time-latitude section

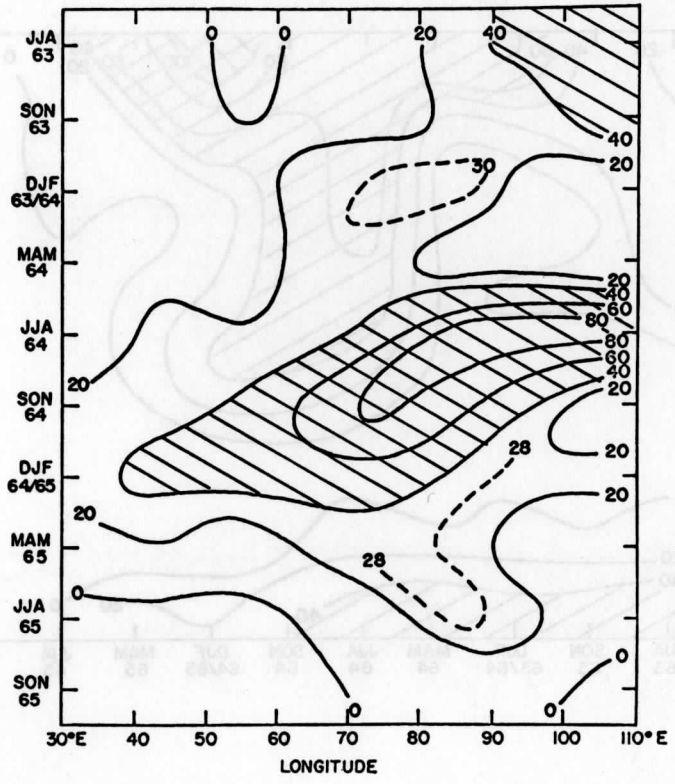

Fig. 15: Intensity index time-longitude section

In Figure 14 the region of greatest activity is associated with the monsoon of 1964. The southward movement throughout SON 64 into DJF 64/65 is readily apparent. Note the indication of some southwesterly motion following the 1963 monsoon. This feature is suggested on long wave radiation and albedo sections also (Figures 10 and 12), but its relative magnitude compared to that of the 1964 monsoon can be determined best by using the index. The 1965 monsoon appears on Figure 14 as a slight southward projection of an index isopleth.

It is noted that these values represent averages over a latitude range (30 E to 110 E) that extends well beyond the normal western extent of the monsoon. In this light, values for 60 E to 110 E were computed and are presented in Table 1. Index values from Table 1 for the Indian subcontinent (10 N to 40 N) are about 43 for the 1963 monsoon, 95 for 1964 and only 28 for 1965. These values can be interpreted as an indication of the relationship between monsoon intensity and agricultural production.

In Figure 15 there are indications of active regions moving westward following the 1963 monsoon, but not nearly as pronounced as that following the 1964 monsoon. This intense region moves steadily westward with time and has nearly the same latitude spread for SON 64 and DJF 64/65. Note the decrease in intensity after DJF 64/65 and the eastward motion into the 1965 monsoon.

Figures 14 and 15 together show that the active area following the 1963 monsoon moved southwestward in SON 63 decreasing in intensity, and then moved westward in DJF 63/64. But the intense region following the 1964 monsoon moved southwestward throughout SON 64 and DJF 64/65 and maintained its intensity. That is, the active area of 1964 was more intense, moved farther southwest and preserved its intensity longer than in the previous year.

There is a priori verification of extensive cloudiness throughout the tropic regions in 1965.[1]

It is also instructive to consider representative values of long wave radiation, albedo and the intensity index for the seasons preceding the two monsoons. Figure 16 portrays these seasons pictorially. The thickness and width of clouds on Figure 16 symbolically correspond to the typical values of long wave radiation and albedo shown. Values are representative of the area of the Indian subcontinent from the Himalayas to the equator. It is assumed that land areas have albedo values of about

---

[1] Personal communication from Mr. Lewis Allison, NASA, based on Environmental Technical Applications Center (ETAC) cloudiness summaries.

TABLE 1

Longitudinal Averages (60° E to 110° E)

Long Wave Radiation (langleys/minute) $\times 10^{-2}$

	JJA 63	JJA 64	JJA 65
40° N	35.6	30.4	35.2
30° N	34.8	28.6	33.0
20° N	32.4	27.6	30.6
10° N			

Albedo (Percent)

	JJA 63	JJA 64	JJA 65
40° N	32.6	36.2	28.6
30° N	33.0	36.4	29.4
20° N	29.0	34.2	23.8
10° N			

Intensity Index

	JJA 63	JJA 64	JJA 65
40° N	40	92	24
30° N	46	99	28
20° N	42	94	22
10° N			

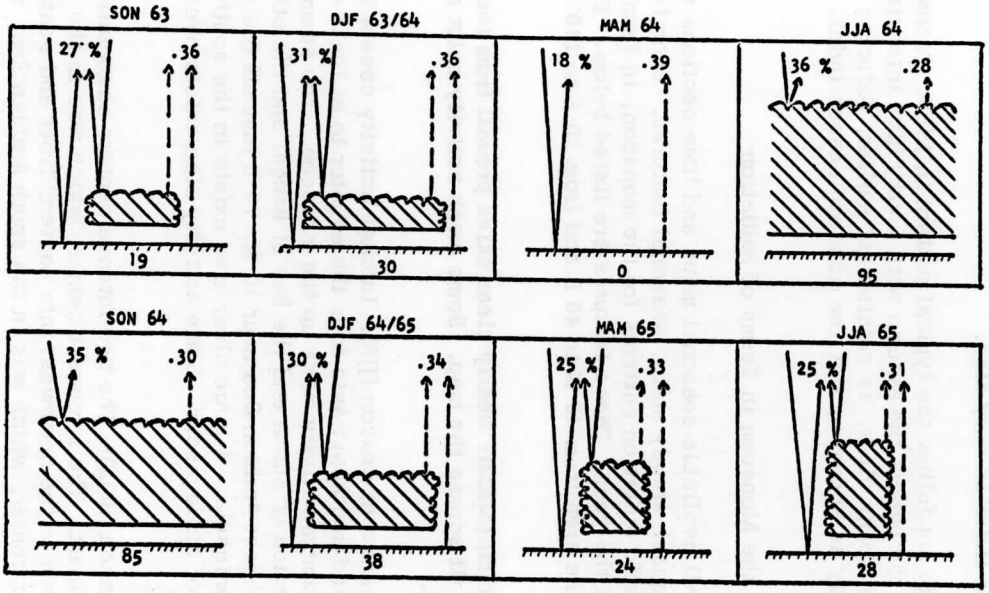

Fig. 16: Typical value diagram of long wave radiation, albedo and intensity index for eight sessions

20% and long wave radiation values of about 0.40 langleys per minute.

The intensity indices for 1964 follow the expected pattern. During the autumn (SON 63) it is quite low representing monsoon dissipation, in winter it increases slightly with the winter monsoon, in spring it is very low allowing maximum surface heating preceding the monsoon, and in the monsoon season the index is very high.

Index values do not follow the typical pattern in 1965. Monsoon activity lingers on throughout the autumn with a very high intensity index. The spring is by no means clear, as pointed out earlier, reducing surface heating significantly as shown by the low monsoon season index.

5.2 Description of the Monsoon in Terms of Radiation

Inspection of all available seasonal maps and time sections reveals certain recurring, quasi-steady state, seasonal features. Such features suggest characteristic radiation patterns for the monsoon, in terms of seasons throughout the year. These features are listed below. Discussion is limited to the area from 40 N to 40 S and from 30 E to 110 E (see Figure 7).

The spring season (MAM): Nearly clear skies prevail from the Himalayas to 30 S all across the map. Some weak activity exist around the equator at 70 E.

The summer (monsoon) season (JJA): Intense activity covers India, the Bay of Bengal and southeast Asia from the equator to at least 40 N. Two centers of maximum activity make up the monsoon. The strongest is located in the region of Burma and the Bay of Bengal and the other is located in the southeast Arabian Sea near 10 N, 70 E just off the southern tip of the Indian peninsula. A large clear area exists in the southern Indian Ocean east of Madagascar. Some activity also exists over northeast Africa at 10 N.

The autumn season (SON): The two intense centers associated with the monsoon split apart. The strongest center, which was in the Bay of Bengal region, moves to the northwest into eastern Tibet and southern China. The weaker center, which was in the south Arabian Sea, moves to the southwest to a relatively stable position near the equator and 70 E. The Arabian Sea, Iran, Saudi Arabia and northeast Africa are nearly cloud free. A clear area also exists south of the equator to 30 S.

The winter season (DJF): The active region near the equator at 70 E remains in approximately the same position but becomes slightly more

intense. North of 25 N cloud activity covers the entire map. These are the features usually associated with the winter monsoon.

The preliminary model discussed here is based on seasonal maps of satellite sensed radiation. It is but a suggestion of what could be done with monthly, weekly or even daily data.

6. Summary and Suggestions for Further Research

Thirty months of continuous low resolution satellite data, emitted long wave radiation and albedo, were used to study the Indian monsoon. These data, combined with rainfall data for the Indian subcontinent, were employed to develop an intensity index which provides the first quantitative measure of monsoon intensity. It was assumed that the index is also representative of precipitation over the oceans where rainfall data is very sparse. Thus a useful tool was developed to study the monsoon over land and the vast ocean areas surrounding the Indian subcontinent.

Three monsoons were studied using the intensity indices and radiation data: the 1963 monsoon, the strong monsoon of 1964 and the very weak monsoon of 1965. Intensity differences in the 1963 and 1965 monsoons were not readily apparent on the long wave radiation diagram. Some difference is observed on the albedo maps. But only on the intensity index diagrams does this difference appear so dramatically. More importantly, the past history of the 1964 and 1965 monsoons were examined. The pre-monsoon seasons proved to be the most interesting. The primary cause influencing the high intensity of the 1964 monsoon appears to be the intense surface heating during the preceding cloudless spring. It was noted that activity associated with the 1964 monsoon lingered on for several months in the south Arabian Sea contributing to cloudy skies in the spring of 1965. Because of the marked cloudiness in this latter season, surface heating was reduced significantly. Thus the cloudiness gradually moving in from the south Arabian Sea became only slightly more intense upon reaching the peninsula. This factor, combined with the apparent evidence that no other cloudy regions moved into India yielded a weak, almost nonexistent 1965 monsoon causing a significant drop in the annual agricultural production.

Typical values of the intensity index, long wave radiation and albedo were compiled for each season of the year preceding each monsoon. From this data, one finds that the intensity index for the autumn of 1964 was only slightly lower than that in the monsoon season.

A model of the monsoon in terms of radiation data was suggested. The most important observation was that the monsoon is composed of two main

activity centers: one over Burma and the Bay of Bengal and one in the southern Arabian Sea just off the southern tip of the Indian peninsula. Following the monsoon season, the Bay of Bengal center moves north and east into eastern Tibet and southern China while the south Arabian Sea center moves southwest to a relatively permanent position near the equator and 70 E.

As the result of this study, new and expanded research areas are suggested. In particular, the intensity index stands only as a first approximation and calls for studies leading to a refined, optimum form. Such an index could be used to study phenomena other than the monsoon. A study using actual precipitation rates rather than percent of normal would be particularly valuable over the oceans. The precipitation term in energy budget studies is difficult to determine over the seas of the world and a refined index could provide the first quantitative values for this term.

Finally, the monsoon itself is still not completely understood. Further studies should be undertaken using higher resolution (spatial and spectral) radiation data and monthly, weekly or even daily radiation values. Such investigations would lend themselves to refining the model of the monsoon, and provide further insight into more effective methods of predicting the onset, intensity, duration and withdrawal of the Indian monsoon.

7. References

Bandeen, W. R., M. Havel, and I. Strange, 1965: A Radiation Climatology in the Visible and Infrared from the TIROS Meteorological Satellites, NASA TN D-2534.

Climate and Weather of Southeastern Asia, 1942: Part 1, India, Burma, and Southern China, Vol. 5, No. 3, United States Government Printing Office, Washington.

Colon, J. A., 1964: On Interactions Between the Southwest Monsoon Current and the Sea Surface over the Arabian Sea, Indian J. Met. and Geoph., Vol. 15, No. 2, 183-200.

Conover, J. H., 1965: Cloud and Terrestrial Albedo Determinations from TIROS Satellite Pictures, J. Applied Met., Vol. 4, No. 3, 378-386.

Chakravortty, D. C., and S. C. Basu, 1957: The Influence of Western Disturbances on the Weather over Northeast India in Monsoon Months, Indian J. Met. and Geoph., Vol. 8, No. 2, 261-272.

Food and Agriculture Organization of the United Nations, 1968: The State of Food and Agriculture 1968, Rome, 147-155.

Fritz, S. and J. S. Winston, 1962: Synoptic Use of Radiation Measurements from Satellite TIROS II, Mon. Wea. Rev., Vol. 90, No. 1, 1-9.

House, F. B., 1965: The Radiation Balance of the Earth from a Satellite. Ph. D. thesis, Department of Meteorology, University of Wisconsin.

NASA Staff Members, 1964: TIROS VII Radiation Data Catalogue and Users' Manual, National Aeronautics and Space Administration, Washington.

Pant, P. R., 1964: Onset of Monsoon over India, Indian J. Met. and Geoph., Vol. 15, No. 3, 375-380.

Raman, C. R. V., 1964: Monsoon Definitions, Indian J. Met. and Geoph., Vol. 15, No. 2, 235-238.

Rao, P. K., 1966: A Study of the Onset of the Monsoon over India During 1962 Using TIROS IV Radiation Data, Indian J. Met. and Geoph., Vol. 17, No. 3, 347-356.

Rao, P. K., and J. S. Winston, 1963: An Investigation of Some Synoptic Capabilities of Atmospheric "Window" Measurements from Satellite TIROS II, J. Applied Met., Vol. 2, No. 1, 12-13.

Shamshad, K. M., 1967: Note on a Technique of Long Range Forecasting for Monsoon Rain in West Pakistan, J. Applied Met., Vol. 6, No. 1, 199-202.

Simpson, G. C., 1921: The Southwest Monsoon, Quart. J. Roy. Met. Soc., Vol. 47, 151.

Sparkman, B. B., 1964: Experimental Analysis of the TIROS Hemispheric Sensor, M.S. thesis, Department of Meteorology, University of Wisconsin.

Staff Members, 1964: Weather, Monsoon Season (June - September 1963), Indian J. Met. and Geoph., Vol. 15, No. 1, 101-108.

Staff Members, 1965: Weather, Monsoon Season (June - September 1964), Indian J. Met. and Geoph., Vol. 16, No. 1, 141-148.

Staff Members, 1966: Weather, Monsoon Season (June - September 1965), Indian J. Met. and Geoph., Vol. 17, No. 1, 115-120.

Suomi, V. E., 1958: The Radiation Balance of the Earth from a Satellite, Annals of the IGY, Vol. 1, 331-340.

Suomi, V. E., K. J. Hanson and T. H. Vonder Haar, 1967: The Theoretical Basis for Low-Resolution Radiometer Measurements from a Satellite, Annual Report, Grant WBG-27, Department of Meteorology, University of Wisconsin, 79-100.

Vonder Haar, T. H., 1968: Variations of the Earth's Radiation Budget, Ph. D. thesis, Department of Meteorology, University of Wisconsin.

Wagner, A., 1931: Zur Aerologic des Indischen Monsuns, Ger. Beitr. z. Geoph., Bd. 30, 196.

Wark, D. Q., G. Yamamoto and J. H. Lienesch, 1962: Methods of Estimating Infrared Flux and Surface Temperature from Meteorological Satellites, J. Atm. Sc., Vol. 19, No. 5, 369-384.

Yin, M. T., 1949: A Synoptic-Aerologic Study of the Cnset of the Summer Monsoon over India and Burma, J. Met., Vol. 6, No. 6, 393-400.

KINETIC ENERGY CHANGES IN A DEVELOPING CYCLONE

by

Frank Sechrist
Richard A. Rudy

ABSTRACT:

An analysis of a major cyclone occurring over the United States in late April, 1968, was accomplished. An attempt was made to measure both the contributions of kinetic energy advection and the changes of total kinetic energy within a fixed volume containing the storm.

Results of the study showed that even though net kinetic energy dissipation initially occurred, the storm developed primarily because of the large contributions of kinetic energy advection; energy conversion was taking place but could not compensate for the larger dissipation process. Later, as positive advection decreased and became negative, overall storm growth was attributed to energy conversion overcoming energy dissipation. The conversion process first appeared in the low levels early in the storm's development before appearing later in the higher levels.

I. Introduction

A recent film developed from the ATS-III meteorological satellite photographs plainly demonstrated the existence of complex atmospheric interactions occurring with major cyclonic development over the central United States during April 22, 23 and 24, 1968. The film, along with corresponding individual photographs, shows an interaction with the cyclone of both an extratropical jet northwest of the cyclone and a subtropical jet to the southwest. The influence of the subsiding extratropical jet in producing clearing behind the cold front has been discussed by Reed (1955) and Danielsen (1964). The precise effect of a subtropical jet on a developing cyclone remains obscure. In any case, the presence of these two important features strongly suggest energy fluxes from sources external to the storm. The problem is to determine quantitatively the extent

to which these energy sources are important in supplying kinetic energy to a growing cyclone.

One of the more puzzling problems confronting theoretical meteorologists today concerns the sources, methods of supply, and influences of kinetic energy on developing cyclones. Sixty-nine years into this century of significant advancement in meteorology, varied and conflicting theories concerning the total energy balance in synoptic scale cyclones are still found. Of principal interest in the present study is the question of precisely how kinetic energy is both supplied to and changes within the developing storm mentioned above.

One of the two essential theories dealing with kinetic energy sources in developing cyclones is that of barotropic instability. This theory proposes, in general, that energy for growing cyclonic disturbances is derived from preexisting kinetic energy of the mean flow. The theory of barotropic instability was derived by Kuo (1949) and Fjortoft (1950), and discussed later by Petterssen (1956) and Eliasen (1960); it is based on the premise that the basic zonal current contains only horizontal wind shear. A necessary condition for instability is that the horizontal shear must have a maximum value at some location. For example, the area of maximum absolute vorticity could be present on the poleward side of a strong west wind belt. Growth of an existing wave is then interwoven with a redistribution of the preexisting vorticity of the wind belt such that the vorticity associated with the perturbation is increased.

Another theory having implications regarding the energy sources of growing cyclones involves the concept of baroclinic instability. In this concept, the differential heating of the atmosphere is seen to produce baroclinicity and increased available potential energy. Cyclone development then occurs as a result of the conversion of available potential energy to kinetic energy. The process is discussed by Charney (1947), Eady (1949), and Kuo (1952).

Obviously, neither the theory of barotropic instability nor that of baroclinic instability can be complete in themselves. The former ignores vertical wind shear and the latter ignores horizontal wind shear; the real atmosphere is characterized by large amounts of both.

Eliasen (1960) employed a model wherein both horizontal wind shear and a horizontal density contrast (vertical wind shear) existed. Both of these features are concentrated in the vicinity of a front. For a particular case, Eliasen found that two-thirds of the wave energy comes from the potential energy while one-third comes from the kinetic energy of the mean flow; this result demonstrates the importance of both barotropic and baroclinic instability.

In the present study, an effort is made to determine the extent to which preexisting energy is supplied to a developing storm through advective processes. To accomplish this, a kinetic energy budget study was made for a volume of the atmosphere in which it was assumed that the developing storm of April 22–24, 1968, was imbedded.

II. Theoretical Background

To determine the factors contributing to kinetic energy changes in a developing cyclone, a kinetic energy budget equation is derived in the following manner:

The rate of specific kinetic energy change can be found by forming the scalar product of the horizontal wind vector and the equations of motion. Thus,

$$\frac{dk}{dt} = -\mathbf{V} \cdot \nabla_p \Phi + \mathbf{V} \cdot \mathbb{F} \tag{1}$$

where k is the specific kinetic energy, $\mathbf{V}$ is the horizontal wind vector, ∇_p is the gradient measured on a pressure surface, $\Phi = gz$ is the geopotential and $\mathbb{F}$ represents the friction force. By expanding the total derivative in equation (1) and multiplying through by ρ, one obtains

$$\rho\frac{\partial k}{\partial t} + \rho[\nabla_p \cdot k\mathbf{V} - k\nabla_p \cdot \mathbf{V} + \omega\frac{\partial k}{\partial p}] = -\rho\mathbf{V} \cdot \nabla_p \Phi + \rho\mathbf{V} \cdot \mathbb{F} \tag{2}$$

by use of the identity

$$\nabla_p \cdot k\mathbf{V} = k\nabla_p \cdot \mathbf{V} + \mathbf{V} \cdot \nabla_p k. \tag{3}$$

Introducing the continuity equation in pressure coordinates, equation (2) can be written as

$$\rho\frac{\partial k}{\partial t} + \rho\nabla_p \cdot k\mathbf{V} + \rho\frac{\partial}{\partial p}(k\omega) = -\rho\mathbf{V} \cdot \nabla_p \Phi + \rho\mathbf{V} \cdot \mathbb{F}\,. \tag{4}$$

It is noted here that the term involving the vertical derivative will, as usual, be neglected because it is often at least two orders of magnitude smaller than the divergence term in equation (4).

With the above assumption, integration of equation (4) in Cartesian coordinates yields

$$\iiint_V \rho\frac{\partial k}{\partial t}\,dV = -\iiint_V (\rho\nabla_p \cdot k\mathbf{V})dV - \iiint_V (\rho\mathbf{V} \cdot \nabla_p \Phi)dV + \iiint_V (\rho\mathbf{V} \cdot \mathbb{F})dV \tag{5}$$

where $dV = dxdydz$.

In pressure coordinates, equation (5) becomes

$$\frac{\partial K}{\partial t} = \frac{1}{g}\iiint_{V_p}(\nabla_p \cdot k\mathbf{V})dV_p + \frac{1}{g}\iiint_{V_p}(\mathbf{V}\cdot\nabla_p\Phi)dV_p - \frac{1}{g}\iiint_{V_p}(\mathbf{V}\cdot\mathbf{F})dV_p \tag{6}$$

where $dV_p = dxdydp$ and $K = -\frac{1}{g}\iiint_{V_p} kdV_p = \iiint_V \rho k dV$.

The first integral on the right side of equation (6) may be transformed by means of Gauss' divergence theorem such that

$$\frac{1}{g}\iiint_{V_p}(\nabla_p \cdot k\mathbf{V})dV_p = \frac{1}{g}\iint_\sigma kV_r d\sigma \tag{7}$$

where V_n is the outward directed component of the velocity vector perpendicular to any element, $d\sigma$, of the surface bounding the volume over which the integration is performed. Thus $d\sigma = dxdp$ or $dydp$. Equation (6) finally becomes

$$\frac{\partial K}{\partial t} = \frac{1}{g}\iint_\sigma kV_n d\sigma + \frac{1}{g}\iiint_{V_p}(\mathbf{V}\cdot\nabla_p\Phi)dV_p - \frac{1}{g}\iiint_{V_p}(\mathbf{V}\cdot\mathbf{F})dV_p \ . \tag{8}$$

It is seen from equation (8) that the total horizontal kinetic energy (K) in a fixed volume may change as a result of: (a) the advection of kinetic energy through the boundaries of the volume; (b) production of kinetic energy in the volume by means of the conversion of available potential energy to kinetic energy as described by Dutton and Johnson (1967); or (c) a loss of energy through frictional dissipation.

In the present study both the kinetic energy change term and the advection term will be evaluated for a region over the United States in which an extratropical cyclone develops rapidly. The conversion (C) and dissipation (D) terms are difficult to evaluate and no attempt will be made to do so in this study. However, the relative importance of each of these processes can be determined by differencing the kinetic energy change (ΔK) term and the advection or boundary (B) term. Expressed simply, equation (8) becomes

$$\Delta K - B = C - D \ . \tag{9}$$

Thus the predominance of either conversion or dissipation for various layers

of the storm may be determined at various times simply by the sign of the left side of equation (9). If $\Delta K - B$ yields a positive result, net conversion resulted; if $\Delta K - B$ gives a negative result, net dissipation occurred.

III. Significance of the Case Under Study

As stated earlier, the purpose of this study is to determine the extent to which kinetic energy is supplied to a developing storm from external sources. In addition, it was shown that it is possible, in principle, to estimate the relative importance of the conversion of available potential energy to kinetic energy as compared with the frictional dissipation of kinetic energy. In this way, significant insight can be obtained into the mechanisms responsible for the production of kinetic energy in a developing cyclone. If the kinetic energy is initially produced entirely within a developing storm through a conversion process, it follows that the mechanisms implicit in the theory of baroclinic instability are responsible for the original cyclogenesis. On the other hand, if the initial supply of energy is advected into the storm, the theory of barotropic instability takes on renewed importance.

The surface maps in Figures 1 and 2 show the storm at the first and last of the four periods examined. The storm underwent continued development during this period but reached maturity during the following day. An Applications Technology Satellite (ATS-III) photograph of the storm is shown in Figure 3.

There are evident in the picture three features of the storm that are particularly significant. First, the clear area behind the cold front denotes an intense frontal zone from Ohio southwestward into Texas. Isotherm packing at 500 mb, shown in Figures 4 and 5, attests to the presence of a subsiding upper front in that region. The 500 mb isotachs presented in Figures 6 through 9 show the evolution of the main concentrations of kinetic energy at this level. Second, the isotach maximum over Texas in Figure 7 actually represents the merger of a jet maximum previously over Nevada and a subtropical jet streaming northeastward over Mexico and Texas. Additional evidence for the subtropical jet is provided by the cirrus clouds observed in the photograph (Figure 3) over central Mexico. At Del Rio, Texas, winds at 250 mb were observed to reach speeds in excess of 140 knots at 1200Z on April 23 (Figure 10). Third, a sequence of photographs indicates that the cloud pattern over Missouri undergoes continual erosion as a third northerly jet (Figure 11) develops at lower levels during the day and subsides just south of the storm center.

All of the above features strongly suggest that considerable amounts of kinetic energy are being advected into the storm from great distances.

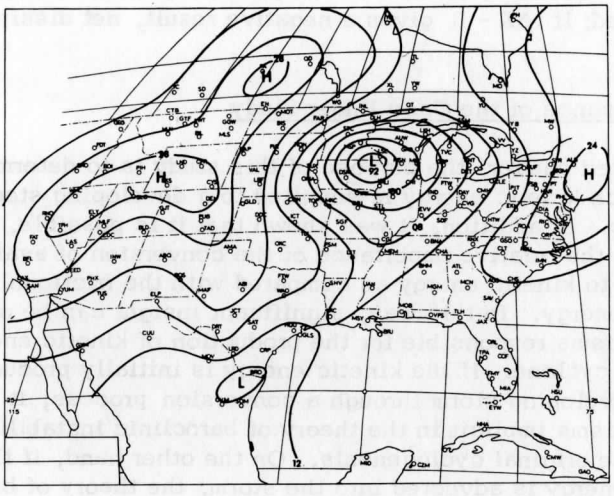

Fig. 1: 12Z Surface Isobars for April 23, 1968

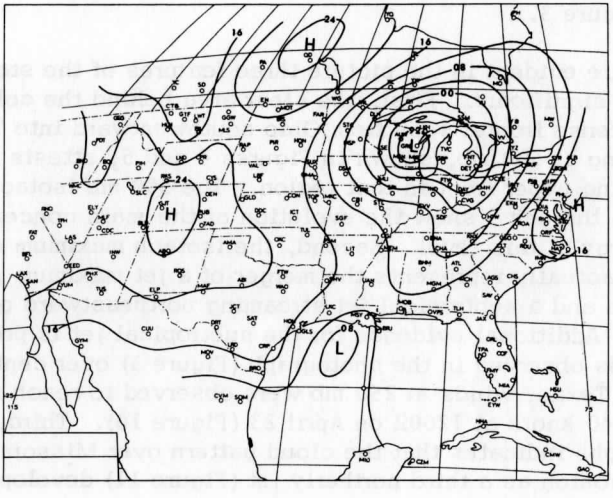

Fig. 2: 00Z Surface Isobars for April 24, 1968

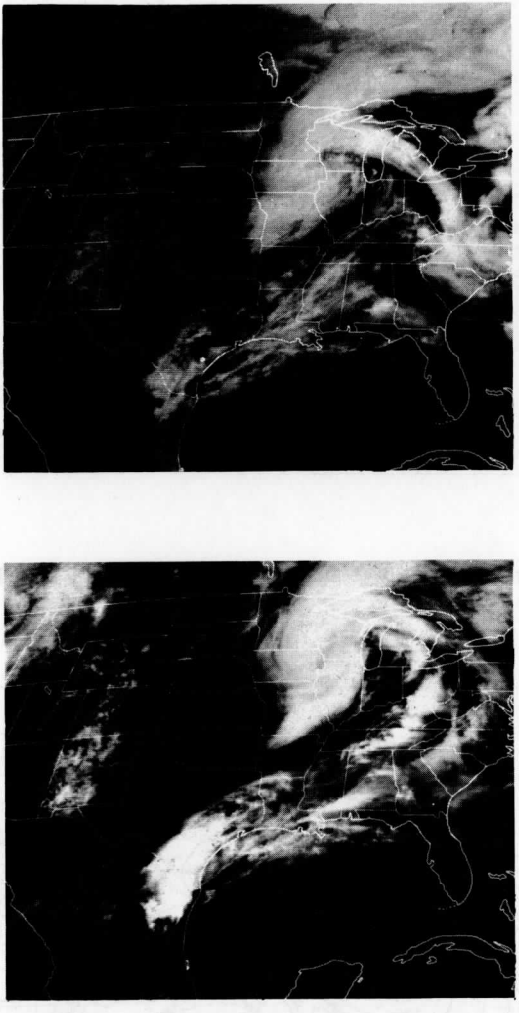

Fig. 3: 20Z Satellite Photograph of April 23, 1968

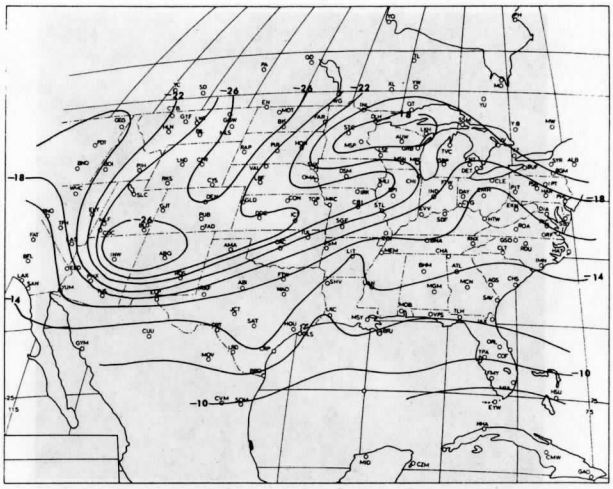

Fig. 4: 12Z 500 mb isotherms for April 23, 1968

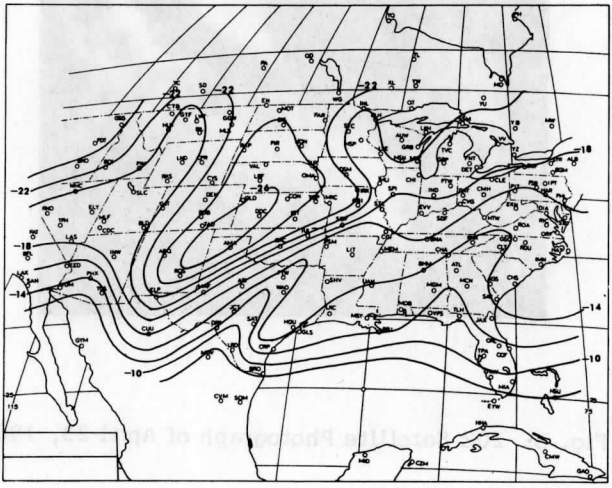

Fig. 5: 00Z 500 mb isotherms for April 24, 1968

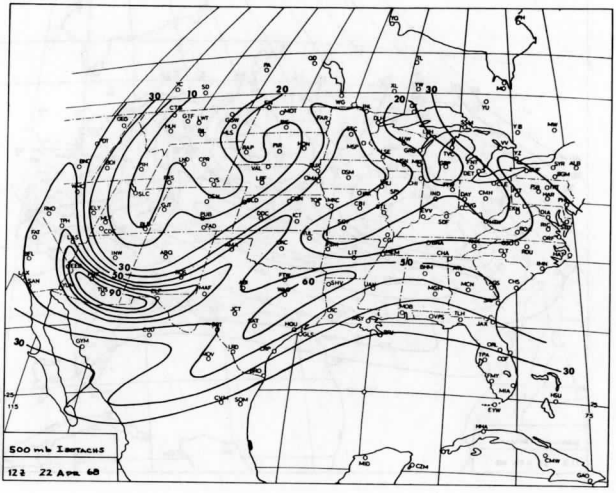

Fig. 6: 12Z 500 mb isotachs for April 22, 1968

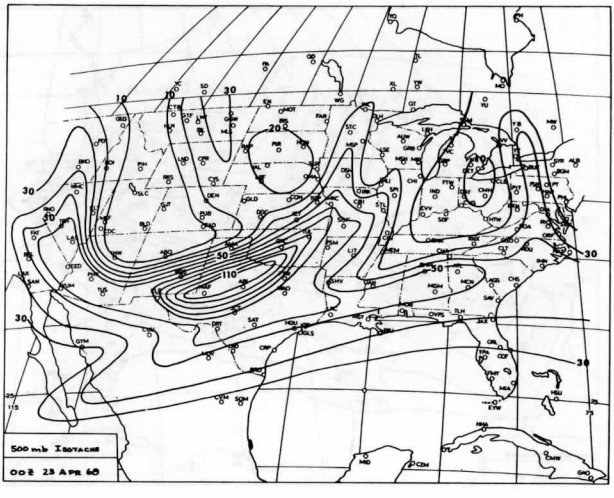

Fig. 7: 00Z 500 mb isotachs for April 23, 1968

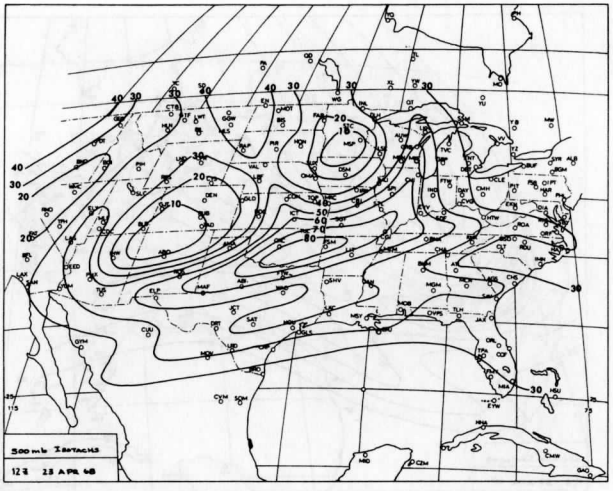

Fig. 8: 12Z 500 mb isotachs for April 23, 1968

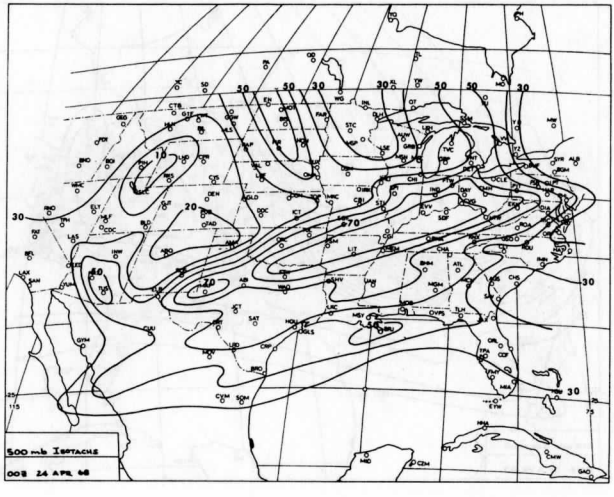

Fig. 9: 00Z 500 mb isotachs for April 24, 1968

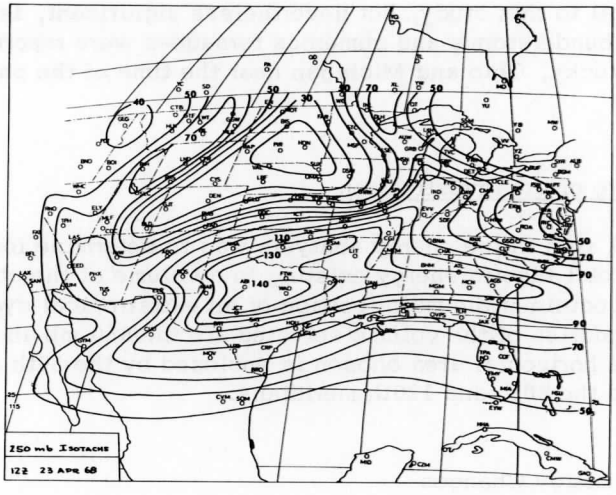

Fig. 10: 12Z 250 mb isotachs for April 23, 1968

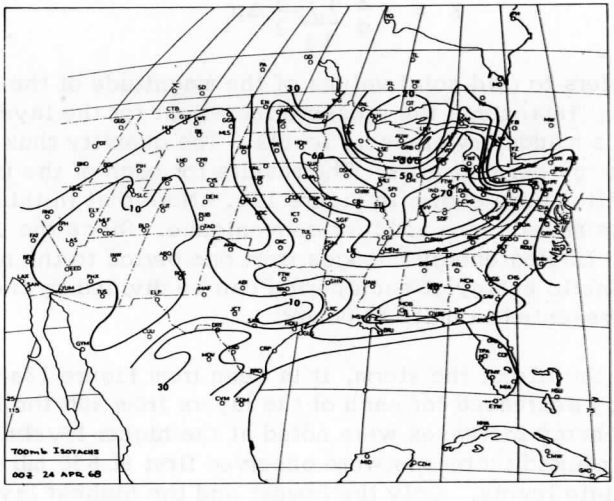

Fig. 11: 00Z 700 mb isotachs for April 24, 1968

Obviously, it is imperative that the role of these various jet streams in the storm's growth be better understood.

Incidental to this study, but nevertheless significant, is the fact that severe thunderstorms and numerous tornadoes were reported in Tennessee, Kentucky, Ohio and Michigan near the time of the photograph in Figure 3.

IV. Procedure of the Investigation

The first step in the energy analysis was to determine for various periods the total kinetic energy existing in a volume of the atmosphere in which is contained the major portion of an extratropical cyclone. The vertical boundaries of the volume selected are the 850 mb and 200 mb surfaces; the horizontal area chosen is enclosed by the 30th and 50th parallels and the 80th and 120th meridians.

A. Kinetic Energy Changes

Isotach analyses were performed for each of the seven mandatory pressure levels from 850 mb to 200 mb for four time periods. The total kinetic energy in the volume was calculated by integrating grid point values according to the equation

$$K = -\frac{1}{g} \sum_i \sum_j \frac{V_j^2}{2} \Delta p_i \qquad (10)$$

where V_j refers to grid point values of the magnitude of the horizontal wind and Δp_i represents the pressure increment for the layer centered on the various mandatory pressure levels. The quantity thus calculated is kinetic energy per unit area. The results for each of the individual layer calculations are shown in Figure 12a. Note that in this figure the units of watts meter^{-2} are used for convenience. Since the ultimate interest is in finding energy changes from one period to the next, the integrated kinetic energy at each period can be divided by the time increment and represented in units of power.

Early in the life of the storm, it is seen from Figure 12a that the kinetic energy decreased for each of the layers from 400 through 850 mb. Only slight energy increases were noted at the higher levels. As time progressed, marked increases were observed first at 850 mb and then at the intermediate levels. Only the lowest and the highest layers showed decreases between the last two periods examined.

The most spectacular energy increases were observed to occur between April 23/00Z and 23/12Z at 850 mb and during the last period at 500 and 300 mb. For these three cases, separate analyses of velocity changes were prepared in order to observe the area in which significant speed changes occurred. Figures 15 through 17 show that the areas of largest energy increase for each of the three layers occurred in the vicinity of the severe weather as observed along the cold front seen on the photograph in Figure 3. This is in good agreement with work of Darkow (1968) in which large total energy increases were associated with areas of severe weather.

The changes of total kinetic energy for the entire volume are shown in Figure 13b, which shows a slight decrease of kinetic energy between the first two periods and rapid increases during the remaining times.

B. Advective Changes

In Chapter II, it was shown that the difference between the total kinetic energy change and the net advection into a volume would be a measure of the relative importance of the conversion and dissipation processes in the storm. In the last section calculation of the kinetic energy changes were described. The problem remaining is to determine the advection or flux term.

From equation (8) the working equation for calculating the advection is seen to take the form

$$B_x = \frac{-\frac{1}{g}\sum_i\sum_j (KV_n)_j \Delta y \Delta p_i}{N_x \Delta x N_y \Delta y} \qquad (11)$$

for the east and west sides of the volume and

$$B_y = \frac{-\frac{1}{g}\sum_i\sum_j (K V_n)_j \Delta x \Delta p_i}{N_x \Delta x N_y \Delta y} \qquad (12)$$

for the north and south sides. In equations (11) and (12), the divisor insures that the advective term is measured per unit horizontal area so that it can be compared with the kinetic change term. In the above equations N_x and N_y are the number of grid points, with Δx and Δy representing increments of length corresponding to the horizontal dimensions of the volume. V_n is the horizontal component of the wind speed perpendicular to the side of the volume being examined. The i and j subscripts denote that the integration is over all pressure layers and

grid points, respectively. In practice, the flux, or advective term, is calculated for each of two times and then averaged.

The results of the flux calculations are summarized in Figure 12b. Large amounts of kinetic energy were obviously being advected into the volume containing the storm during the initial stages. In general, this advection decreased with time until, in the later stages, there occurred a net advection of kinetic energy out of the storm. The advection for the entire volume is shown for the various times in Figure 13a.

Table I (Parts 1 and 2) depicts the flux contributions from each of the four sides of the volume under study. The most dominant feature is the magnitude of the kinetic energy transport into the volume through the south side at each time. Obviously, the subtropical jet in the vicinity of 300 mb supplied considerable amounts of kinetic energy to the developing storm.

C. Conversion Versus Dissipation

In the previous sections the procedure for evaluating both the kinetic energy change term and the advection term was described. From Chapter II it is seen that by differencing these two values layer by layer for the various time periods, an estimate can be made of the relative importance of conversion or dissipation processes. The results of this differencing are presented in Figure 14. It is clear from this figure that the conversion process could not have been important in the initial development of the storm. Regardless of the fact that there may have been considerable conversion of available potential energy to kinetic energy in the early stages, Figure 14 shows that there was net dissipation occurring at all levels of the storm except the topmost one. Later in the development, conversion overcame dissipation by increasingly large amounts starting at the lower levels before appearing later at successively higher levels. For the final period examined the most effective conversion took place at 500 mb while at 850 mb dissipation again became the dominant process. The integrated conversion versus dissipation process for the entire volume is summarized in Figure 13c.

TABLE I—PART 1

Energy Fluxes in (watts meter^{-2}), April, 1968

22/12Z	850	700	500	400	300	250	200	Row Totals
North	.21	.02	.35	.07	-.98	-.35	-.08	-.76
East	-.03	-.21	-.86	-.67	-1.53	-1.99	-2.41	-7.70
South	.18	-.35	.88	1.08	2.95	2.75	3.00	10.50
West	.03	.16	.82	.99	1.02	1.37	1.36	5.76
Column totals	.39	-.38	1.19	1.33	1.46	1.78	1.87	Overall Total 7.7

23/00Z	850	700	500	400	300	250	200	Row Totals
North	.13	.01	.13	.77	.93	.27	-.01	2.23
East	-.02	-.16	-.73	-.96	-2.14	-2.66	-2.60	-9.29
South	-.05	.00	.34	.55	1.63	1.40	1.15	5.03
West	.00	.03	.51	.29	.69	1.48	1.36	4.36
Column totals	.06	-.12	.25	.65	1.11	.49	-.08	Overall Total 2.3

TABLE I—PART 2

23/12Z	850	700	500	400	300	250	200	Row Totals
North	-.15	.45	-.52	-.62	-.17	-.64	-.28	-1.86
East	-.04	-.10	-.44	-.71	-3.29	-1.79	-2.53	-8.90
South	-.14	-.11	.24	.81	2.77	1.94	2.15	7.66
West	.05	.19	.65	.70	.82	.79	.44	3.62
Column totals	-.27	.43	-.06	.18	.13	.29	-.22	Overall Total .5

24/00Z	850	700	500	400	300	250	200	Row Totals
North	.12	.27	-.45	-.46	-.77	-.33	-.17	-1.78
East	-.26	-.74	-1.19	-1.09	-2.21	-3.64	-2.58	-11.71
South	-.02	.05	.22	.08	2.42	1.64	.61	5.02
West	.03	.19	.96	.70	1.10	.81	.82	4.50
Column Totals	-.13	-.23	-.46	-.77	.54	-1.52	-1.32	Overall Total -3.9

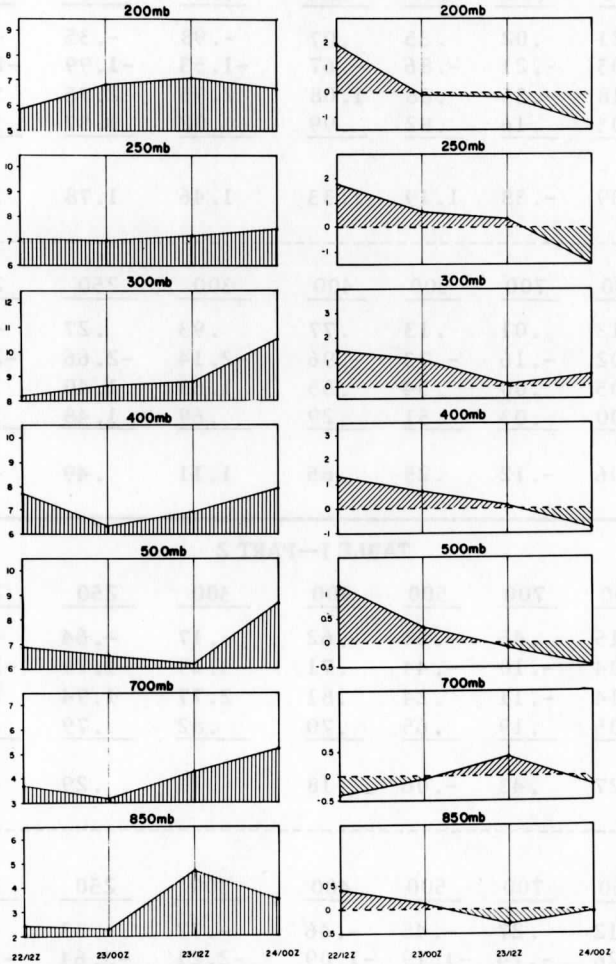

FIG. 12a TOTAL ENERGY CHANGES (WATTS-METER^{-2})

FIG. 12b ENERGY FLUX CHANGES (WATTS-METER^{-2})

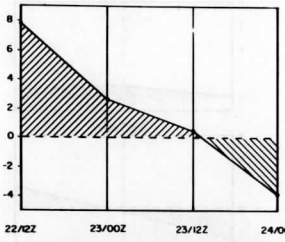

FIG. 13a COMPOSITE KINETIC ENERGY FLUX CHANGES (WATTS-METER^{-2})

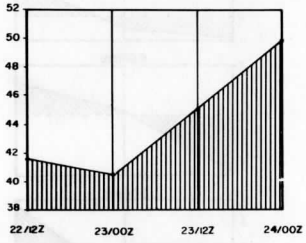

FIG. 13b COMPOSITE TOTAL KINETIC ENERGY CHANGES (WATTS-METER^{-2})

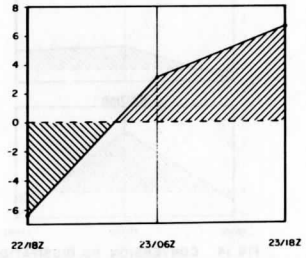

FIG. 13c COMPOSITE CONVERSION VS DISSIPATION (WATTS-METER^{-2})

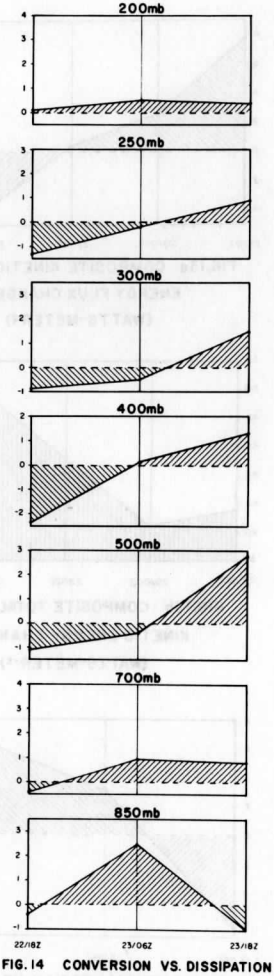

FIG. 14 CONVERSION VS. DISSIPATION (WATTS-METER^{-2})

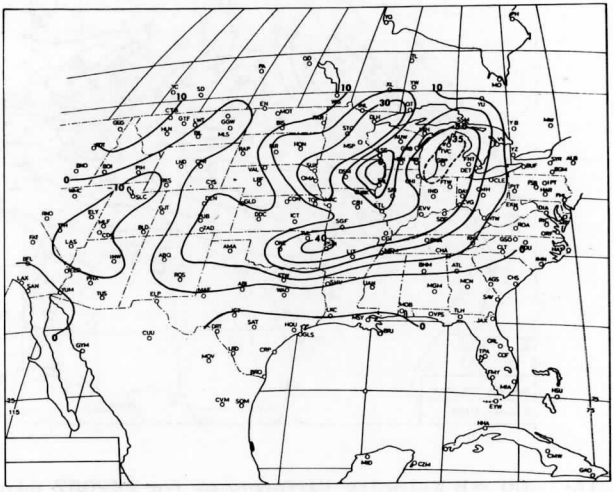

Fig. 15: 850 mb Velocity Differences for 23/12Z minus 23/00Z, April, 1968

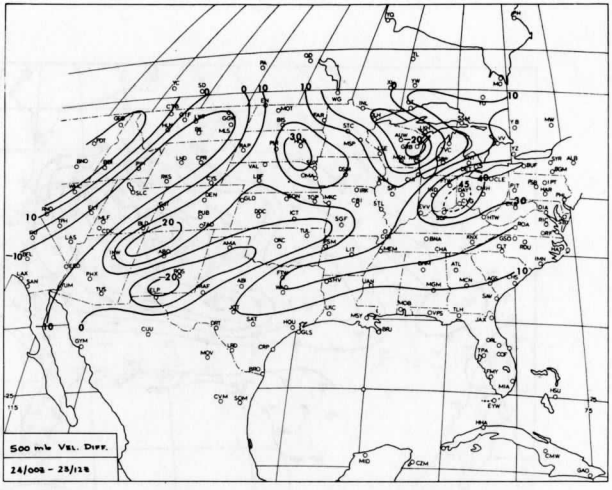

Fig. 16: 500 mb Velocity Differences for 24/00Z minus 23/12Z, April, 1968

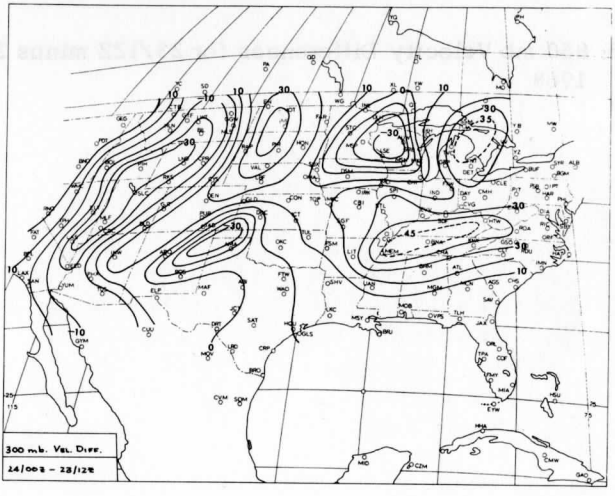

Fig. 17: 300 mb Velocity Differences for 24/00Z minus 23/12Z, April, 1968

V. Summary and Suggestions for Future Research

In reviewing the results of this study of kinetic energy changes in the developing cyclone of April 22–24, 1968, the following salient features emerge:

First, the kinetic energy of the volume in which this storm developed remained nearly constant or decreased slightly during the earliest period of growth. For this same period, the results indicate that dissipation processes were dominant in the storm area. Therefore, it can be concluded that the conversion of available potential energy to kinetic energy, however great, could not have alone contributed to the growth or even the maintenance of the storm during the original cyclogenesis. On the other hand, the large amount of kinetic energy advected into the volume of the storm must have contributed significantly to maintaining its level of kinetic energy. Without this influx of energy from outside the volume the dissipation process would have significantly reduced the relatively high level of kinetic energy characteristic of the storm. Instead, the energy level was maintained; during subsequent periods the conversion process evidently became the dominant energy source for the cyclone.

Second, there is evidence that the conversion process, after becoming effective in contributing kinetic energy to the storm, begun first at low levels before occurring later at successively higher levels.

Third, the subtropical jet was evidently a prime contibutor of kinetic energy to the developing cyclone. This fact stimulates considerable interest in the origin of this jet and its further implications regarding its role in the cyclogenetic process.

Fourth, although the net flux into the volume decreased and changed sign as the storm progressed, it must not be concluded that the conversion process was the only mechanism that contributed to development in the later periods of the storm's life. In smaller volumes in the immediate vicinity of the cyclone it was found, even at later times, that kinetic energy advection accounted for most of the kinetic energy increases at higher levels. Although there was a net kinetic energy transport out of the larger volume during these times, locally there was appreciable advection into the core of the storm.

The results of this study indicate that the advection of kinetic energy from sources far removed from the storm center is important in the maintenance of the cyclone during its early stage of development. This observation reaffirms the importance of barotropic instability theory in cyclogenesis. Moreover, it is clear that additional research should be carried out to ascertain the locale and precise mechanisms which are responsible

for generating both the subtropical jet and the main mid-latitude jet which seems to form near the ridge upstream from the developing storm.

Also, it is imperative that additional studies of the conversion process be made to understand why the effective conversion originates at low levels of the storm and moves progressively upward.

Finally, it would be useful to reexamine the contribution of the vertical advection of kinetic energy. Of course, this must await more satisfactory calculation of the vertical motion fields for a cyclone. It appears that with greater accuracy and more resolution in the vertical motion field instances of significant vertical advection may be found.

BIBLIOGRAPHY

Charney, J. G., 1947: The dynamics of long waves in a baroclinic westerly current. J. Meteor., 4, p. 135.

Darkow, G. L., 1968: The total energy environment of severe storms. J. Appl. Meteor., 7, 199-205.

Danielsen, E. F., 1964: Project Springfield Report. Defense Atomic Support Agency. DASA 1517, Washington, D.C., 97 pp.

Dutton, J. A., and Johnson, D. R., 1967: The theory of available potential energy and a variational approach to atmospheric energetics. Advances in Geophysics, 12, 333-436, Academic Press, New York.

Eady, E. T., 1949: Long waves and cyclone waves. Tellus, 1, 33-52.

Eliasen, E., 1960: On the initial development of frontal waves. Publ. Danske Meteor. Inst., Meddelser No. 13.

Fjortoft, R., 1950: Application of integral theorems in deriving criteria of stability for laminar flows and for the baroclinic circular vortex, Geofys. Publikasjoner, Norske Vedenskaps-Akad., Oslo, 17(6).

Kuo, H. L., 1949: Dynamic instability of two-dimensional flow in a barotropic atmosphere. J. Meteor., 6, p. 105.

Kuo, H. H., 1952: Three-dimensional disturbances in a baroclinic zonal current. J. Meteor., 9, 260-278.

Petterssen, S., 1956: Instability theories of cyclone formation. Weather Analysis and Forecasting, 1, 305-318.

Reed, R. J., 1955: A study of a characteristic type of upper-level frontogenesis. J. Meteor., 12, 226-237.